CHARACTERIZING G-LOADING, SWIRL DIRECTION, AND RAYLEIGH LOSSES IN AN ULTRA COMPACT COMBUSTOR

THESIS

Jacob D. Wilson

AFIT-ENY-13-S-02

DEPARTMENT OF THE AIR FORCE

AIR UNIVERSITY

AIR FORCE INSTITUTE OF TECHNOLOGY

Wright-Patterson Air Force Base, Ohio

DISTRIBUTION STATEMENT A. APPROVED FOR PUBLIC RELEASE;

DISTRIBUTION UNLIMITED

AFIT-ENY-13-S-02

CHARACTERIZING G-LOADING, SWIRL DIRECTION, AND RAYLEIGH LOSSES IN AN

ULTRA COMPACT COMBUSTOR

THESIS

Presented to the Faculty

Department of Aeronautics and Astronautics

Graduate School of Engineering and Management

Air Force Institute of Technology

Air University

Air Education and Training Command

In Partial Fulfillment of the Requirements for the

Degree of Master of Science in Aeronautical Engineering

Jacob D. Wilson, BS

U.S. Civilian

July 2013

AFIT-ENY-13-S-02

CHARACTERIZING G-LOADING, SWIRL DIRECTION, AND RAYLEIGH LOSSES IN AN

ULTRA COMPACT COMBUSTOR

Jacob D. Wilson

Approved:

_____   _____

 Marc D. Polanka, PhD (Chairman)   Date

_____   _____

Mark F. Reeder, PhD (Member)   Date

_____   _____

Maj James L. Rutledge, PhD (Member)   Date

AFIT-ENY-13-S-02

Abstract

Previous research has been conducted showing significant benefits on combustion

efficiency and stability by creating high centripetally accelerated, also known as g-loaded,

combustion environments. Ultra Compact Combustor systems decrease size and weight of the

overall engine by burning in a circumferential direction around a hybrid vane row where the high

equivalence ratio cavity flow is quick quenched to lean by the core flow. The hybrid vane row

integrates the compressor, combustor, and turbine for further length reduction and weight

savings. Fuel and air are brought into the cavity and combusted in a high g-loaded environment

driven by air injection at an angle tangent to the cavity outer diameter. The Air Force Research

Lab and Air Force Institute of Technology have worked previously on compact combustor

designs, and a new, high g-loaded, Ultra Compact Combustor has been designed to study flow

characteristics in the cavity and core to help understand integration issues with engine systems.

The Combustion Optimization and Analysis Laser Lab was also heavily modified and upgraded

in order to support the new test rig. Swirl direction was varied in order to determine the proper

cavity flow direction with respect to the hybrid vane, and showed a suction-side vane impact to

be the most favorable for less pressure drop and a more uniform cavity flow. Cavity flame

stability and lean blowout tests were completed for a baseline air driver diameter and showed

trends matching previous data. However, high speed video revealed instabilities at higher

equivalence ratios than where lean blowout occurred, establishing stable operating conditions for

the rest of the test cases. Cavity air driver diameter was also varied from 0.35 cm to 0.65 cm to

measure the effects of g-loading. Trends match previous CFD data collected on a large scale

Ultra Compact Combustor model, indicating g-load increased as air driver diameter decreased

for a constant mass flow. Significant velocity gradients were seen over the width of the cavity for the 0.35 cm diameter at the higher flow rates tested. These gradients were not as severe for larger air driver diameters, at the mass flows tested. Rayleigh losses were studied at lower flow rates due to lab capability, but still showed significant Mach number increase and pressure drop due to heat addition. This led to the design of a center body that mitigated these losses using an area increase at the interaction location between the core and cavity, which provided slower burning Mach numbers and some pressure recovery from the baseline case. Finally, internal and external cooling schemes were evaluated for effectiveness in reducing rig material temperatures during testing.

Acknowledgments

First and foremost, I would like to thank Dr. Marc Polanka for giving me the opportunity to earn my master's degree at the Air Force Institute of Technology. He gave me technical insight, life guidance, freedom to explore new ideas, and held high expectations that bettered me as a professional individual. I would not have grown into the engineer I am today without his help.

I would like to thank the lab technicians at AFIT, especially John Hixenbaugh. Mr. Hixenbaugh provided continuous assistance in the lab, purchasing supplies, contacting vendors, and solving problems with equipment. Many students, including myself, would not have a thesis without his help. I would like to thank the AFIT Model Shop. They provided fabrication of countless parts and were extremely reliable, willing to help make a part on a moment's notice. I would also like to thank Jamey Condevaux and Williams International for fabrication of a crucial piece to our test rig that other machine shops were unwilling or unable to build due to its complexity.

I would like to thank my family, as their support, encouragement, and much needed distraction now and again, not only through my graduate education, but in my life in general, has been unwavering and empowered me to achieve things I would otherwise be incapable of doing. Finally, I would especially like to thank my mother. She has endured and persevered through more than anyone I have ever known, and has still been a rock in which our family has been able to thrive. She continues to selflessly give infinite amount of love and support to each one of her children and her husband, and has provided me with every opportunity I could possibly ask for.

Table of Contents

Table of Figures

Nomenclature

A   =   Area

a   =   Local speed of sound

AFRL =   Air Force Research Lab

AFIT =   Air Force Institute of Technology

CCW =   Counter-clockwise cavity direction, corresponding to a pressure-side vane impact

CFD   =   Computational Fluid Dynamics

COAL =   Combustion Optimization and Analysis Laser

C_p =   Specific heat capacity at constant pressure

CW   =   Clockwise cavity direction, corresponding to a suction-side impact on vane

DAQ   =   Data Acquisition Unit

DPIV   =   Digital particle image velocimetry

EGV   =   Exit guide vanes (compressor)

FS   =   Full scale value

FT   =   Fischer-Tropsch (fuel)

G   =   g-load

g   =   Gravitational constant for earth

GCF   =   Gas correction factor

HPT   =   Higher pressure turbine

HSV   =   High speed video

IB   =   Instrumentation block

ID   =   Inner diameter

IGV   =   Inlet guide vanes (turbine)

IR   =   Inner radius

IR   =   Infrared

ISSI   =   Innovative Scientific Solutions, Inc.

ITB   =   Inter-turbine burner

LBO   =   Lean Blow Out

LE   =   Leading edge

LLCB	=	Low Loss center body
LPT	=	Low pressure turbine
M	=	Mach number
$\dot{m}$	=	Mass flow rate
MFC	=	Mass flow controller
MFR	=	Mass flow ratio (between the cavity and core)
N	=	Step number
NI	=	National Instruments
Nu	=	Nusselt Number
OAP	=	Optical access port
OD	=	Outer diameter
OFAR	=	Overall fuel to air ratio
P	=	Pressure
PDPA	=	Phase Doppler Particle Analyzer
PSI	=	Pounds per square inch
r	=	Radius
Re	=	Reynolds Number
R	=	Gas constant
RNG	=	Renormalization Group method
RVC	=	Radial vane cavity
SFC	=	Specific fuel consumption
T	=	Temperature
TCB	=	Tapered center body
TE	=	Trailing edge
TVC	=	Trapped Vortex Combustor
UCC	=	Ultra Compact Combustor
q"	=	Heat rate
V	=	Velocity
Φ	=	Equivalence ratio
γ	=	Ratio of specific heats

ρ = Density (kg/m^3)

Subscripts

c = Referring to gravitational constant of Earth

cav = Referring to cavity

COLD = Non-reacting conditions

f = Final condition

HOT = Reacting conditions

i = Initial condition

S = Stoichiometric

t = Total (stagnation) condition

tan = Tangential direction

3 = At the inlet of the combustor

4 = At the exit of the combustor

I.   Introduction

Since the introduction of the jet engine in 1929, the overall system layout has remained unchanged in the core section. The core section is made up of three main, interdependent systems: the compressor, combustor, and the turbine, all which must be designed dependent on the needs of the others for an engine to function correctly. Air enters the compressor and is pressurized before entering the combustor, where the air is slowed to a low Mach number and fuel is added and burned at fuel lean conditions [1] in the axial direction, dramatically increasing temperature of the gas at relatively constant pressure. The hot gas exits through the turbine, which expands the flow to create kinetic energy and power the compressor and other auxiliary systems such as electronics or pumps. The flow is then accelerated out of the engine via the nozzle. The majority of the thrust provided by the engine is dependent on this exit velocity multiplied by the amount of mass flow exiting the nozzle.

Manufacturing, material, and technological advances have taken simple jet engines from their birth pre-World War II to extremely sophisticated systems of highly advanced components, which is especially true for the turbine section. The extremely high temperatures leaving the combustor ($T_{t,4}$) make turbine design especially challenging, as each blade must be able to perform and survive in this harsh environment. High $T_{t,4}$ is required for both higher engine efficiency and greater propulsion, necessitating the use of exotic, nickel-based alloys that withstand hotter temperatures with less thermal growth and film cooling techniques that allow for bleed air to form a protective "barrier" around hot spots of the vane. These techniques increase the life of turbine, but drive up blade cost. These hot spots can be caused by burning that

1

is still happening on the way out of the combustor and into the turbine inlet guide vane (IGV) or non-uniformity in the hot gas flow.

For this reason, most engines burn lean in the combustor, however, typical jet engine combustor configurations still require formidable axial length to achieve complete combustion before entering the turbine section, seen in Figure 1. This axial length adds weight to the engine, which hinders improving thrust-to-weight ratio, one of the main goals of engine design. For the last few decades, improving thrust-to-weight of the engine has been accomplished by implementing new ways to increase thrust. This can also be done by reducing the weight of the engine, specifically in the combustor section. A more novel approach to the combustor design could allow for decreased length and weight, increasing thrust-to-weight of the engine, while maintaining combustion efficiency and increasing turbine blade life.
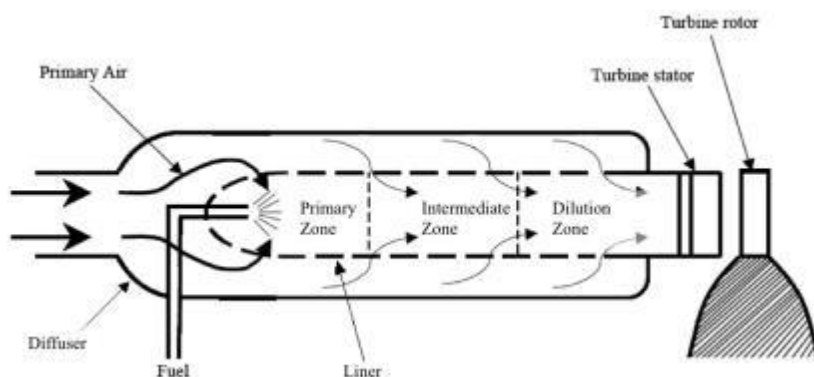
Figure 1. Typical combustor system [2]

1.1. Ultra Compact Combustor

The Ultra Compact Combustor (UCC) is one solution that could potentially meet or exceed the required temperatures and efficiencies while increasing the thrust-to-weight ratio of

the engine. The Air Force Research Lab (AFRL) and the Air Force Institute of Technology

(AFIT) have been working on a joint project to study trapped vortex combustor (TVC) designs

with and without centrifugal force effects, known as gravitational loading (g-loading). While the

traditional combustion process occurs through the engine axially, the high g-loaded configuration

of the UCC achieves the necessary residence time by forcing combustion to occur in a

circumferential cavity around the outer diameter (OD) of the engine, reducing the overall axial

length, shown in Figure 2. The compressor exit guide vane (EGV) and the turbine IGV are

removed and replaced by a single, hybrid vane that takes flow from the last compressor rotor into

the first turbine rotor. Ahead of the hybrid vane, flow from the compressor rotor is split into the

circumferential cavity and core section. Replacing the two stages with the single hybrid vane

coupled with the reduction in combustor length is estimated to reduce the system length up to

66% [3, 4].
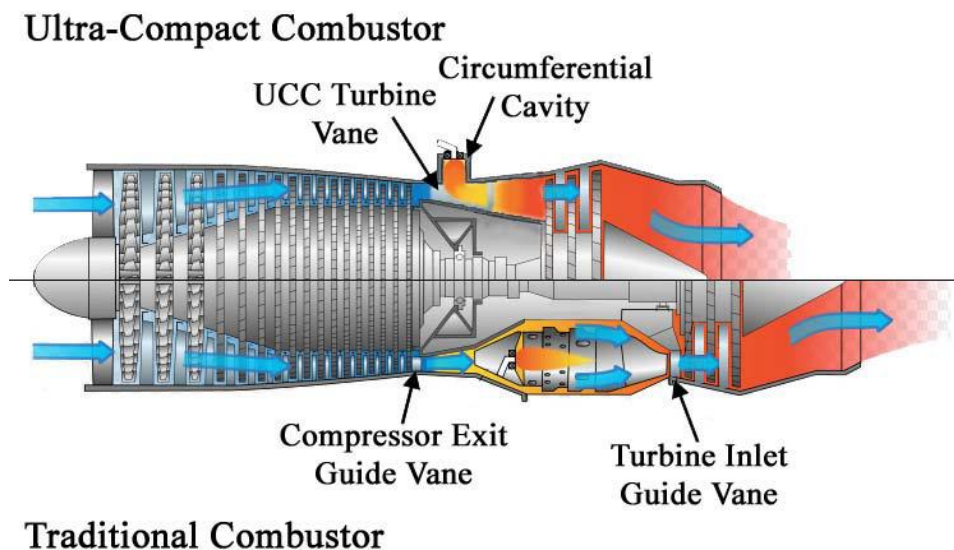
Figure 2. Reduced axial length from a modern turbine engine [4]

The cavity flow breaks off and is injected into an outer circumferential cavity through a series of driver jets that force the flow to rapidly move in the circumferential direction, which generates a swirl/g-loaded effect in the cavity, shown in Figure 3. Fuel is injected into this flow and is burned at higher than stoichiometric equivalence ratios, otherwise known as a fuel-rich condition [5]. Lewis [6] studied swirl effects on combustion and found that g-loading above a minimum threshold increases flame speed. Higher flame speed is indicative of increased reaction rates [5], and when coupled with the high turbulence intensity in the cavity that increases mixing, a decreased combustor volume can be utilized with equal or added efficiency. Additionally, swirl also causes a buoyancy phenomenon in the cavity. In theory, heavier particles (unburned fuel and cold air) are pulled to the OD by the g-loading allowing for reactants to remain in the circumferential cavity until they are combusted. Meanwhile, lighter, combustion products are pushed to the ID of the cavity, causing a density gradient from the OD to the ID. This creates an extremely efficient burning environment where unburned fuel is unlikely to leave the combustor section, even one with a short axial length, for fuel-to-air mixtures less than or equal to stoichiometric conditions. For fuel rich conditions, fuel products not burned in the cavity mix with the core air in the hybrid vane section and finish combustion. This allows for higher temperature gain in the combustor as a whole, with the same or greater efficiency as conventional main burners.
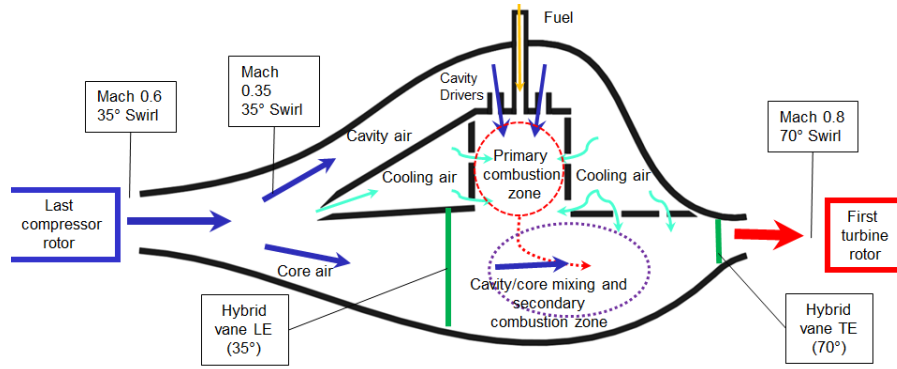
Figure 3. Cavity-core flow split and flow direction

Because of its shorter length, the UCC has shown potential for use as a second stage combustor system called an Inter-Turbine Burner (ITB). An ITB allows for high levels of low-pressure energy to be extracted by the low-pressure turbine, with only a modest rise in temperature [7]. Additional energy could be used to operate a large bypass fan or supply additional electrical power to aircraft systems.

Designing the UCC, whether as a main combustor or ITB, has many challenges. Diffusing the flow into the core and cavity must be done with minimal losses. In the core, the flow must be slowed so that substantial Rayleigh losses are avoided, and then accelerated to the appropriate Mach number for the turbine. Temperature distribution at the exit of the UCC must also be desensitized to varying operating conditions so that the pattern factor is acceptable for the turbine. As highlighted by Sirignano et al., [7] using the UCC as an ITB presents challenges with mixing at higher flow rates, unsteady flow fields, and increase loads on the low-pressure turbine (LPT). These are examples of obstacles that must be studied and overcome before the UCC can be implemented in an engine.

1.2. Design Methodology

The design of the UCC depends on the engine size, whether its intended use is a primary burner or ITB, and what operating conditions are chosen for a design point. Computational Fluid Dynamic software is a useful tool to study optimization and was done by Bohan [4] for a large diameter (76.2cm) UCC. Findings from this larger-scale study were coupled with previous research to envision a UCC design that was suited for accomplishing various research objectives, while staying within the bounds of the lab setting.

The new UCC design was intended to facilitate the study of main combustor applications, but could be configured as an ITB or afterburner/augmenter as well, and for this reason was extremely modular. The entire rig was therefore designed to have interchangeable pieces to cover the wide range of use, with increased optical access and instrumentation of previous rigs. Once built, the rig was used to study multiple research objectives to forward UCC research toward engine integration. These objectives focused on the rig set up in a main combustor configuration, with simulated compressor air entering the system at swirl and Mach number conditions typical of an engine system, and exit conditions acceptable to enter the turbine rotor.

1.3. Research Objectives

The main focus of this research is to characterize a UCC test rig that accurately replicates the flow that would be seen in a typical combustor environment of a turbine engine. Three main objectives were established to further the future integration effort of the rig with the compressor and turbine sections, with a number of secondary objectives that would further benefit the goal of optimizing the UCC system overall.

The first main objective was to study the loss in the system, particularly those associated with heat addition at high Mach number, known as Rayleigh Loss. The turbine engine system requires pressure and temperature requirements to be met at each stage so that the next part of that system can function properly, and integration of the UCC requires it to satisfy the needs of the surrounding stages. Because the Mach number through the core of the UCC is typically higher than can combustors, significant Rayleigh loss can occur which decrease the efficiency of the system. These losses must be minimized for the UCC to be a viable replacement for typical combustors. To investigate this, two center body sections were designed. The first maintained a nominal through-flow Mach number to serve as the baseline. The second center body was designed to reduce the Mach number locally where the heat addition was expected to attempt to reduce the Rayleigh loss without impacting the aerodynamic losses.

The second primary goal was to determine the proper swirl direction in the circumferential cavity with respect to the hybrid vane/ swirled core flow. Whether the flow interacts with the pressure or suction side of the vane could greatly affect combustion efficiency and could enhance aerodynamic losses. For instance, when impacting the pressure side of the vane, the flow must do significantly more turning in comparison to impacting the suction side, as shown in Figure 4. This could lead to greater pressure losses, but could also increase mixing and result in better efficiency and pattern factor/flow uniformity at the exit. When impacting the suction side, the flow will have to do less turning to migrate into the core, decreasing the pressure loss, but without the mixing effects, this could lead to poor efficiency. Impacting the suction side may also be harder to cool, as shown by Bohan and Polanka [4]. For this purpose, the air injector ring was designed such that it could be flipped to change the swirl direction in the cavity so that each could be studied for the optimal configuration.

7
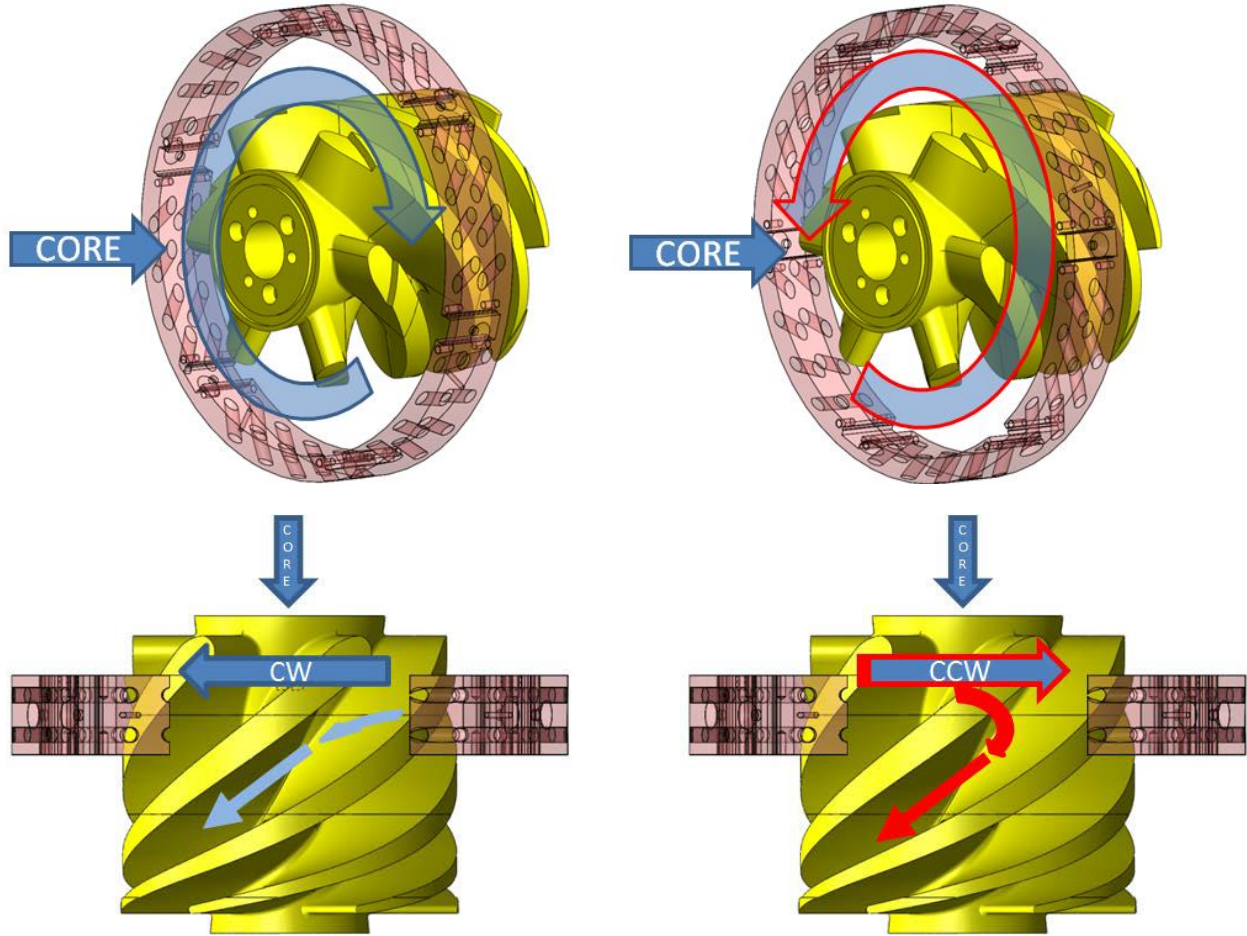
Figure 4. CW (left) and CCW (right) swirl direction variation with respect to the hybrid vane

Lastly, the third main purpose of this research is to study the effects jet diameter sizing

for air driver jets in the circumferential cavity, shown in Figure 3. Bohan and Polanka [4]

showed these holes have significant impact on tangential velocity, and therefore g-loading, for a

given mass flow. However, changing the jet diameters may lead to a change in the mixing within

the cavity and therefore have a significant impact on the efficiency. Three different injector rings

were created with different jet diameters on each ring so that the g-load and efficiency using each

ring could be studied and compared to the others. Proper sizing of the air injection ring is an

important part of the circumferential cavity design and must be properly understood for future UCC systems.

Secondary objectives aimed at characterizing the UCC test rig itself and included generating the overall stable operating range of the rig at different g-loads and equivalence ratios, determining the best flow split between the circumferential cavity and the core flow, and establishing the limiting temperatures of the rig itself.

A combination of experimental and computational/analytical methods were used, including CFD and use of the new UCC test rig, to understand and complete these research objectives. Before this was done, fundamental principles that encompassed the basis of each objective were studied in order to gain an in-depth understanding of each topic. This way, research objectives could be met accurately and precisely under proper testing and data acquisition conditions.

II.   Background

UCC technology has been studied significantly in the past decade by AFRL and AFIT, as well as researchers elsewhere. This interest stemmed from research done on adding swirl and therefore g-loading, on combustion processes. The conclusions of both g-loaded combustion and previous UCC experimentation provide the groundwork for the design/experimentation of the AFIT full annular UCC test rig. To design and characterize a new UCC, a working knowledge of the fundamentals of combustion, previous UCC research, cooling techniques, and data acquisition are required. This chapter focuses on previous research that impacted and led to a better understanding of topics. This establishes the knowledge base for this research to draw on to accomplish the current objectives.

2.1.   G-Loading Effects on Combustion

It has been long recognized that there exists a substantial difference in density between cold reactants and hot products in a combustion environment. In normal earth gravity, a buoyant force is created in a combustion regime as hot combustion products replace colder reactants, given by Equation 1[6]

$$F_B = \rho_a g [1 - {\rho_f}/{\rho_a}]$$

Equation 1

where F_B is the buoyant force per unit volume, g is the acceleration force, ρ_a is the density of the cold reactants, and ρ_f is the density of the hot products. Lewis et al. [6] studied increased g-loading on combustion using a combustion centrifuge, where g-loading was calculated using Equation 2 [3]

$$g - load = \frac{V_{tan}^2}{rg_c}$$

where V_{tan} is the tangential velocity, r is the radius at which the experiment is spinning, and g_c is the acceleration due to gravity. This experiment showed that up to a g-load of 200, combustion is relatively unaffected, but over a g-load of 500, flame speed increases with the square root of g-loading up to about 3500. In this regime, a bubble of combustion gas will travel ahead of the flame front. Above this point, the flame speed is reversed and decreases until a g-load of 7,000 to 8,000 is reached, where combustion will no longer occur.

Lewis et al. [6] then tested applied concepts in a test rig and full-scale turbofan engine augmenter. Research showed that removing typical flame holders from the conventional augmenter and using a swirl-inducing injection pattern to stabilize the flame reduced the pressure loss by approximately half. While, unable to measure directly, it was postulated the swirl augmenter could lead to a 2% improvement in specific fuel consumption (SFC).

Yonezawa et al. [8] developed a computational model of a main engine combustor with swirl and created an experimental prototype based on the results. A conventional combustor was modified with a series of air and fuel injectors that would introduce swirl into the primary combustion zone. Yonezawa et al. were able to increase the loading inside the combustor while still maintaining high levels of combustion efficiencies, showing that fuel could be burned faster, allowing for a reduction in typical combustor lengths up to 33%.

2.2.   Ultra Compact Combustor Research and Design

In 1997, Sirignano et al. [7] proposed that exhaust gas inside the turbine could be reheated via an ITB between the turbine stages. The ITB coupled with a smaller afterburner (smaller than

traditional afterburner) could increase specific thrust and provide lower specific fuel consumption than a traditional afterburner alone. However, typical combustors in turbine engines burned axially and required significant length in order to achieve high combustion efficiency and would increase the length and weight of the engine past the point of this being a viable concept for aircraft applications. The UCC was the proposed solution to the ITB problem and was designed by Anthenien et al. [9]. A circumferential cavity wrapped along the outer radius of the first low pressure stator would split flow from the high pressure rotor and burn at a lean condition, then rejoin the bulk flow to provide a modest temperature rise. Flow would be swirled in the circumferential cavity, creating a centripetal acceleration, known as g-load, implementing buoyancy effects studied by Lewis [6]. Because of the weight difference in particles, the g-load theoretically keeps reactants (heavier) in the cavity, while allowing the products (lighter) to migrate radially inward and exit the burner. The Anthenien et al. rig had a cavity diameter of 11.8 cm, 5 cm wide, and was constructed from 316 stainless steel with the exit tube made from quartz as shown in Figure 5.
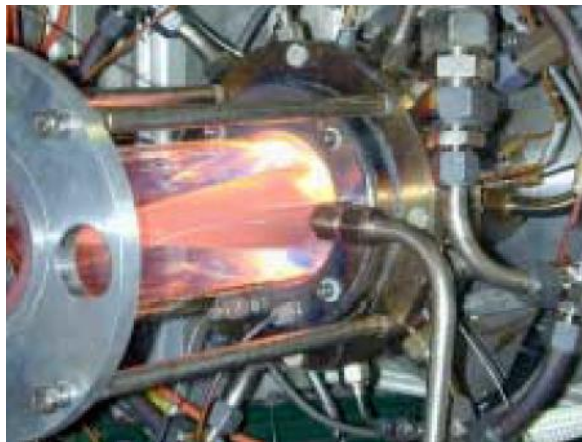
Figure 5. Anthenien et al. UCC rig exit [9]

Figure 6. Fuel and air circumferential injection ring of Anthenien et al. [9]

Fuel was injected into small cavities around the circumferential cavity at six discreet

locations around the cavity ring, and two different designs were made for the air injection. The

first design had twelve air slots that created a curtain of air at each of the injection points. This

design showed very low efficiency and difficult lighting thought to be due to the air collapsing

the fuel spray, reducing the mixing. The second design, shown in Figure 6 had twelve sets of

paired rounded holes which injected air at 45° to the radial direction on either side of the fuel jets

to prevent the fuel spray from being collapsed. The center body was held in place with six, 6 mm

wide support struts that allowed mass transport out of the cavity into the main flow. Anthenien et

al. [9] reported efficiencies for this design of 99+%, achievable for both ethanol and JP-8 fuels

based on emission measurements of CO, CO_2, O_2, NO_X, and unburned hydrocarbons.

Zelina et al. [3, 10] used the test rig from Anthenien et al. [9] study a small-scale, full

annular UCC system at the Air Force Research Lab (AFRL), operating at atmospheric and

increased pressure. They showed combustion efficiencies between 95 and 99%. Axial flame

length was also found to be 50% shorter than in typical combustors, which enables a decrease in

the length, and thus the weight, of these types of combustion systems while also providing a

significant increase of turbine life. Zelina et al. [11] also determined stable lean flame limits

were also determined for various g-load and equivalence ratio combinations shown in Figure 7

for JP-8 fuel, where Configuration 1 has a different radial vane cavity (RVC) than

Configurations 2 and 3. The RVC is primarily designed to assist migration from the

circumferential cavity throughout the entire radial span of the core flow. Configurations 1 and 2

also have 5x more injector air impinging on the fuel atomizers, which was thought to have

increased mixing potential.
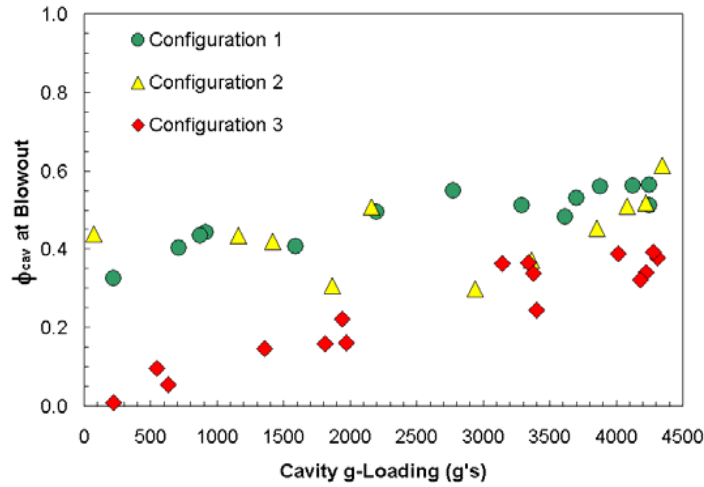
Figure 7. Stability limits of the AFRL UCC test rig [11]

The tangential velocity in the cavity was determined by Equation 3 [10]

$$V_{tan} = \frac{\dot{m}_{cav}}{\rho_{cav} A_{ex}} \frac{1}{\tan \beta}$$

Equation 3

14

where, V_{tan} is the tangential velocity, $\dot{m}_{cav}$ is the mass flow, ρ_{cav} is the cavity density, β is the

cavity air swirl angle with respect to the tangent point of the cavity OD, and A_{ex} is the total exit

area of the injector holes. The density in the cavity was estimated from bulk temperature in the

cavity based on equivalence ratio, while mass flow was varied to change the tangential velocity,

effectively changing the g-load.

Anderson et al. [12] used the circumferential cavity section from Anthenien et al. [9] rig

with a modified center body section shown in Figure 8 containing four equally spaced, simulated

turbine IGV with a RVC on the suction side of each vane. With such a large core flow, a shear

effect was seen that tended to keep hot gas leaving the cavity on the OD of the core, resulting in

a non-uniform exit temperature profile.
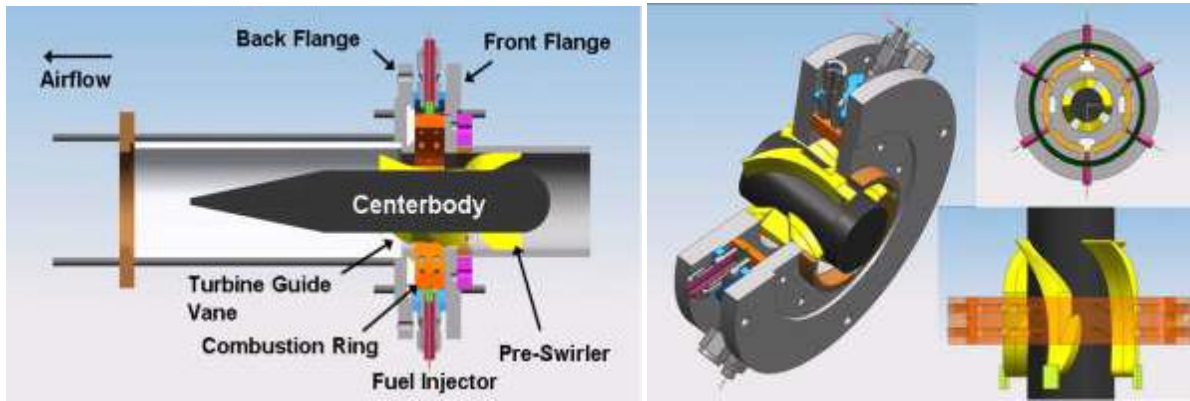
Figure 8. Anderson et al. test setup [12]

The flow direction was varied using JP-8 and Fischer-Tropsch (FT) jet fuels, and CFD

was used to help realize the aerodynamics inside the cavity. Studies showed very different flow

behaviors inside the circumferential cavity whether the flow was swirling clock-wise (CW) and

impacting the pressure side of the vane, or counter clock-wise (CCW) and impacting the suction

side of the vane as shown in Figure 9. CCW flows that impacted the suction side of the vane

caused much more turbulence in the cavity. Specifically, the fuel injection cavities showed

significantly higher flame holding and circulation in the CCW case, which was verified using

high-speed video (HSV), shown in Figure 10. It is important to note there is a mismatch in the

number of vanes and fuel injectors at four vanes to 6 fuel injection locations. This caused the

lack of patterning seen in Figure 9, necessitating the study of a rig with a fuel injection port to

core vane ratio of unity.
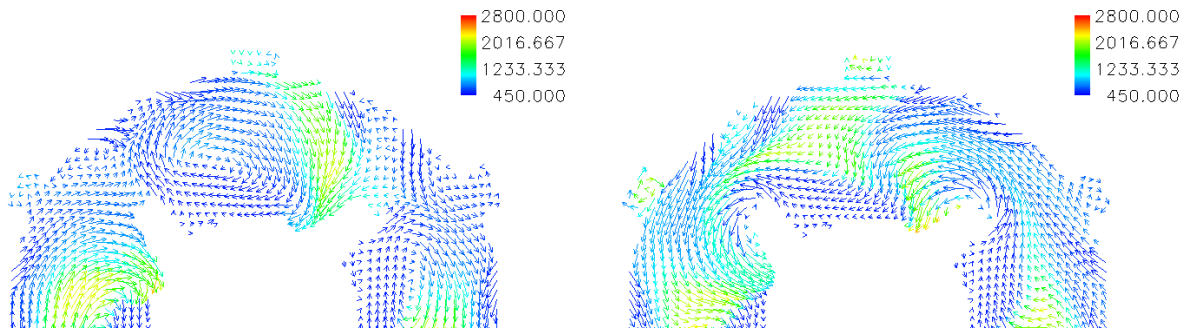
Figure 9. CFD velocity vectors for CW (left) and CCW flows (right) in the cavity [12]
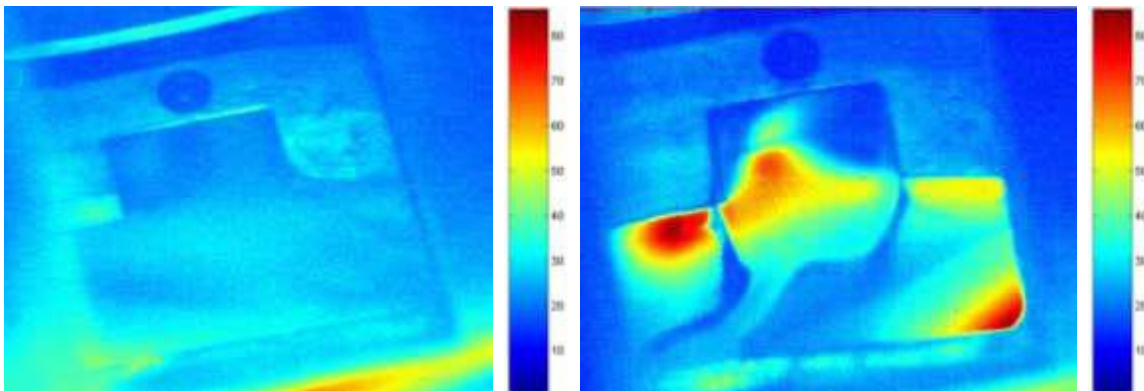
Figure 10. CW flow (left) and CCW flow (right) with flame holding present (based on light intensity)

[12]

Experimental results revealed that no significant differences existed in either lean blow-out or emissions data between the two fuels. However, combustion efficiency in excess of 99% was shown for all cavity equivalence ratios higher than ϕ=1.2 for both the CW and CCW flows. At these higher cavity equivalence ratios, the overall equivalence ratio for the combustor began to approach the stoichiometric condition, leading to increased heat release and therefore thermal efficiency [12]. There was insufficient data to determine if varying g-load would significantly affect emissions results for fuel rich operation, making this a point of great interest for current research. Larger g-loads would be expected to keep products in the cavity longer, increasing the efficiency of the system, until blowout occurred.

At AFIT, Greenwood [13] used the commercial CFD software FLUENT [14] and standard k-ε turbulence models with second order, implicit solvers for steady state solutions and developed the proper heat transfer and fuel injection models and made a comparison of a sector model of the UCC combustor to experimental data from AFRL for the full UCC rig. The model featured a 120° circumferential cavity section with matching radius and air/fuel injection to the AFRL rig, with a one-sixth section (area-based) core flow. He also studied changes in the geometry of the cavity. Anisko [15] improved periodic boundaries of Greenwood's work to include fuel particles, and investigations of further geometric variations.

Moenter [16] built on Greenwood [13] and Anisko's [15] CFD work, but used a model based on a statistical technique known as renormalization group theory (RNG). This RNG k-ε model was intended to provide greater accuracy and reliability than previous models. He evaluated several numerical models at three cases of pressure and mass flow rates to develop both a 2-D flat and curved cavity rig expected to closely behave like the entire UCC in a one-

17

sixth (60°) model, but found a larger section of one-third (120°) was necessary to duplicate full annular characteristics. The combustor's behavior was compared to experiment based on the examination of velocity, temperature and other properties of the flow field at pre-defined locations to give a quantitative measurement. Also, measurements such as efficiency, emissions, temperature distribution and pressure loss across the combustor were used as a qualitative basis of comparison.
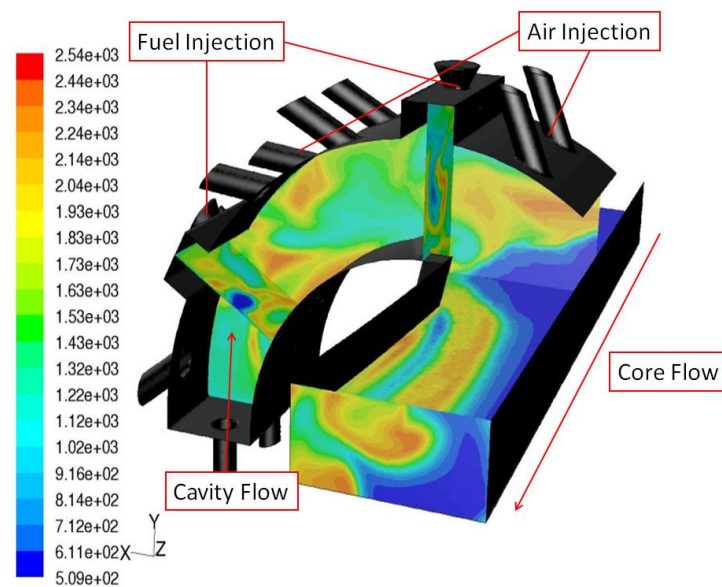
Figure 11. CFD results on AFIT sector model showing temperature gradients (°F) [16]

Anderson [17] used CFD research from Moenter [16], Greenwood [13], and Anisko [15] to design and fabricate a sectional UCC test rig to study both g-loaded and non-g-loaded effects on flow migration from the circumferential cavity to the core section, shown in Figure 11. The core section consisted of a single vane passage (1/6 section) and a 120° g-loaded circumferential cavity.   In addition to the design and fabrication of the rig, Anderson also made significant contributions in the setup of the COAL Lab for experimentation. This included the installation of

air and fuel lines, wiring power and signal lines, setting up the gas analyzer system, connecting the control computer, and writing the initial LabVIEW [18] code to interact with the lab equipment.
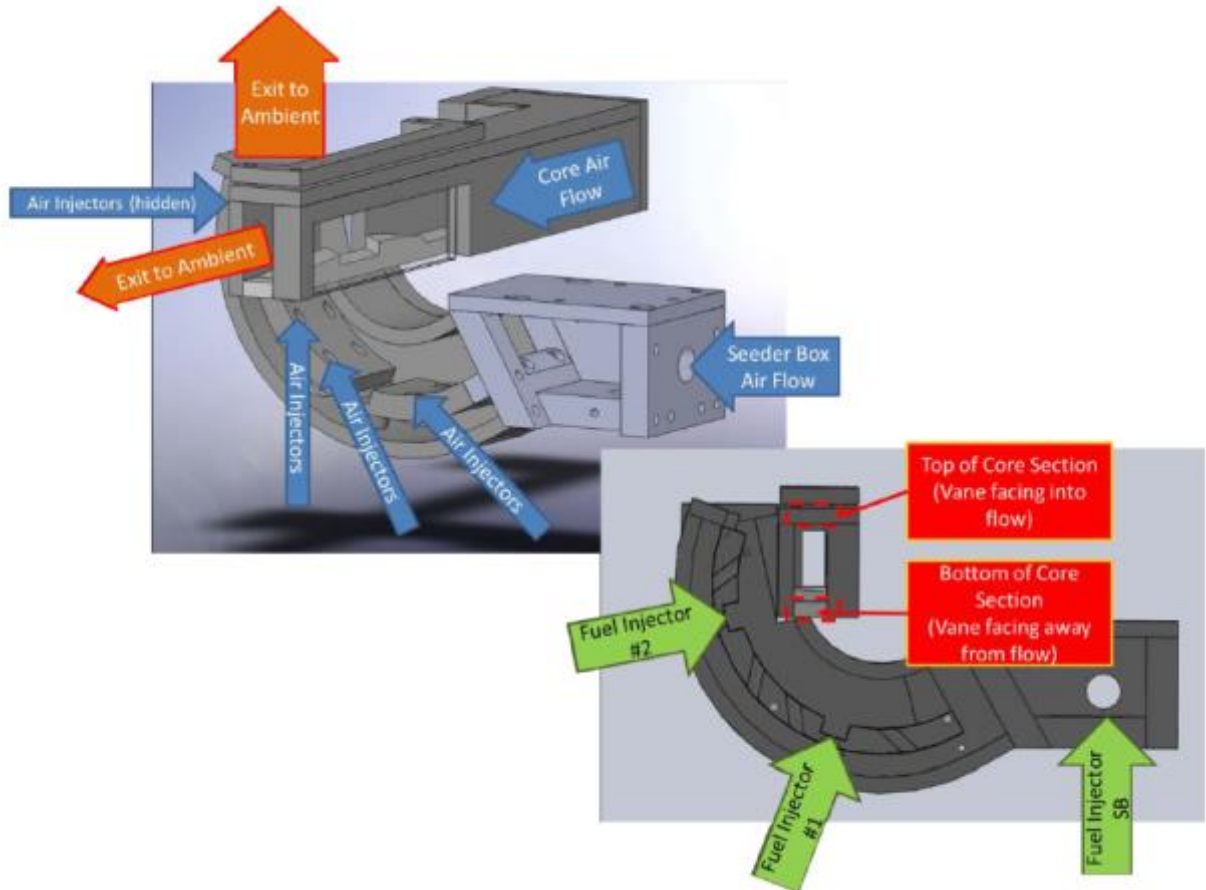
Figure 12. Curved sector rig geometry with addition of seeder/ignition box [19]

The small-scale UCC sectional model developed by Moenter [16] and Anderson [17] was used to study flame migration out of the circumferential cavity into the main flow. LeBay et al. [20], sought to characterize g-loading effects on circumferential cavity flow migration into the axial core flow using high-speed video and laser diagnostic techniques with both g-loaded (via a curved, circumferential cavity section) and non-g-loaded (via straight cavity section) cases with

19

different vane heights. It was concluded that g-loading did positively affect flame migration into the core. The extent was dependent on g-load, vane height, and velocity and mass flow ratios (MFR) between the cavity and the core. With increased vane height (under constant MFR), the velocity ratio between the cavity and the core was effectively increased and the cavity flow was able to penetrate further down the vane into the core flow. LeBay [21] showed that at constant vane height, increasing MFR also led to increased migration along the vane span, shown in Figure 13. For the 28mm vane height, a MFR=0.2 resulted in the most uniform temperature distribution in the core. This was an important condition to maintain turbine life and efficiency. The results of LeBay et al. [20] and LeBay [21] uncovered a notable amount of burning taking place in the core as the fuel rich cavity flow migrated into the air core flow.
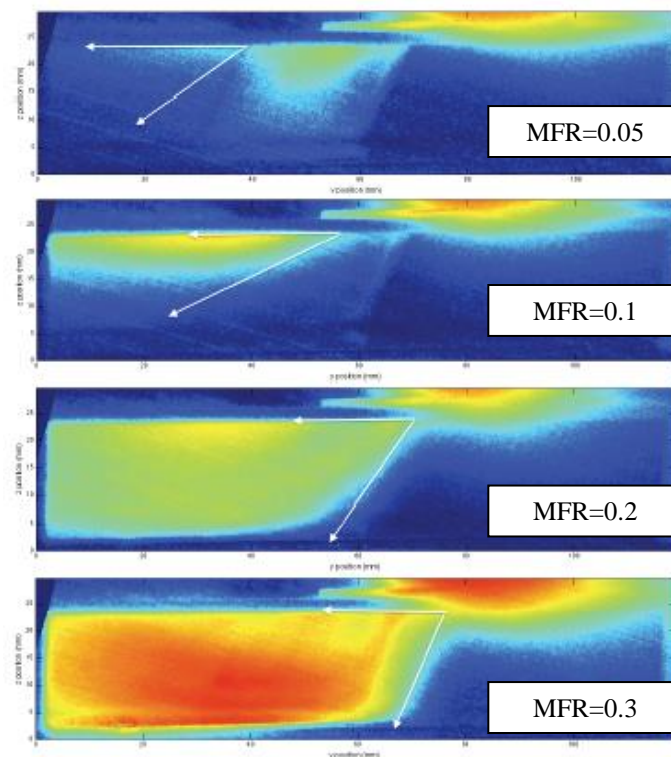
Figure 13. Cavity to core migration flame intensity study using sector rig done by LeBay[21]

Bohan and Polanka [4] developed a hybrid vane that maintained the compressor rotor exit swirl through the UCC and thus minimized the turning needed within the vane section prior to entering the turbine rotor. Traditional combustors require axial inlet flow, which necessitates an exit guide vane section in the compressor to straighten the flow as it enters the combustion section, and a turbine inlet guide vane to turn the flow before reaching the first row of turbine blades. Additional length, and therefore weight, savings come from removing these two vane rows and replacing them with a 'hybrid' vane, as shown in Figure 14. This integration of the compressor and turbine stages within the UCC system significantly reduces both complexity and losses for the overall system. This is comprised of a reduction in diffusion and dump losses exiting the compressor, less viscous losses due to less surface area and lower aerodynamic losses due to less turning.
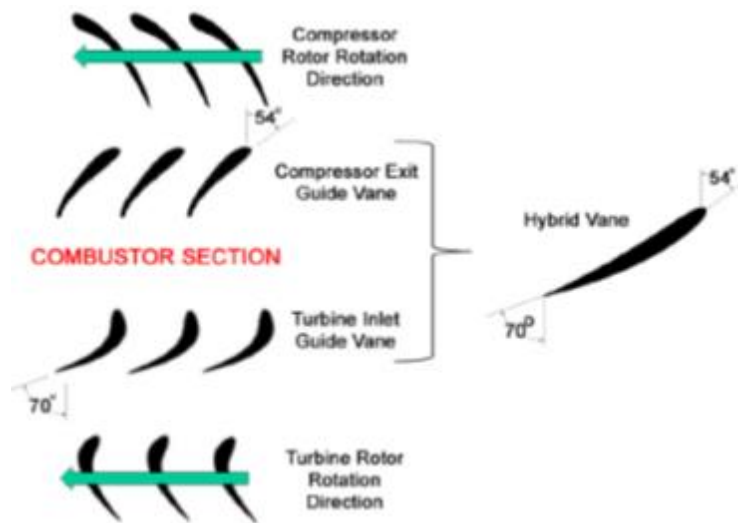
Figure 14. Hybrid vanes replace the compressor exit guide vanes and the turbine inlet guide vanes [4]

Bohan and Polanka [4] also used CFD to study flow migration from the circumferential cavity to the core section in a full annulus model, one much larger than the geometry of the AFIT or AFRL test rigs. This work focused specifically on g-loading, air injection diameter, and vane count effects on the fuel and air species residence time in the circumferential cavity and how they interacted with the hybrid vane upon migration into the core. They found that the cavity g-loading can be directly coupled to the air injection jet diameter, shown in Figure 15, which in turn, influences how long the fuel species stays resident in the cavity before migrating to the core, shown in Figure 16. As the jet diameter decreases the tangential velocity, and therefore the g-loading increases. When the g-load is increased, the fuel will travel further in the cavity before migrating into the core.
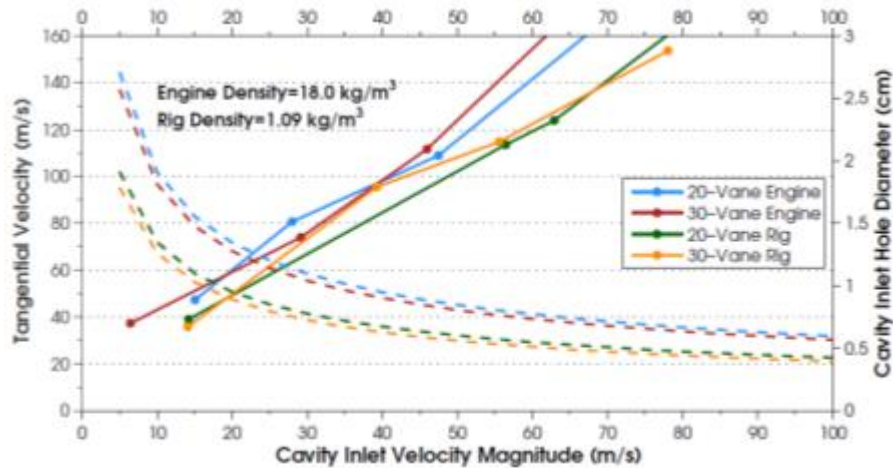
Figure 15. Cavity air injection jet diameter relationship to g-loading and tangential velocity [4]
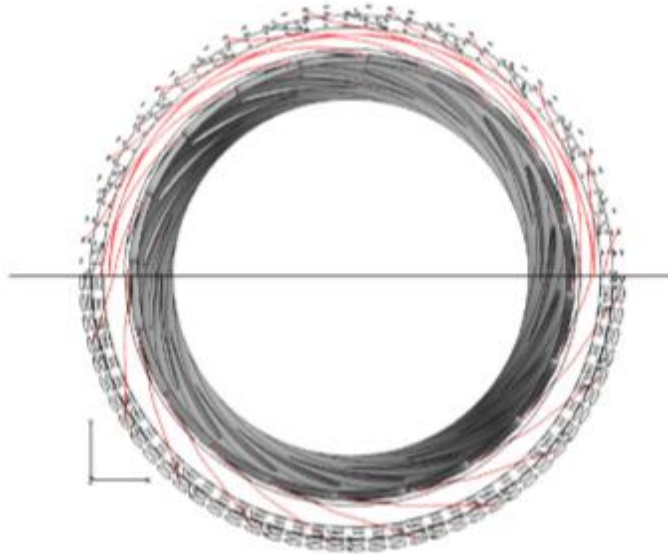
Figure 16. Fuel residence time using baseline jet diameter (top) and 3x jet diameter (bottom) [4]

Parks and Polanka [19] and Parks [22] made several modifications to the AFIT sector rig, including flipping the suction side of the vane to top of the rig based off data from Bohan and Polanka [4] and establishing a flame holding region within the injector/seeder box. Parks then studied ways to desensitize the exit emissions and temperature profile, along with cavity to core migration, by testing a novel "Tiger Claw" RVC concept against a vane with no cavity and one with a typical straight RVC, all three shown in Figure 17.

(a)

(b)

(c)

Figure 17. Baseline (a), standard RVC vane (b), and Tiger Claw RVC (c) vanes studied by Parks [22]

Parks [22] concluded that it was difficult to quantify the difference in flame characteristics when switching the vane from the bottom to the top of the core because the mass transfer was unknown. The flow exited both the circumferential cavity and core, making it extremely problematic to quantify how much mass is coming out of either. However, he saw that the Tiger Claw RVC vane was successful at desensitizing the migration out of the core for some operating conditions, seen in Figure 18, but tended to decrease the mixing between the cavity and the core, impacting the emissions seen at the combustor exit. The standard RVC vane created a helical migration structure inside the core section that promoted mixing and burning, increasing efficiency. The Tiger Claw cavity reduced the strength of this span-wise vortex by turning the flow more axial as it exited the cavity.

24
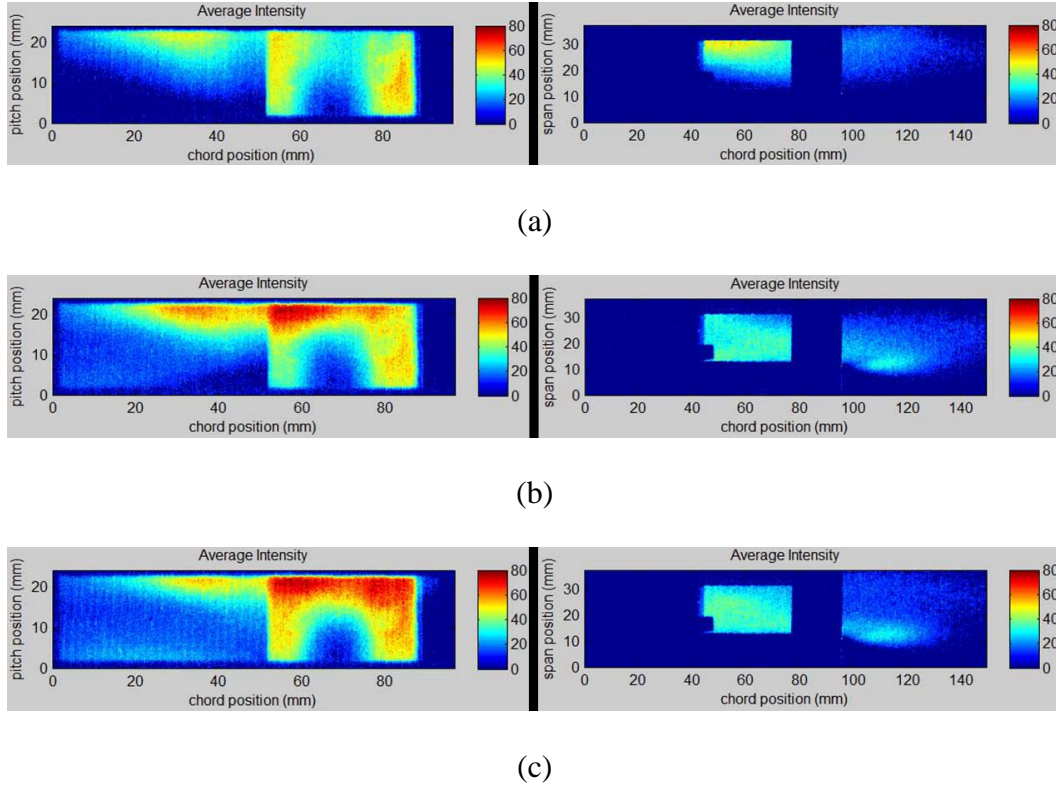
Figure 18. Desensitization of flow using Tiger Claw RVC vane for (a) MFR=0.1, (b) MFR=0.2, and (c)

MFR=0.3. [22]

2.3. UCC Integration into Engine Hardware

In an attempt to integrate a UCC into an engine for a practical application, an engine

manufacturer, Spytek, outfitted a Spytek JI-304 dual spool turbo jet with a UCC configured as an

ITB [23]. The main engine (radial compressor, reverse flow burner, axial turbine) provided

vitiated air to the UCC-ITB, with a secondary turbine to drive an axial boost stage upstream of

the engine main radial compressor (acts like a boost stage for the main compressor), shown in

Figure 19. Between 0-50% of the total air mass flow was diverted into the ITB over testing, with

the optimum number for the setup being 23%. At a total fuel-to-air ratio 0.008 and 23% air

diversion, temperature rise over the baseline (ITB off) was 588° K. Because the ITB drives the

axial boost, air mass flow, as well as shaft speeds, increased with increased ITB fuel input. This indicated the presence of combustion products that have the ability to drive a second, lower pressure turbine that could do work in the system [23]. LBO was found to be around 0.006 overall fuel-to-air ratio (OFAR). Equivalence ratios in the cavity from 0.57 to 0.79 were tested by adjusting air flow splits. Report cavity velocities of 37.7 m/s at their operating range (23% mass flow of air), with a loading of 2300. Auto ignition was found to be possible in the cavity for certain test conditions, however, at the optimum air mass flow split of 23%, a spark ignition was required, which was accomplished by two spark plugs 180° from one another in the cavity.
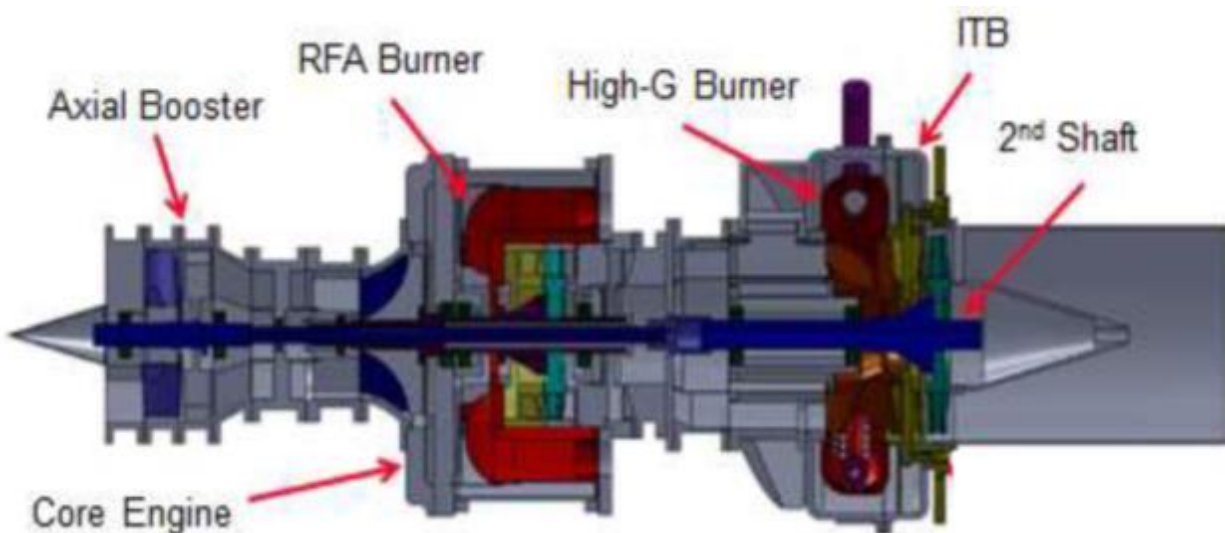
Figure 19. Spytek JI-304 outfitted with UCC ITB system to drive an axial boost stage [23]

2.4.   Rayleigh Loss

When heat is added to a constant area, subsonic flow field, the Mach number, velocity, and total temperature increase, while static and total pressure decrease [24]. Total pressure loss due to heat addition is called Rayleigh loss and the total pressure ratio [24] is given by

26

$$\frac{P_{o2}}{P_{o1}} = \frac{1 + \gamma M_1^2}{1 + \gamma M_2^2}\left(\frac{1 + \frac{\gamma - 1}{2}M_2^2}{1 + \frac{\gamma - 1}{2}M_1^2}\right)^{\gamma/\gamma-1}$$

Equation 4

where P_o is the total pressure, M is the Mach number, γ is the ratio of specific heats, and *1* and *2* refer to the conditions before and after heat addition, respectively. Typical combustor setups diffuse incoming flow down to low Mach numbers to avoid these pressure losses while burning.

Radtke [25] used a modified version of the Anthenien et al. [9] rig to study pressure losses in the combustor due to Rayleigh effects. Radtke saw this increase in Mach number when comparing reacting and non-reacting cases, seen in Table 1, where the temperature factor is the multiplication factor between the inlet temperature and exit temperature. The Rayleigh loss incurred from heat addition were calculated by

$$\left.\frac{\Delta P_{o,1-2}}{P_{o,1}}\right|_{Rayleigh\ Loss} = \left.\frac{\Delta P_{o,1-2}}{P_{o,1}}\right|_{Hot} - \left.\frac{\Delta P_{o,1-2}}{P_{o,1}}\right|_{Cold}$$

Equation 5

where hot and cold refer to the reacting and non-reacting cases, respectively, and $\Delta P_{0,\ 1-2}$ is the difference between the initial, *1*, condition and the final, *2*, condition. Rayleigh losses were under 2% for all four cases. These losses were minimal, as the inlet Mach numbers were below Mach 0.1.

Table 1. Rayleigh loss measurements on AFRL experimental rig [25]

Inlet Mach #	Temperature Factor between Inlet and Outlet	Reacting Exit Mach #	Non-Reacting Exit Mach #	Rayleigh Loss
0.071	2.94	0.2785	0.1285	0.779%
0.089	2.93	0.3223	0.1616	1.048%
0.071	3.44	0.3245	0.1271	1.175%
0.089	3.41	0.3845	0.1591	1.738%

CFD research done by Bohan and Polanka [4] focused on flow migration from the UCC cavity into the hybrid vane section on a 76.2 cm diameter, full annular model using periodic boundary conditions. By design, the compressor exit Mach number, Mach 0.3, was maintained through the entire vane section. The goal of this design was not to achieve a representative turbine rotor inlet Mach number of 0.8, but to simply study migration out of the circumferential cavity. While lower aerodynamic losses were shown with this design, pressure losses due to Rayleigh effects at Mach 0.3 were approximately 12% according to the CFD model analyzed by Johnson [26]. As shown by Table 2, the typical pressure drop in a conventional combustor is roughly double the aim of advanced combustor designs. The allotted pressure drop for CFD UCC model was exceeded by the Rayleigh loss alone for a current turbine engine system [1]. Therefore, the local Mach number at the cavity-core flow interface needs to be reduced to decrease Rayleigh loss and enable the UCC to be viable for future engine systems [27].

Table 2. Typical engine pressure losses in the combustor and goal of future combustor systems [27]

Component	Conventional Pressure Drop	Advance Combustor Design Goals
Compressor EGV	1%	
Compressor Exit Diffuser	3%	One component with
Combustor	4%	total of approximately 5%
HPT Vane	2%	pressure drop
Total	10%	~5%

Johnson created an exaggerated model in which the core area where burning from the cavity occurred was dramatically increased, shown in Figure 20. Using the same axial length and cavity dimensions, the increase in area, in theory, dramatically reduced the Mach number, and therefore decreased the Rayleigh loss in the system. The model proved that it was possible to

mitigate Rayleigh loss under 1% with an area change. However, the dramatic increase in area in such a small axial distance led to separation and aerodynamic losses that overwhelmed the system, leading to the conclusion that the geometry needs to be optimized to give the lowest total losses, taking both aerodynamic and Rayleigh losses into account.
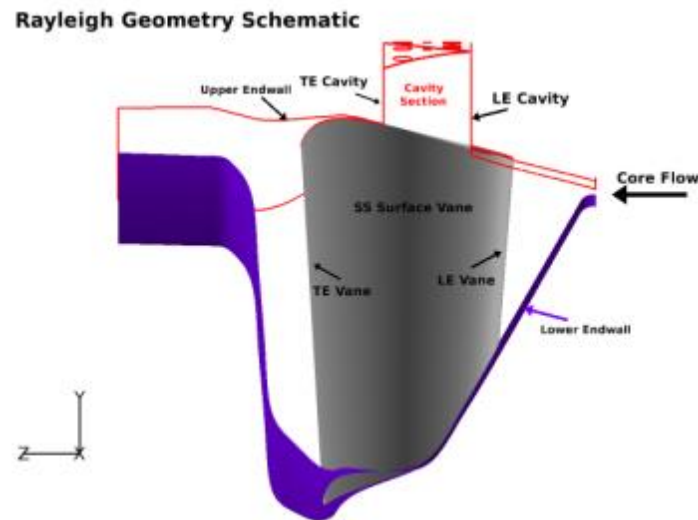
Figure 20. Exaggerated low Rayleigh loss geometry by Johnson in CFD model [26]

2.5. Cooling

In order to extend the life of hardware, cooling is often used in high temperature test rigs. Initial lighting of the new AFIT UCC test rig showed significant heating on the back face. To remove some of this heat, cooling methods were studied, specifically convective and impingement cooling techniques. Convection is the process of removing heat via fluid moving over a surface, and includes the advection from bulk fluid velocity, and the random motion of fluid particles [28]. Impingement cooling is a form of convective cooling that directs fluid

normal to the surface, instead of over it, enhancing the fluid's convective properties [28]. The heat flux for convective methods is given by

$$q'' = h(T_s - T_\infty)$$

<div align="right">Equation 6</div>

where h is the convective heat transfer coefficient, T_s is the temperature of the surface being cooled, and T_∞ is the temperature of the fluid. The convective coefficient, however, is much higher generally for impingement cooling [28].

Glynn et al. [29] studied the effects of jet diameter, Reynolds number (Re), and jet target spacing on the heat flux of impinging air and water jets on stainless steel foil. A DC current was passed through the foil to heat it to a constant temperature. The cooling fluid was then injected through an orifice plate at the foil while a FLIR ThermaCAM A40 infrared (IR) camera with a 50μm lens imaged the back side of the foil to measure the temperature gradient. Reynolds number was calculated using

$$Re = \frac{4\rho Q}{\pi d \mu}$$

<div align="right">Equation 7</div>

where ρ is the density of the cooling fluid, Q is the volumetric flow rate, d is the jet/nozzle diameter, and μ is the dynamic viscosity. Results showed that high Re, small diameter (therefore high velocity), and minimum distance between the nozzle and surface increased heat transfer coefficient, h, while the opposite characteristics reduced h, as shown in Figure 21. Glynn et al. concluded that the results showed arrays of small diameter impinging jets were one of the more attractive options for cooling [29].

(a)

(b)

(c)
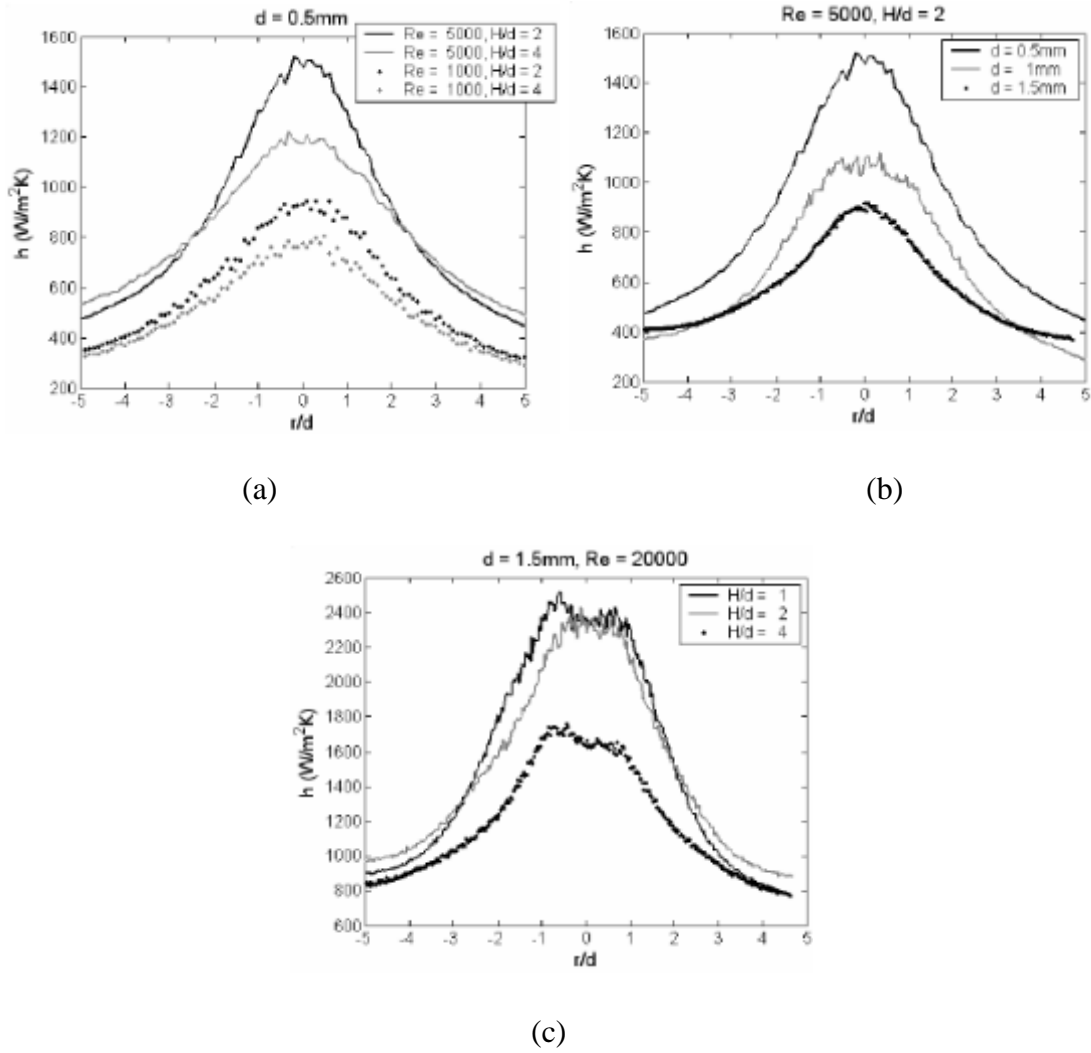
Figure 21. Heat transfer coefficient for (a) multiple Re number, (b) jet nozzle diameters, and (c) height

from orifice to surface [29]

San and Lai [30] investigated the optimum spacing between each nozzle in a staggered

array of impinging air jets in terms of Nusselt number (Nu) given by

$$Nu = \frac{qd}{k(T_w - T_{aw})}$$

Equation 8

where q is the local heat flux, k is the thermal conductivity (of air), and d is the jet diameter, T_w is the wall temperature, and T_{aw} is the adiabatic wall temperature. As the Nusselt number increases, the more effective the cooling scheme. Spacing between nozzles, Reynolds number, and distance from the impinging jet nozzles to the surface being cooled were varied. It was shown that jets too close together or too far apart had detrimental effects on cooling, shown in Figure 22, due to jet interactions (a) or the fountain affect (b) which re-circulated hot air into the jet streams. Results showed greater cooling effects for higher Reynolds number flows with the jets situated closer to the surface. The distance from the surface the jets were positioned also had significant impact on Nusselt number, with smaller height-to-jet diameter ratios giving the highest value, seen in Figure 23.

(a)

(b)
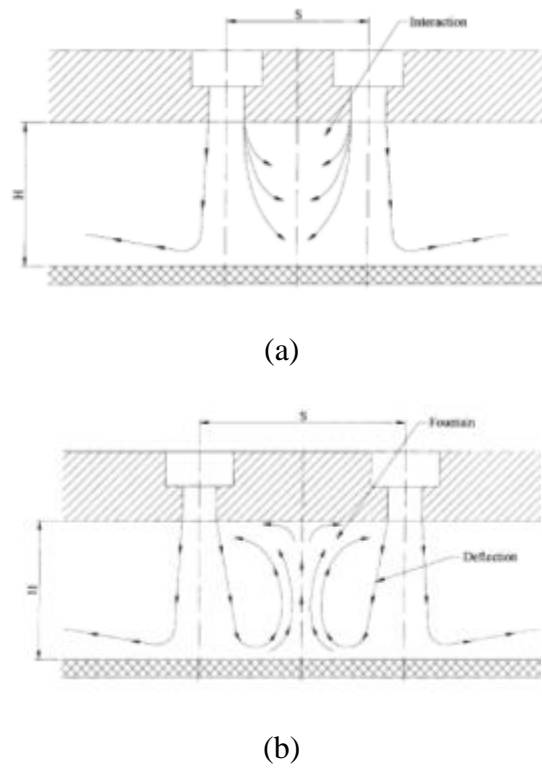
Figure 22. Jet interference with (a) close spacing and (b) hot gas fountain/recirculation with further spacing [30]
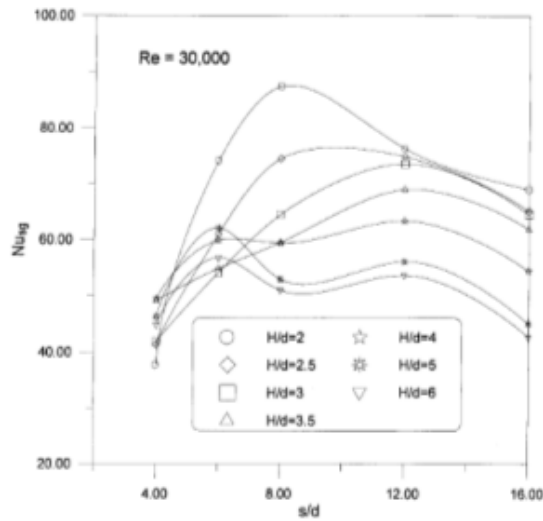
Figure 23. Nu number for Re=30,000 at multiple jet orifice to surface heights [30]

2.6.   High Speed Video and Imaging of Flame Structures

In most exothermic reactions, energy is emitted as both heat and light, and the emission of light is referred to as chemiluminescence. High speed imagining of these reactions with various wavelength filters can allow observation of OH and CH radicals, as well as C_2 and CO_2. Tracking these types of species can lead to identification of reaction zones [21] and the study of flame structure within the circumferential cavity and core exit.

Stojkovic et al. [31] used a high speed imaging system to locate OH radicals within the reaction zone of an internal combustion engine based on chemiluminescence. Cross et al. [32] researched oscillations in flames for natural gas/air flames. Similar techniques were used again by Cross et al. [33] to study Jet-A/air flames by using only the green and blue channels of a high speed video system since C_2 and CH only emit in green and blue spectrums, where the green wavelength falls between $450 - 510$ nm and blue falls between $510 - 570$ nm [33].

33

LeBay et al. [20] and LeBay [21] used time-averaged intensity measurements of images taken using a Phantom V12.1 high speed camera to find approximation location of CH production, and therefore flame fronts, in the AFIT small-scale, sectional UCC test rig, shown in Figure 24. This allowed for estimations on the migration path as flow left the circumferential cavity and entered and mixed with the core flow. This was also used to characterize the unsteadiness of the flame.
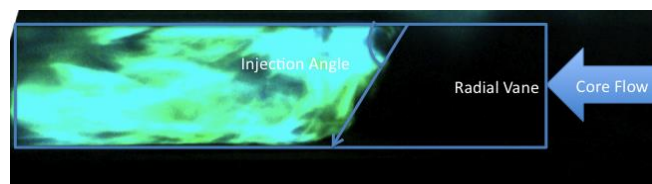
Figure 24. High speed video image of cavity migration angle into the core stream [20]

Parks and Polanka [19] used the Phantom V12.1 color camera and a 65 mm lens with the modified UCC core section while attempting to desensitize the flame structure and migration path from operating conditions. The camera was used to capture the flame structure as it moved in the core, and an intensity study revealed how the flow reacted to different operation conditions for each of the given radial vane/ radial vane cavities.

2.7.   Limitations of Previous Work

The previous work done on both the AFRL and AFIT UCC test rigs each had limitations to the experimental research that could be done. While each provided insight into the dynamics of the UCC, neither could be used to fully characterize all parts of the combustion process while replicating the flows that were expected in an engine system. The AFRL test rig gave poor visibility into the circumferential cavity, seen in Figure 25, and did not replicate the hybrid vane

system constructed by Bohan and Polanka [4]. It also had limited instrumentation for pressure

and temperature measurements, more of which was needed to characterize the rig completely.
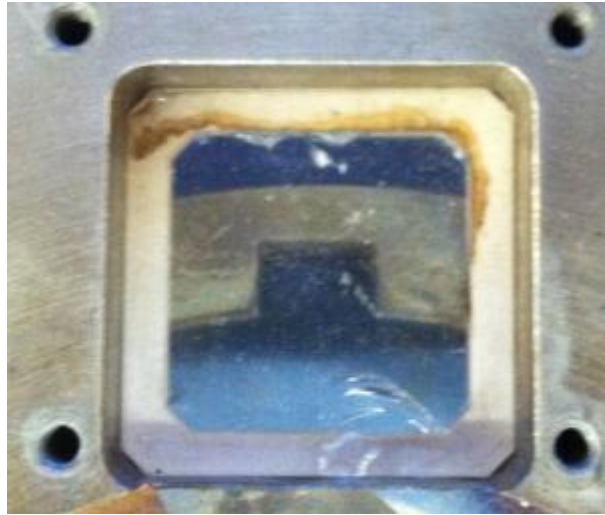
Figure 25. AFRL UCC limited cavity optical access

The AFIT test rig used by LeBay et al. [20], LeBay [21], and Parks and Polanka [19] was

also limited in that it was a sectional model. This rig was created to study fundamental principles

of a g-loaded cavity system because the UCC was still in infancy during the time this rig was

built. The exit area of the cavity ultimately dictated how much migration occurred from the

cavity to the core stream, making migration a function of cavity versus core pressure, not the

desired density gradient of the cavity. Experiments done (and discussed in more detail in

Appendix A) showed that the desired entrainment was not achieved and therefore the migration

was not representative of a full-annulus rig. The single passage core section also only

represented a flat vane surface and did not replicate the pressure gradients or Mach number

distributions found in a real airfoil. Many fundamental concepts were studied using this rig, but

it was not suited to accomplish the desired research objectives outlined in this paper.

III.   Experimental Setup

To facilitate better understanding of the characteristics of UCCs, a full-annulus test rig was designed and built and dramatic changes were made to the COAL Lab. This chapter is dedicated to the design and installation of the new test rig, as well as the implementation of necessary instrumentation, support hardware, and control systems to effectively operate and characterize the UCC.

3.1.   Annular Rig Requirements

As discussed in the previous chapter, the sector rig's ability to accurately replicate a UCC was limited to very fundamental studies, specifically lacking in the area of mass flow extraction from the cavity to the core. For this reason, a full annular rig became the nominal design point. A full annular rig would be able to represent the engine condition and give accurate mass migration changes based on g-load. To more accurately represent the flow requirements in an engine, flow Mach number of 0.35 with 35° swirl at the inlet and Mach number between 0.7-0.8 with 70° swirl at the exit of the core were desired at 0.45kg/s of air (based on an initial 70/30 core-to-cavity air split). Independent air control over the cavity and core would allow the mass flow ratio between the two to be changed in order to find the optimum operating point. Optical access and instrumentation would be increased over previous rigs so that a more complete characterization could be done for both liquid and gaseous fuels. Finally, the entire rig would be modular, such that parts could easily be swapped, and the rig could be used as an ITB [34].

3.2.   Initial Air Flow Modifications and Upgrades

Parks [22] specified and purchased a new Ingersoll Rand H50A-SD, 50 hp, oil-free compressor to provide up to 1 kg/s of air at atmospheric pressure, or up to 0.1 kg/s at 862 kPa,

and was installed outside of the COAL Lab East wall as seen in Figure 26. This compressor

contained built-in dryers to remove any condensation in the air and provided the core air required

for a large sized UCC test rig, initially designed around Bohan and Polanka's [4] CFD model,

seen in Appendix B. This complimented the two existing AFIT 50-hp Ingersoll Rand air

compressors capable of providing 0.15 kg/s (total). It was necessary to plumb an additional

airline because existing air supplies were sized for much smaller quantities of flow. The new,

7.62 cm line was controlled by a Flowserve MaxFlo 3 valve capable of 0.6 kg/s max flow rate

and included a Fisher 99 pressure reducing valve that was purchased and installed to drop the

pressure from the compressor to the desired line pressure so the necessary mass flow could be

achieved. Flow rate was measured and transmitted to the control station from a FT2 Fox Thermal

Instruments flow meter.

Figure 26. Ingersoll Rand H50A-SD Compressor installed outside COAL Lab

The existing 3.81 cm air line was upgraded with a Flowserve MaxFlo 3 valve capable of

flowing 0.3 kg/s max flow rate and Fisher 299H pressure reducer, replacing the smaller flow

and pressure controllers. The new valve and regulators were equipped to handle higher flow rates and would be less likely to be choked at the connections, a problem seen in the previous experiment. The 1.91 cm line was unchanged, using an ITP and Badger control valve and Cashoo pressure reducer, and could flow 0.03 kg/s max, allowing for the total system to flow up to 1 kg/s over three different air lines. The two smaller lines both had FT2 Fox Thermal instruments flow meters to give feedback on the mass flow through each. This provided independent control over the different air inlet sites on the rig so that air flow parameters can remain independent of one another for UCC characterization purposes.

The valves, regulators, and flow metering systems were installed on the North wall of the COAL Lab, shown in Figure 27. A hand-valve system was installed upstream of the three lines to allow a different air source for the two smaller lines, or a common source for all three, shown in . The FT2 flow meter boxes were calibrated by the manufacturer and were used as a calibration for the control system. This allowed for precise control of the system with an accuracy of +/-1% of the measured value. To control each air line, a Eurotherm 2404 PID controller was used with the control station computer running LabVIEW [18]. An analog 0-5 VDC set point signal was transmitted from the control computer to the PID controller which was then relayed to the line control valve via a 4-20 mA signal. The FT2 flow meter measured the flow and transmitted a 4-20 mA signal back to the PID, where the control value was automatically adjusted to accurately reflect the actual flow and desired set point.
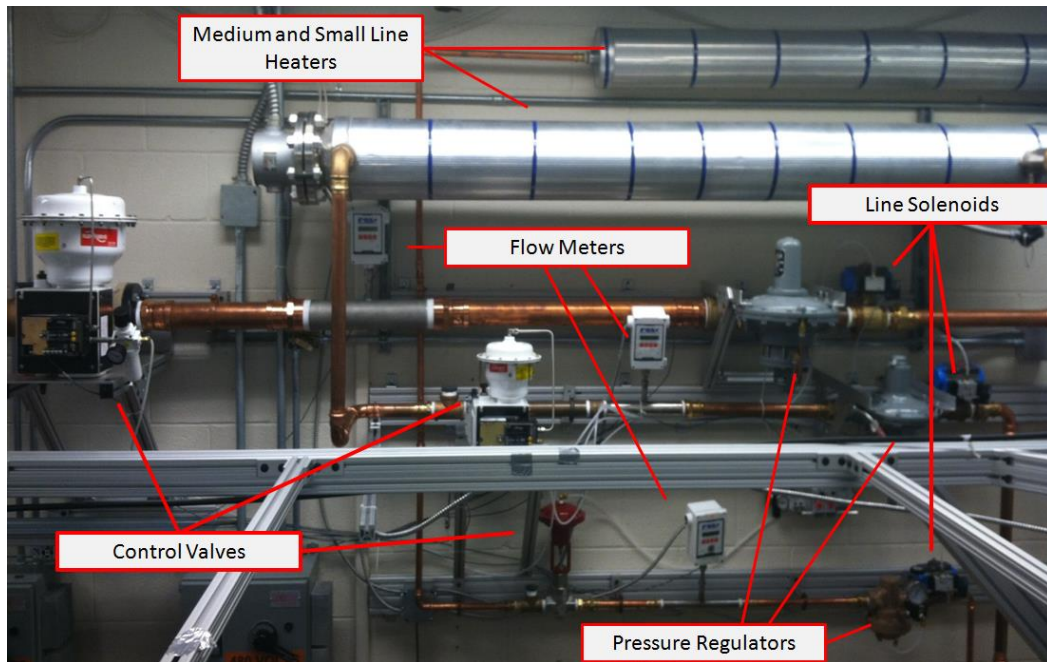
Figure 27. Air system setup on the North wall of the COAL Lab
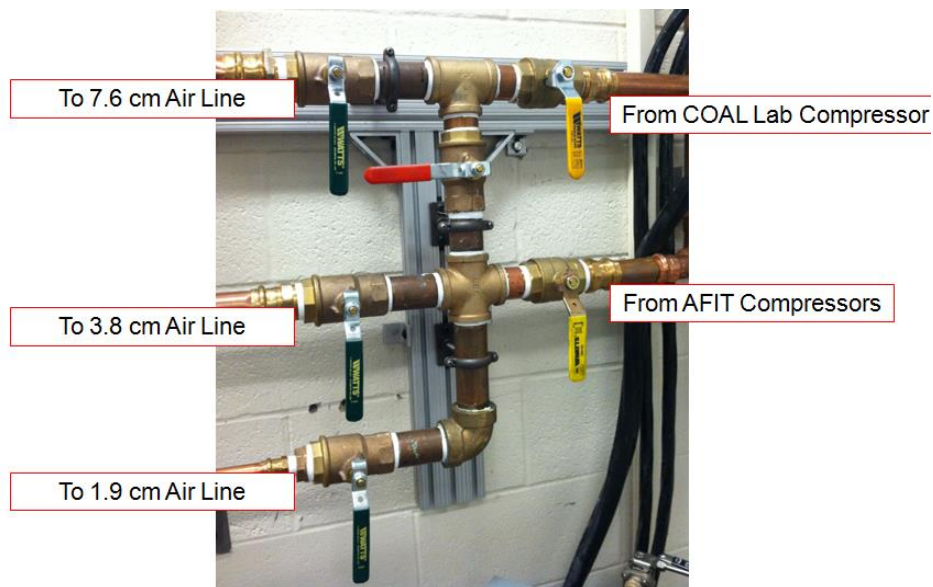
Figure 28. Valve system to source air flow from desired compressor

Important to note is that the Fisher 99L regulator on the 7.82 cm line requires a downstream feedback into the main valve between the regulator and the control valve to balance the pressure correctly. Without this feedback, the regulator will not be able to sense the correct pressure downstream, and will over pressurize the downstream line, which is detrimental to the integrity of the regulator itself. The regulators on the smaller two lines do not require this feedback.

3.3.   Full Annulus Ultra Compact Combustor Design and Setup

Due to the limitations of the sectional UCC rig, a larger radius, full annulus test rig was designed and built for to carry out the main objectives of this research to ensure relevant results. This rig focused on accurately representing the flow conditions for a main combustor application. The following section includes an overview of the chosen design, shown in Figure 29, and its main features and components, which include the core inlet, the circumferential cavity, the center bodies, and the core exit.

The inlet of UCC was designed to handle typical compressor rotor exits at Mach 0.35 and 35° swirl [1]. The passage span at the inlet was also desired to be large enough to simulate actual engine geometry at a height of 2.03 cm, dictating a core mass flow of 18.9 kg/min, well within the capability of the 7.62 cm air line. Previous research dictated a 70/30 core-to-cavity split was a good starting point for study and optimization purposes, so the cavity size was designed for 8.1 kg/min of air to reach a g-load of 2,000. The design point for cavity equivalence ratio was between 1.5-2.0, which gives a minimum overall fuel-to-air ratio (OFAR) of 0.45, such that g-load and equivalence ratio were in the stable regime from research performed by Zelina et al. [3, 10, 11] and flow capabilities for both fuel and air allowed for off design studies by upping or

lowering mass addition to the rig. The hybrid vane section, which was designed to mimic that of Bohan and Polanka [4], turned the 35° flow to 70° for the inlet to the first turbine rotor stage. The flow must also be accelerated to Mach 0.7-0.8 at the exit in order to drive the first turbine rotor in a typical engine [1].

(a)

(b)
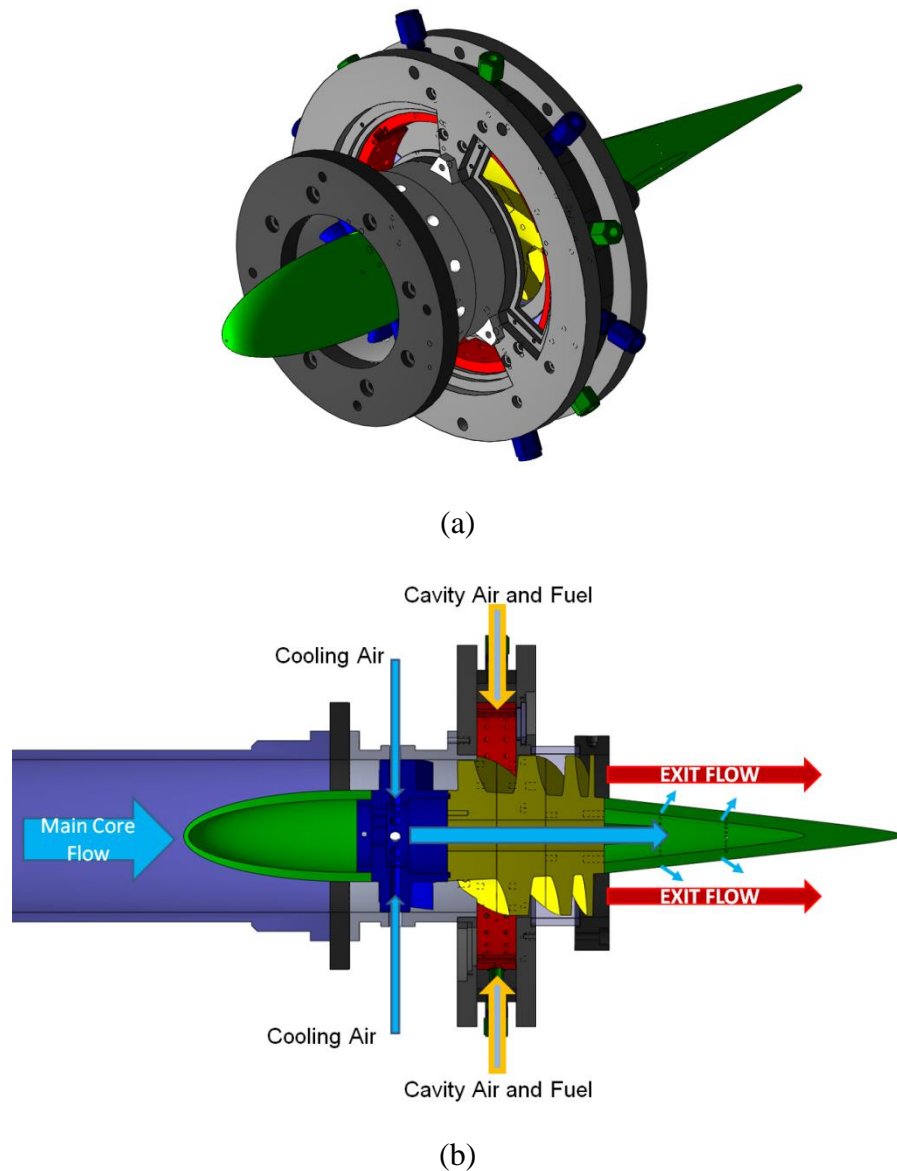
Figure 29. Full annulus UCC (a) design and (b) main flow path

3.3.1. Inlet and Compressor Rotor

The larger percentage of airflow to the test rig that supplies the core flow is taken from the 7.62 cm supply line. This line is brought to the inlet line via a flexible plastic tube, where it is turned horizontal and expanded to 10.16 cm, and travels 122 cm, roughly twelve diameters, in a PVC pipe before entering the rig, reducing vortices and non-uniformity in the flow, shown in Figure 30.
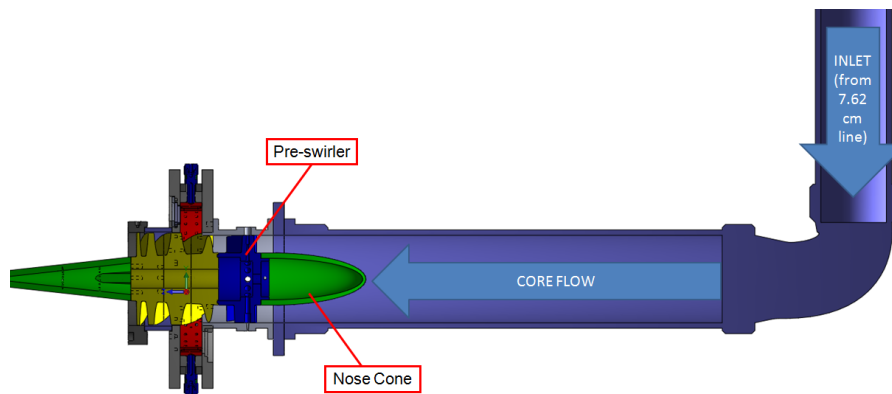
Figure 30. UCC Inlet Diagram

Flow enters the rig from the plastic pipe via an elliptical, aluminum, nose section that directs the flow into a 2.04 cm passage where flow accelerates to Mach 0.35 and twelve turning vanes that impart the a 35° swirl to the axial flow before entering the rest of the rig. The pre-swirl section attaches to the outer inlet shroud and holds the main center body section in place. It also provides inlets for cooling air passage that routes through the pre-swirl body into the main center body and tail, diagramed in Figure 29. The core air is ambient temperature enabling the front section of the rig to be made with lighter materials that are more easily machined.

3.3.2. Circumferential Cavity

The circumferential cavity section is shown in Figure 31 and constitutes the main combustor chamber. Fuel and air are brought in and burned in the circumferential direction at a diameter of 15.85 cm. Air is brought in from the smaller, 3.81 cm air supply into an outer plenum at six locations that drives 48 paired, air injection holes 35° to the tangent direction on the inner ring. The air injection jet diameter was set at 0.35 cm for the baseline case, but the ring was removable to allow different air driver configurations and diameters to be studied. The cavity size was initially designed at 2.54 x 2.54 cm, giving a cross sectional area of 6.45 cm^2, nearly 50% larger than the AFRL rig, and served as the baseline cavity size. The width of the cavity can be changed by fabricating new outer and inner cavity rings to study effects of widening the geometry and increasing the area of the cavity and find a more optimized point.
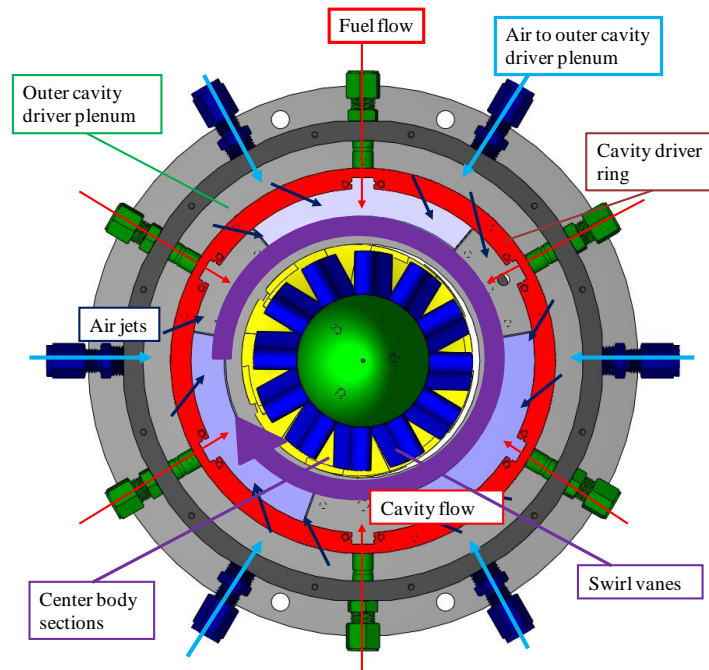
Figure 31. Circumferential component layout and flow diagram [34]

Fuel is injected into six, equally spaced 1.02 x 0.51 cm fuel cavities via six fuel plugs shown in Figure 31. When using liquid fuels, a peanut-style nozzle is attached to the fuel plug, shown in Figure 32, which atomizes the fuel as it is injected into the fuel cavity, allowing it to mix with air before being entrained into the circumferential cavity flow and burned. Liquid fuel control is provided by a dual ISCO Model 1000D, syringe style liquid pump system, capable of providing continuous fuel flow up to 408 mL/min. For gaseous fuels, a baffle plate with eight smaller driver holes is inserted into the fuel cavity, creating a fuel plenum that breaks up the momentum of the fuel flow coming in from the fuel plug, shown in Figure 33. Parks [19] and Parks and Polanka [22] saw that at high flow rates of fuel, the momentum from a single fuel port could cause fuel to exit the circumferential cavity before it was fully burned, necessitating breaking up the single stream into multiple streams with lower momentum/ flow each. Liquid propane is supplied from four 150 gallon tanks and is converted to gas via two Zimmerman LPG electric propane vaporizers in the tank farm, shown in

Figure 34, capable of handling 0.67 kg/min of propane each. The gas is metered at the gas control box by two 200 SLM MKS mass flow controllers (MFC). Each of the two lines feeds three equally spaced fuel ports on the rig, such that an even distribution is always attained, even if one of the flow controllers sees a variation or fluctuation that the other does not.
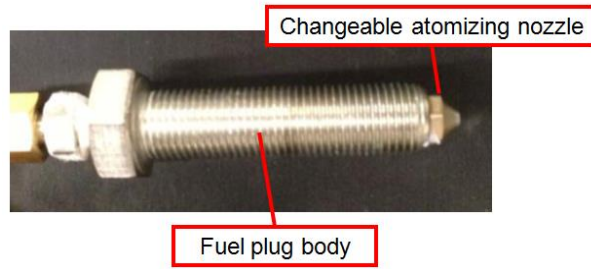
Figure 32. Fuel plug with atomizing nozzle attached [35]
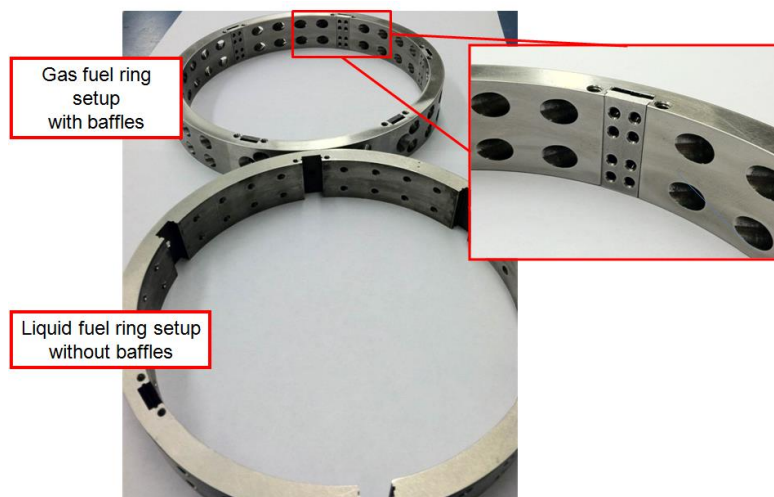
Figure 33. Liquid fuel and gaseous fuel ring setups
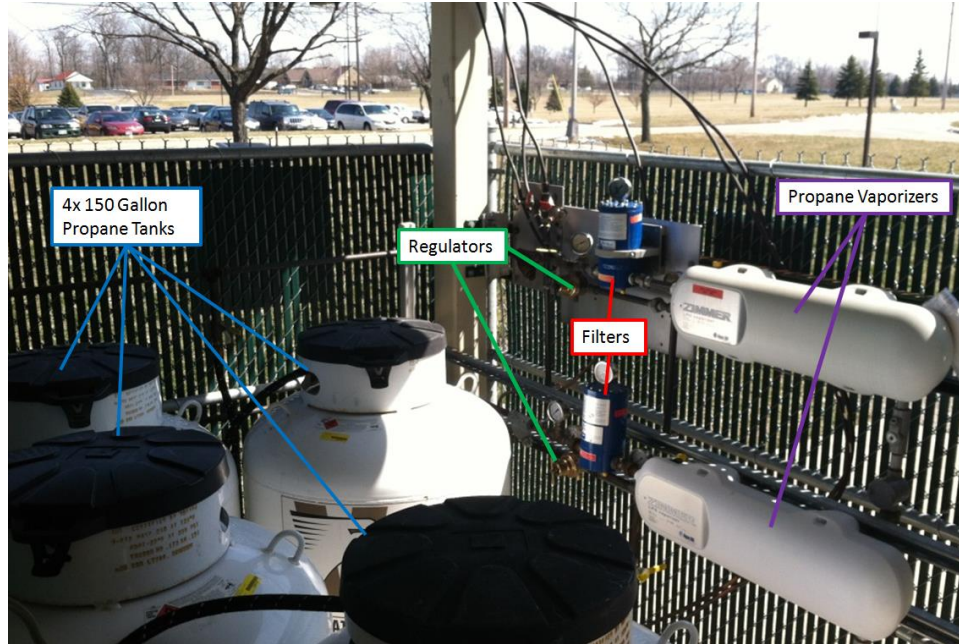
Figure 34. Propane tanks and Zimmerman LPG propane vaporizers

The optical access to the circumferential cavity was greatly increased over that of the Anthenien et al. [9] test rig. Three, equally-spaced, 90° optical access ports (OAP) were designed on the front face, and three, offset but also equally-spaced, 80° OAPs on the back face allow for full optical characterization of the entire UCC cavity and multiple overlap points for laser diagnostics and high speed video data. Quartz pieces were used to gain optical access into the cavity. The front and back OAPs could also be clocked such that they line up directly on top of one another, giving through access for use with Phase Doppler Particle Analyzer (PDPA) and other diagnostic systems. The quartz is protected from the metal via Fiberfrax® refractory ceramic felt, which provides both a tight seal between the two surfaces, as well as insulation from excess heat.

Figure 35. Optical access section at the front of the UCC with overlap from back windows

In addition to quartz windows, instrumentation block (IB) were also made in order to allow pressure and temperature measurements to be made in the cavity. The front IB had nine tap locations and the back IB had seven, all at mid radius of the cavity at different circumferential locations, shown in Figure 36. Blank plates could also be substituted for the instrumentation plates or windows for testing that did not require optical access into the cavity.
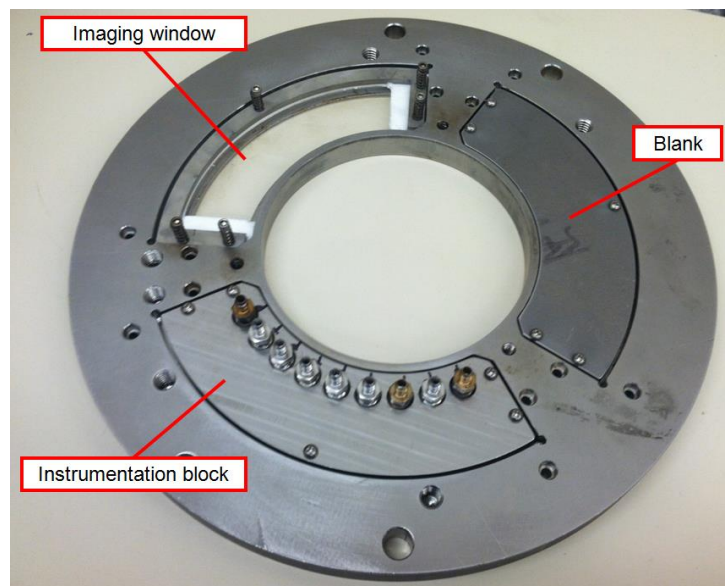
Figure 36. Three different OAP configurations on the front face

An ethylene- air torch shown in Figure 37, which was used previously for the small-scale circumferential rig, was used to initially ignite the circumferential cavity flow. Shop air and ethylene are brought in to a stainless steel manifold and are ignited via auto spark plug. The flame is injected into the cavity via stainless tube on the back cavity plate at one of the fuel inlet port locations inside the fuel cavity. Due to the increased optical access, location for the igniter was limited but initial testing done by Wilson and Polanka [36], Wilson et al. [37] and Conrad [35] showed its effectiveness to combust reactants in the circumferential cavity effectively.
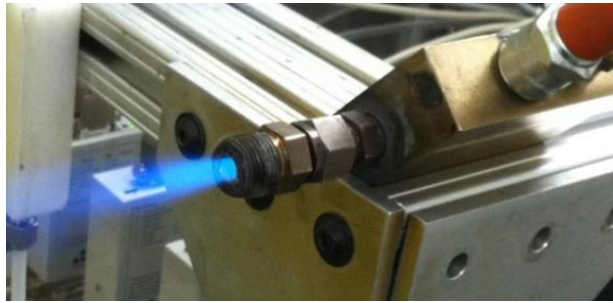
(a)
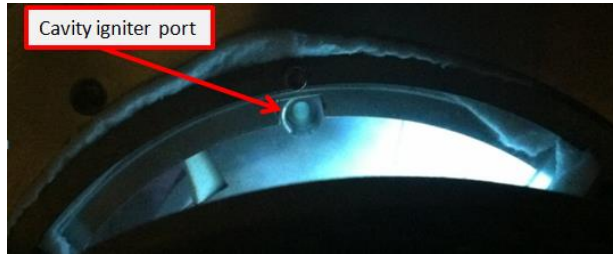
(b)

Figure 37. Ethylene-air torch (a) test and (b) location within the UCC circumferential cavity

The circumferential cavity is contained by two parallel plates and two rings that make up the inner cavity and the air plenum. Hastelloy-X is a nickel-based alloy that was chosen for the material as it has extremely low thermal expansion coefficient between 15.6 and 16.7 µm/m°C at

1000°C (1273 K) [38], much lower than 316 stainless steel, which is nearly 20 µm/m°C at this temperature [39]. Continuous use of the AFIT stainless steel, small-scale sectional rig deformed the individual parts, allowing gaps to form in the assembly and air entrainment that could not being accounted for in calculations involving mass flows [22]. This is avoided by using Hastelloy-X, which has a lower thermal expansion coefficient. The downfall, however, is that the melting temperature of Hastelloy-X is approximately 1630 K [38], whereas stainless steel melts at 1800 K [39]. The rig, however, will never see material temperatures this high in normal test intervals.

3.3.3. Core Section and Rayleigh Loss MATLAB Code

The core section of the UCC test rig is made up of a 10.16 cm long center body, which passes through the center of the circumferential cavity as seen in Figure 31. Two center body sections were designed and built to study the ability of controlling Rayleigh loss within the core. As shown by Johnson [26], these could lead to serious integration issues with engine hardware, necessitating the need to mitigate Rayleigh loss. Each center body has an ID of 6.096 cm at the front and 5.08 cm at the rear. The six hybrid vanes were designed to meet the objective of turning the flow from 35° to 70° and have axial chord length of 8.89 cm and a maximum thickness of 3.18 cm. The first center body, shown in Figure 38, had a straight taper ID from the front to the rear and is referred to as the tapered center body (TCB). This would be used as the baseline to study Rayleigh loss, pressure and Mach number distribution.

The second center body, the low loss center body (LLCB) had a distinguished ID distribution used to slow the flow and theoretically reduce Rayleigh loss. This ID is expected to slow the flow, lessening the effects of the pressure loss due to heat release, and accelerate the

flow back to the same exit conditions of the baseline case. It was expected that the TCB would experience roughly 1-3% larger pressure drops due to Rayleigh loss over the LLCB design, based on the decrease in Mach number at the core/cavity interaction.

Figure 38. Baseline tapered center body

A MATLAB [40] code was written to aid in the design of the ID distribution of the LLCB, taking into account Rayleigh effects, heat addition, and turning to develop a passage cross-sectional area that reduced the Mach number (by expanding the area) in the core at specific points, while maintaining necessary inlet and exit conditions. This area was then implemented into the design of the ID of the LLCB with a fixed OD to achieve the desired area distribution. The code breaks the core into four sections with the general shape shown in Figure 39. Before Station 1, flow would be leaving the compressor rotor at roughly a 35° swirl angle at Mach 0.35. The flow is diffused to a desirable burning Mach number at a constant 35° swirl angle to the axial direction in Station 1. Station 2 is directly under the cavity and expands based on the heat release at the same 35° swirl angle. While the physical cavity was not represented in the code,

heat and mass addition at station 2 represented the movement of cavity flow into the core.

Through Station 3, the flow turns from 35° to 70° swirl and continues to expand based on heat

release in an attempt to burn as much of the fuel as possible. Finally, Station 4 contracts to

accelerate the flow to the Mach 0.8 required for the turbine rotor at a constant 70° swirl angle,

with the remaining combustion/heat release done before exiting the combustor. The hybrid vane

runs from the end of Station 1 to the start of Station 4. The vane geometry was taken into account

with the addition of a blockage percentage used to determine the effect the vanes had on the area

and Mach number distribution. This was incorporated into the final design of the center body

section.
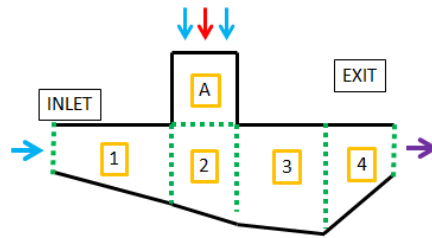
Figure 39. Station numbers for LLCB design MATLAB simulation

The circumferential cavity was not included in this study. The g-loading in the cavity can

be calculated by Equation 2 and at a g-load of 2000 in the 15.9 cm circumferential cavity of this

rig, the tangential velocity was 39 m/s. At 1500 K, this would equate to approximately Mach

0.05. This means significantly lower Rayleigh loss would occur in the cavity in comparison to

the core because of the dependence on Mach number.

Three main equations were used in the calculation of an area distribution that would

lower Mach number and Rayleigh loss. These consisted of the continuity equation, a form of the

energy equation accounting for the heat addition, and a calculation of the Rayleigh loss which

was calculated based on Equation 5. At each step in Stages 1 through 4, all flow conditions, including temperature, pressure, velocity, Mach number, and total conditions, were calculated. The equation of continuity [24] is given by

$$\rho_i M_i a_i A_i = \rho_f M_f a_f A_f$$

Equation 9

where ρ is the density, M is the Mach number, a is the local speed of sound, and A is the cross sectional area. Once the flow was combusting, due to increased pressure and temperature, it must continue to expand in order to maintain a constant Mach number. Continuity was used to both expand and contract the flow in the necessary locations to achieve the desired Mach number distribution. Total conditions were found from Mach number and static quantities using isentropic flow relations. The total pressure ratio between the initial and final conditions is calculated using Equation 4. The temperature increase due to heat release [24] was characterized by

$$T_f = T_i + \frac{qN}{\dot{m}C_p}$$

Equation 10

where T is the temperature in K, q is the energy per unit mass (J/kg), N is the fraction of heat given off at the current cross sectional area, and C_p is the specific heat with respect to pressure (J/kg K). C_p was calculated based on the fuel (propane) to air ratio at an average temperature over the whole combustor.

Once the proper area distribution was created for the heat/mass addition case (the hot or reacting case), the non-reacting (cold) case was run by using the same geometry and mass addition, but no heat release. This provided the difference between the reacting and non-reacting cases. Because aerodynamic losses were not taken into consideration, the total pressure loss in the non-reacting case was, as expected, zero.

In implementing the code, a series of steps consisting of an area change followed by a heat release process at constant area was utilized as indicated in Figure 40. The heat release was distributed in Stations 2, 3, and 4 at 50%, 40%, and 10%, respectively, and the mass addition from the cavity to the core was distributed in ten steps in Station 2 to simulate the mass leaving the cavity. The heat release distribution was chosen as the most realistic to what is expected in the test rig, and was seen when comparing the code run with inputs from Johnson's CFD analysis on a larger UCC model [26], but needed to be verified using experimental methods. Changing the heat release percentages in each of the stages would cause different Rayleigh losses to occur, with larger losses resulting from the burning near the exit, where the Mach number is much higher. Johnson's model was used as a validation for the heat release portion of the code, which then provided areas for the new test rig at the correct flow conditions. Station 2 is represented between x = 5 and 10 cm where the CFD indicated elevated temperatures because it included an average of the temperature within the circumferential cavity that is not included in the MATLAB code. As shown in Figure 41, within the core section, the temperature rise calculated in MATLAB fairly accurately matches that of the CFD.
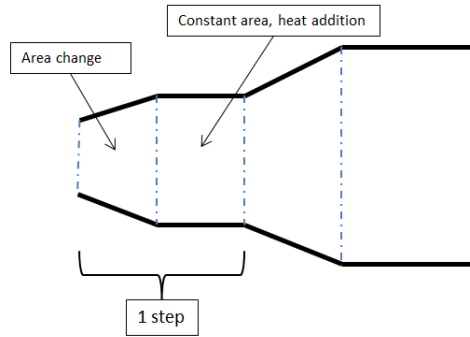
Figure 40. Stepping sequence to use continuity and constant area heat addition to design the area profile
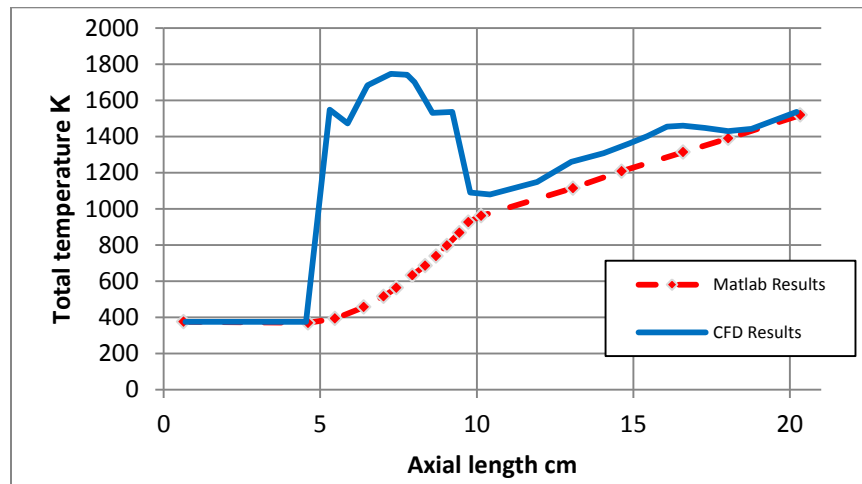
Figure 41. Comparison of CFD and MATLAB results for temperature rise in exaggerated UCC CFD model done by Johnson [26]

The resulting ID distributions for LLCB design are shown in Figure 42. The reduction of the ID in the LLCB design results in a nearly 20% area increase and acts to slow the flow, reducing Rayleigh loss in the core. Note that the exit area was not contracted back to give a Mach number of 0.8. This code provided a rough estimate of areas for the desired Mach numbers, but does not include several important factors such as aerodynamics, viscosity and boundary layer build-up, etc., which must be quantified with CFD or experimentally. Therefore a target

55

Mach number between 0.5-0.6 was used for the exit area, and once verified, can be modified later to reach Mach 0.8. This also leaves more exit area in the rear of the test rig for instrumentation and data collection.

These geometries were tested using CFD to ensure significant aerodynamic losses were not seen when expanding the flow. To do this, a structured, two-dimensional grid profile of the core section of the cavity was created in Point Wise. The computational code Fluent was used to analyze the flow in both the cavity and core sections to quantify the losses and investigate if any flow separations occur. A second-order, Roe scheme solver was used to solve the flow field within the grid, with a k-ω turbulence model for enhanced wall treatment. The cavity and core inlets were modeled as mass flow inlets while the exit of the rig was modeled as pressure outlet to ambient conditions, with mass flow per unit area matching that of the rig design. Results showed no significant flow separation using the modified ID distribution of the LLCB, shown in Figure 43; however there is a significant pressure gradient across the core span which must be studied experimentally.
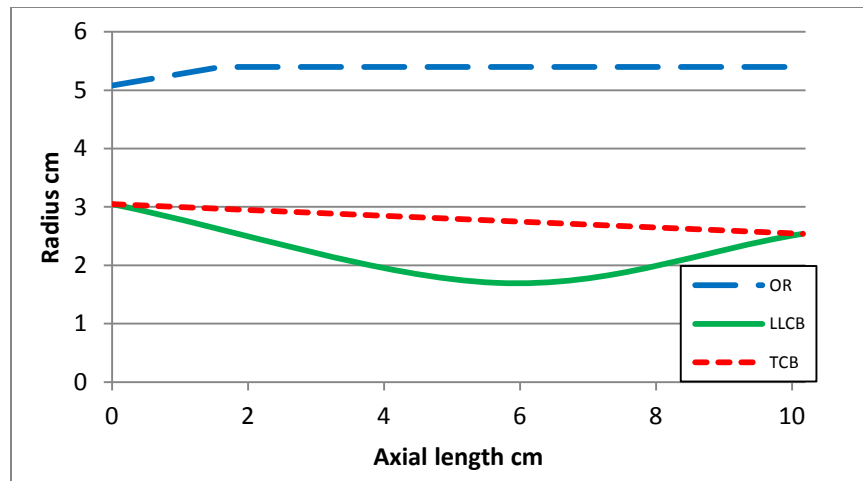
Figure 42. Radius distributions for LLCB and TCB designs
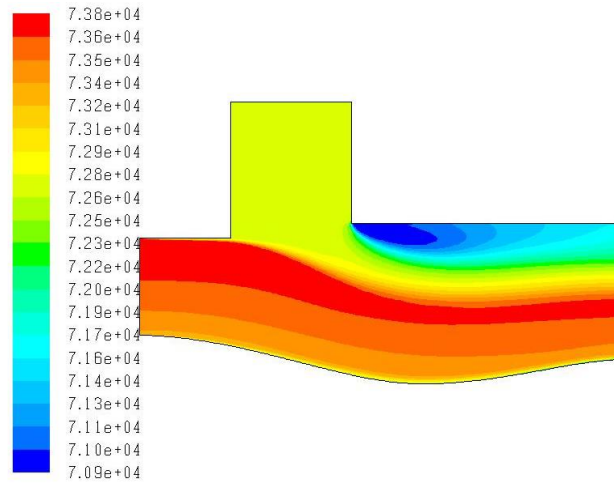
(a)
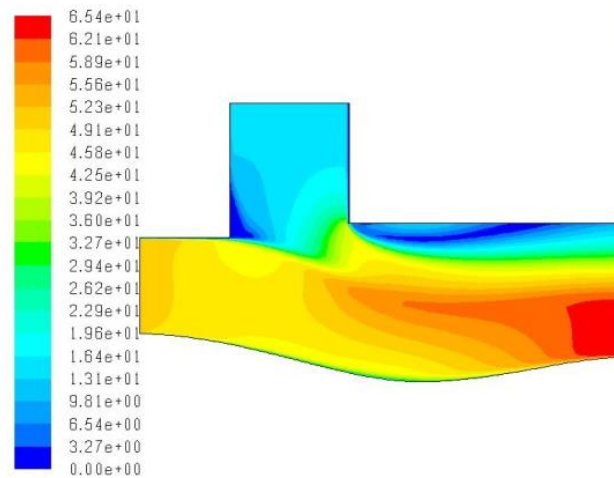
(b)

Figure 43. CFD calculation of (a) total pressure (Pa) and (b) velocity (m/s) in a 2D representation of the

LLCB

Due to the complexity of the vane structure in the center body section, special fabrication

equipment with true three-axis or above milling capability had to be used. Williams International

provided sponsorship to this effect and used their milling capabilities to manufacture the straight

section. The LLCB was manufactured by Kutrieb Research in Chetek, Wisconsin. Both center bodies were machined from stainless steel, as this is not expected to be a final design and stainless is much less expensive than the Hastelloy-X used for the more permanent pieces. Each center body was made from three pieces, which would allow for future cooling schemes and probe locations to be machined into the vanes. The complete assembly also had a hollow center to allow cooling air to travel through the system, as shown in Figure 44, which was brought in through the pre-swirl section. Being in three pieces, the center bodies could also be later modified for cooling schemes and pressure and temperature instrumentation on the vanes themselves.

Figure 44. LLCB (left) and TCB (right) fully assembled

3.3.4. Combustor Exit

The exit of the rig was made up of a 3.81 cm long quartz tube section that allowed optical access to center body section to study flow migration, and an instrumentation ring with 21 ports that were used for taking pressure and temperature measurements. These ports were located

approximately 0.635 cm from the exit of the vanes. The instrumentation ring held the quartz tube in place and was mounted via three spring-loaded bolts attached from the ring to the back cavity wall, as seen in Figure 45. A metal tube was built from steel to replace the quartz tube for high heat, high endurance testing, so that failure did not occur. The instrumentation ring was also fitted with bolt holes to allow the attachment of a nozzle for the use with the small turbine project [34, 35].

Attached to the center body was a 21 cm tail section with a 6.5° expansion angle that helped expand the flow out the exit. The flow at the exit plane is expected to be near Mach 0.6 with 70° swirl, as dictated by vane geometry. The tail and instrumentation exit ring, shown in Figure 45, were made from Hastelloy-X, as this would be an extremely hot section of the rig. The exit of the test section was configured roughly 25 cm from the exhauster, allowing sufficient space of measurements at the exit. The instrumentation ring was configured with total and static pressure and temperature probes to characterize the exit flow, which could be varied for each research objective. The full center body assembly, made up of the nose cone, pre-swirler, hybrid vane section, and tail, is shown in Figure 46.
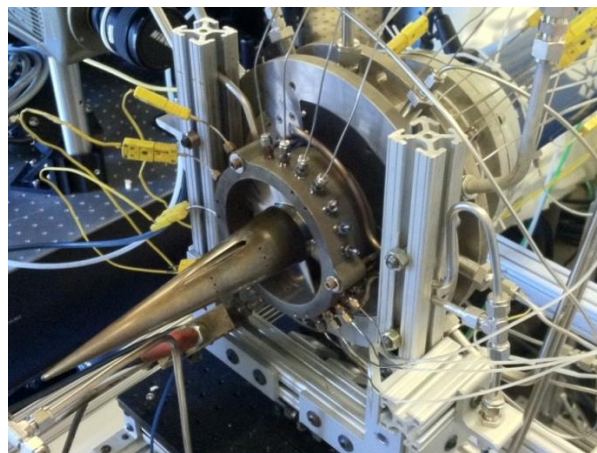
Figure 45. UCC tail and exit ring
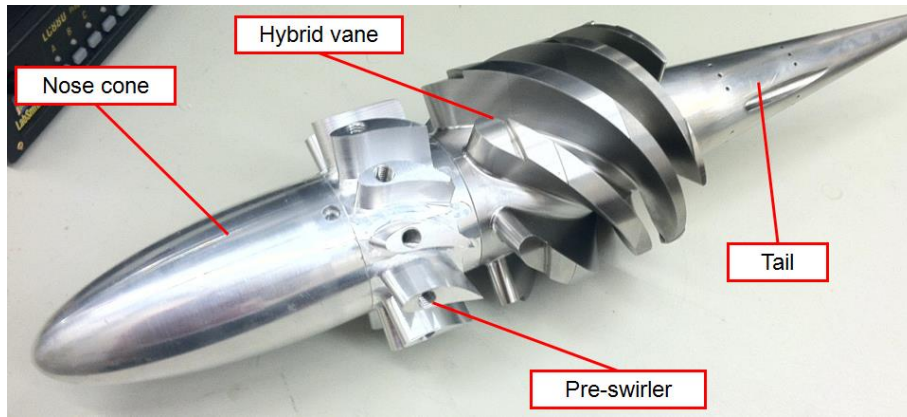
Figure 46. Full center section of the UCC

3.3.5. Rig Cooling

In order to extend the life of the rig and its components, a cooling scheme was designed

into the core section of the test rig. The purpose of the integrated cooling system was to use

convection to remove heat from the core section components by routing cooling fluid through the

hollowed centers of these components. The flow path for cooling fluid is shown in Figure 29.

The fluid enters the rig through the pre-swirl vanes and enters a center cavity within the pre-

swirler, which opens up into the hollowed out, main center body. The fluid flows through the

center body into the tail, where it exits via two sets of radial holes into the exit of the rig, 3.8 cm

downstream measurement ports on the instrumentation ring, to help cool the rig exit flow before

it enters the exhausters without interfering with data collection. A cooling ring, shown in Figure

47 provides additional cold air to the hot exhaust gas in the exhauster, to cool flow before it

reaches the exhaust fan and motor.
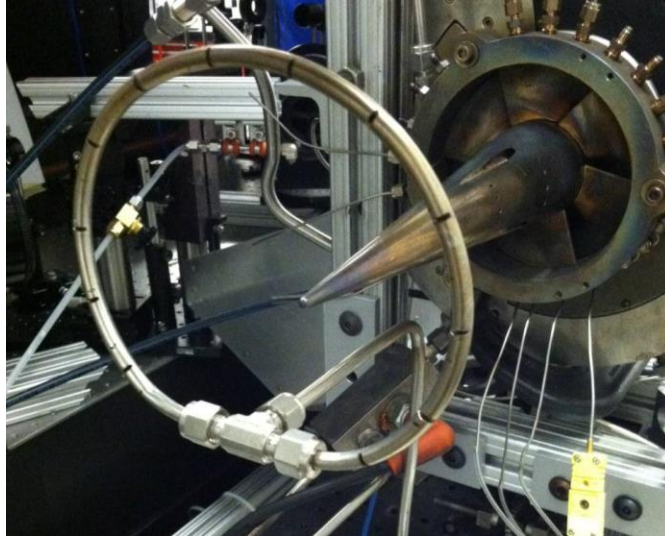
Figure 47. Exhaust cooling ring

During initial testing, significant heating occurred on the back plate of the cavity section near OAPs where material is thin, shown in Figure 49. 2D CFD simulations also verified this was a region of high turbulence, shown in Figure 48. Visual thermal gradients were also visible at the ports where the quartz windows were installed and heating caused catastrophic failure of the quartz during burn testing in excess of three minutes. To combat the buildup of heat on this back section, three arrays of air impingement jets were constructed around the rear of the quartz exit tube of the rig, seen in Figure 50, which had six, approximately 0.05 cm^2 air jets spaced 1.75 cm apart from one another. These were spaced 1.75 cm from the back plate and impinged on lower OAP structures.
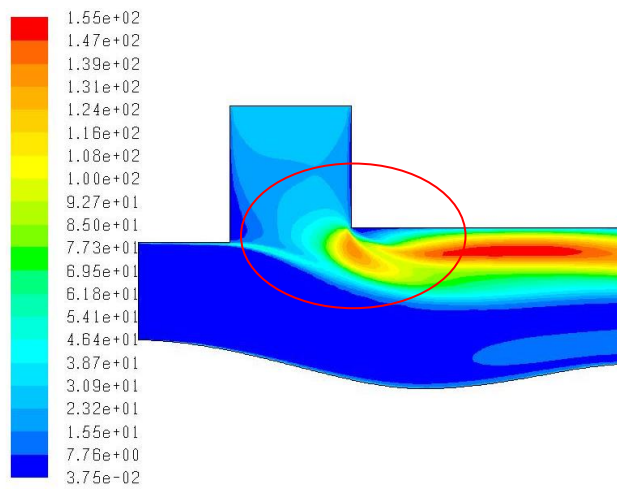
Figure 48. 2D turbulence intensity on rear cavity wall and OD of the exit

(a)
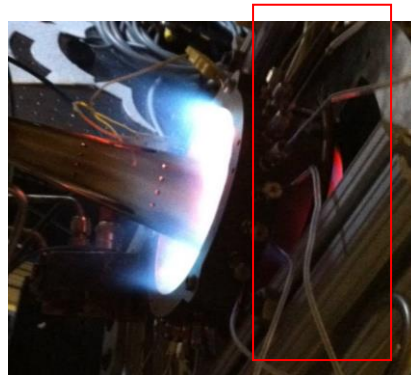
(b)

Figure 49. Visible heating on back side of inner cavity (a) and on exit tube (b)
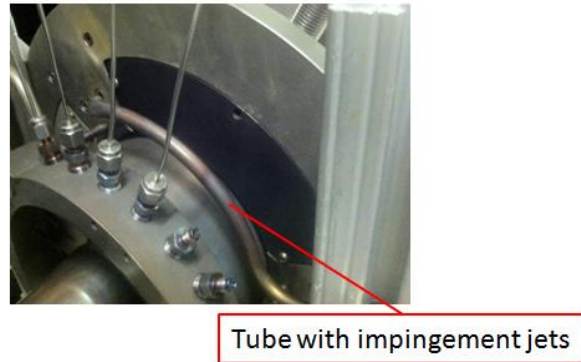
Figure 50. Impingement cooling air array (1 of 3)

3.3.6. Rig Test Stand

A new test stand was built and designed to support the UCC test rig. 5.08 by 5.08 cm 80/20® modular frame was used to construct the stand, which was mounted onto a 2.54 cm thick steel breadboard. A secondary breadboard with was mounted to the top, to which a vertical translation stage is bolted and holds the rig frame, made from 2.54 by 2.54 cm 80/20®, as shown in Figure 51.The rig itself is bolted to two upright pieces of frame via four bolts, two per side. The translation stage allows the height of the rig to be changed to characterize different cavity sections without refocusing cameras and other diagnostic equipment. This top section can be removed and swapped with a dual rail thrust stand with four air bearings mounted to a large breadboard with an attached load cell to measure thrust of small turbine engines with and without the use of a UCC style afterburner section, as done by Conrad et al. [34] and Conrad [35].
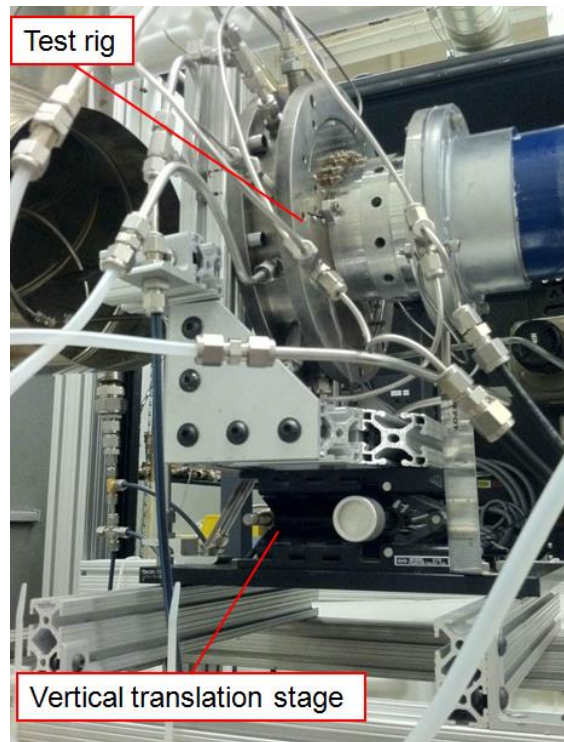
(a)
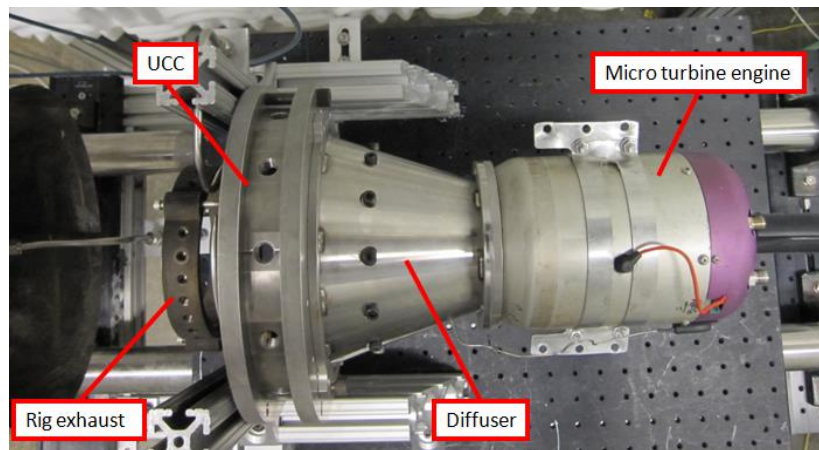
(b)

Figure 51. Rig with (a) vertical translation stage and (b) thrust stand with micro turbine [35]

3.4.   Combustion Optimization and Analysis Laser (COAL) Laboratory

In order to facilitate the new test rig, the COAL Lab needed several additional changes and upgrades, including the before mentioned air supply upgrades. Because of the lengthy fabrication time of the rig and the increasingly unorganized configuration of the network of lab systems, it was decided that during the interim, the lab should essentially be gutted and reorganized to both clean up the existing power, signal, and plumbing lines and lay new lines as efficiently and logically as possible to create a simpler yet more capable lab that can support the new UCC. All lab layouts, plumbing, and wiring diagrams can be found in Appendix C.

3.4.1. Gas Control Flow Modifications, Organization, and Upgrades

The gas control system was updated from two, 4-channel, analog MKS type 247 controllers to a single, 8-channel, digital MKS type 647C controller. This system allowed the user to update MFC ranges and gas constants, while providing real-time data. It also allowed control from the unit itself or through a computer using a RS-232 cable and LabVIEW [18]. The MKS 647 controller was connected to eight MKS MFCs in the fuel control box next to the rig stand, seen in Figure 52, which ranged from 20 to 200 SLM N2 with the required gasses such as air to run the rig in Table 3. Gases were kept in the tank farm, shown in Figure 34. Most gasses used were stored in K-bottles with a fixed pressure regulator at 25 PSI, except the propane system outlined previously. Shop air was provided via 230 liter air tank at 80 PSI. To account for density through the controller, gas correction factors (GCF) were used to ensure proper mass flow was being used. Each MFC had a 0.1 micron filter and electric solenoid upstream of it. The solenoids were controlled digitally via LabVIEW through a National Instruments PCI-6905 and an OCTO 22 relay system. The electro-pneumatic liquid fuel solenoid was also controlled

through this system, although the liquid fuel pumps had their own flow metering and control

system that linked directly to the control computer via serial port. A full flow control layout can

be found in Appendix C.

Table 3. MFC ranges and gas for MKS system

MKS Channel	MFC Model	MFC Range (SLM) Using N_2	Gas	GCF	Line Pressure (PSI)
1	MKS Alta 1480A	50	SHOP AIR	1.00	80
2	MKS Alta 1480A	30	N_2	1.00	25
3	MKS Alta 1480A	30	CEM AIR	1.00	25
4	MKS Alta 1480A	50	H_2/He	1.01/1.45	25
5	MKS Alta 1480A	30	C_2H_4	0.89	25
6	MKS Alta 1480A	20	CO_2	0.70	25
7	MKS type 1559	200	C_3H_8	0.36	80
8	MKS type 1559	200	C_3H_8	0.36	80
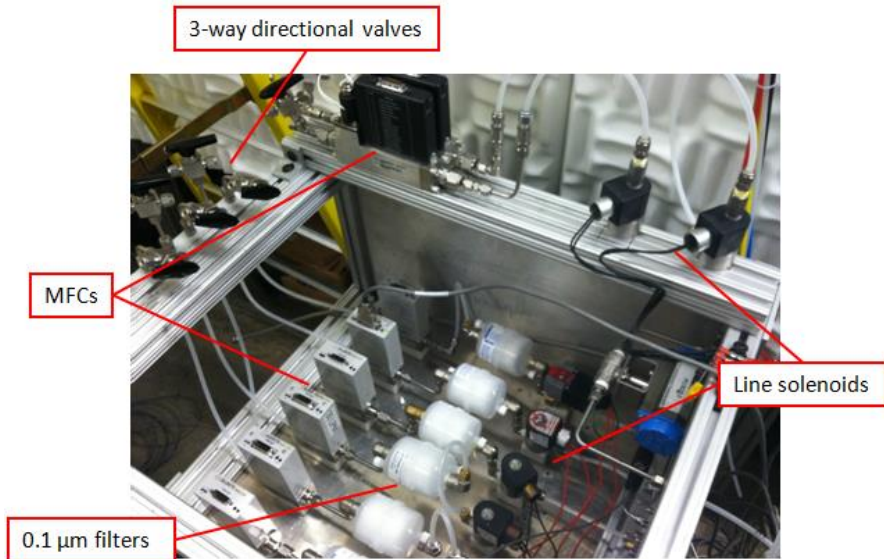
Figure 52. Combustion gas flow metering and control box

MFCs 1 and 4 were calibrated a Mesa Labs Bios DryCal Definer 220, shown in Figure

53, which is able to measure flow from 0.5 to 30 SLM with an accuracy of ±1.5%. MFCs 7 and 8

were calibrated using a Mesa Labs Bios DryCal Definer 1020, shown in Figure 53, which could

measure 5-500 SLM of flow with ±0.25% accuracy of reading. MFCs 2, 3, 5, and 6 were

calibrated using the 220 for low ranges and the 1020 for the higher ranges of each MFC. Each

MFC was calibrated using shop air at 80 PSI over the entire range of the MFC, and later

corrected for the gas being run through the controller using GCF, shown in Table 3. Calibration

data for each MFC is given in Appendix D. MFCs 2 and 3 were audibly louder than the rest at

higher flow rates (70% of max), and MFCs 2, 3, and 7 showed increased instability at flow rates

near 85% max range. Therefore, these were either used only as support lines for cooling (in the

case of MFCs 2 and 3), or at the lower, more stable flow rate (MFC 7).

(a)

(b)

Figure 53. Mesa Labs (a) Definer 220 and (b) Definer 1020 flow meters

3.4.2. Pressure and temperature measurements

The previous setup involved single pressure transducers for each pressure measurement. This was expensive, timely to setup and calibrated, and with only a dozen pressure transducers available, only a few measurements could be made at one time. These individual pressure transducers were replaced with a single Esterline DTC Initium acquisition system and one, 64-port ESP-HD PSID pressure scanner, seen in Figure 54. With automatic calibration using shop air supply at 80 PSI and Ethernet interface, this system allows for increased characterization of the test rig, with easy setup and use. A stand-alone pressure transducer was kept in the system to measure ambient conditions in the lab.

(a)
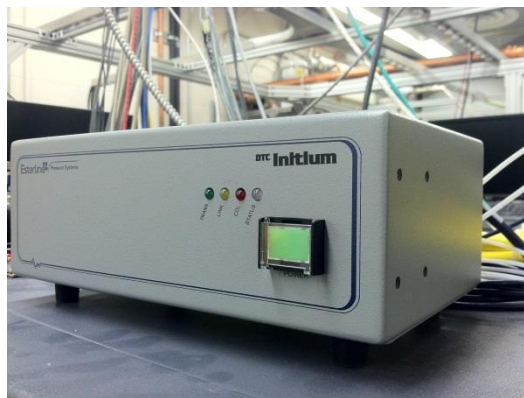
(b)

Figure 54. (a) ESP-64HD pressure scanner and (b) Initium acquisition system

The temperature measurements were done with K-type probe thermocouples. A 48-connection board was installed near the rig for easy access for adding new thermocouples. Four, 12-line cables ran from the board back to the control cabinet to a 4-slot National Instrument (NI) data acquisition module (DAQ) for increased organization, shown in Figure 55. Note, at the time of this experiment, only two, 16-channel and one, 4-channel compact DAQ modules were available. The system capability can easily be increased to its full potential with the purchase of an additional compact DAQ module with 16 channels.
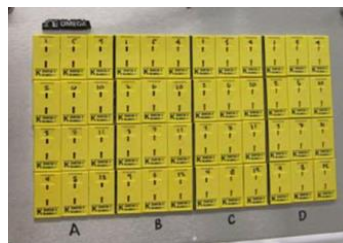
(a)

(b)

Figure 55. Thermocouple (a) plug panel board and (b) DAQ setup

3.4.3. National Instruments Hardware and LabVIEW Code Updates

The initial setup done by Anderson [17] included software and hardware from 2006. Since then, NI technology, the main data acquisition systems that were used, had changed and the COAL Lab had become outdated. To update the lab, changes to both hardware and software were necessary.

The three existing NI SCXI-DAQ systems were replaced with four Compact DAQs: two, 4-port and two, 8-port compact DAQs, which used individual, plug-in DAQ modules (analog/digital inputs/outputs, thermocouple connections, etc.,) that drastically changed the modularity and capability of the control system. In addition, a new DELL control computer was purchased. A NI, PCI-6509 control board was installed in the control computer to operate any required digital signal outputs, such as solenoid control. The complete setup of the control system can be found in Appendix C.

The original 2008 version, LabVIEW [18] code constructed by Anderson [17] was extremely complex and required an advanced LabVIEW operator to make major changes. Therefore, the 2012 version of LabVIEW was installed to keep the system current and new code was constructed to operate the necessary requirements for the UCC test rig, including air and gas control, temperature, pressure, and emission measurements, and liquid fuel and Jet Cat control. The code layout and functionality was simple in comparison to the previous code and allowed basic users to change different characteristics with only a beginner's understanding of LabVIEW.

The entire control cabinet was rebuilt to enhance capability at the station, shown in Figure 56. A designated multi-camera monitoring system was also installed for rig monitoring

and safety purposes, allowing the user to view the rig from a safe distance. Two computers, one designated for HSV data, and the other for the LabVIEW [18] code/control of the lab, were installed with rack-mounted monitors. The MKS and PID systems were also rack-mounted for easy access.
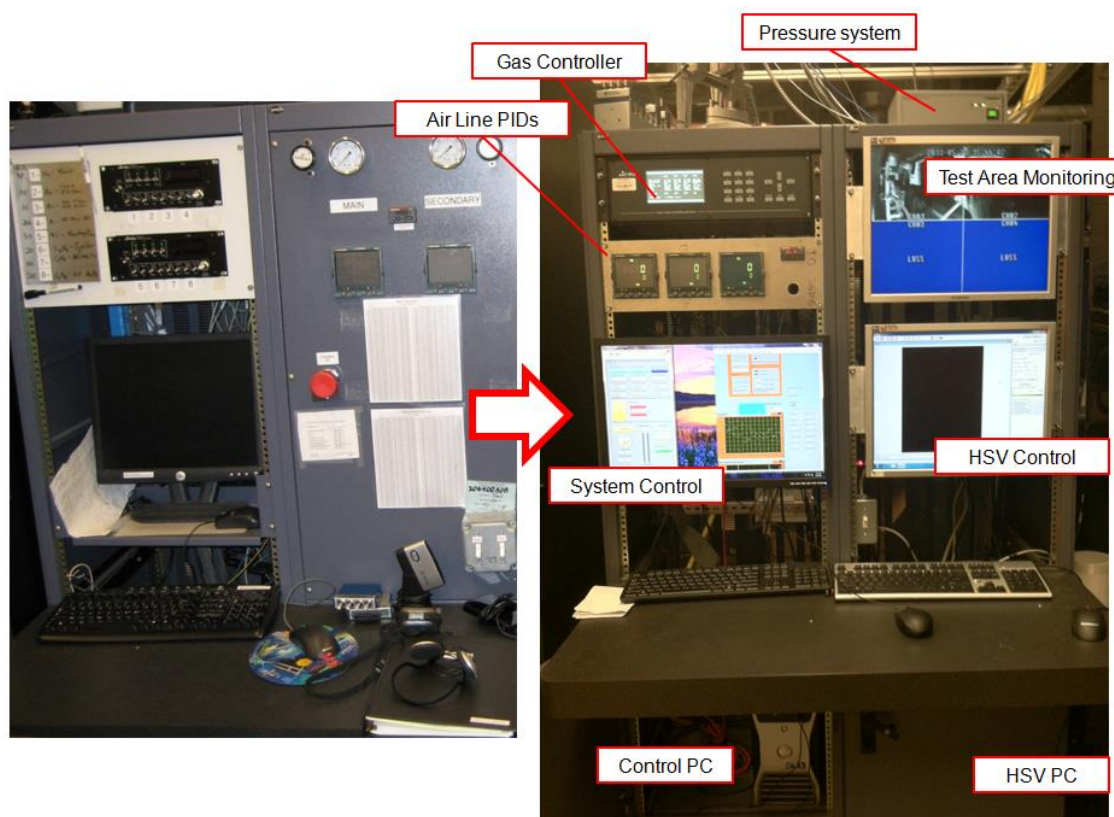
Figure 56. Before (left) and after (right) of the control cabinet

3.5. Characterization Techniques

In order to characterize the new test rig, certain qualitative and quantitative techniques were used in conjunction with one another. The techniques provided information on where reactions were taking place, how changing characteristics impacted loading and efficiency,

pressure losses, and other key information to better understand the physical environment within the UCC.

3.5.1. High Speed Video Setup and Data Processing

High speed imaging of the flow field can provide information on the flame structure, flow velocity, and other characteristics within the circumferential cavity and UCC exit. To accomplish this, a Visions Research Phantom V12.1 color camera, capable of capturing up to one million frames per second, was used to image the flow field.

The camera was originally setup to view one of the OAP sections with a quartz window, shown in Figure 57. However, because the size of the core inlet tube and connecting flange, the camera could not be aligned perpendicular to the window. Therefore it was placed on the optics table next to the test rig and a mirror system was used to achieve a more direct view into the cavity, shown in Figure 58.
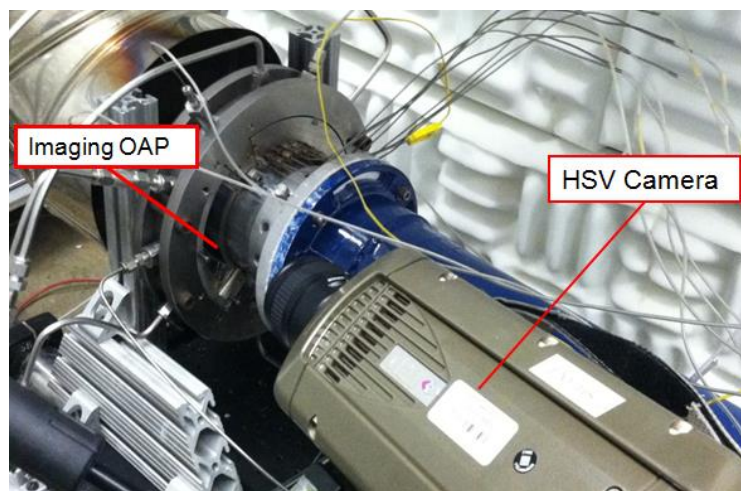
Figure 57. Original camera setup impeded by the core inlet
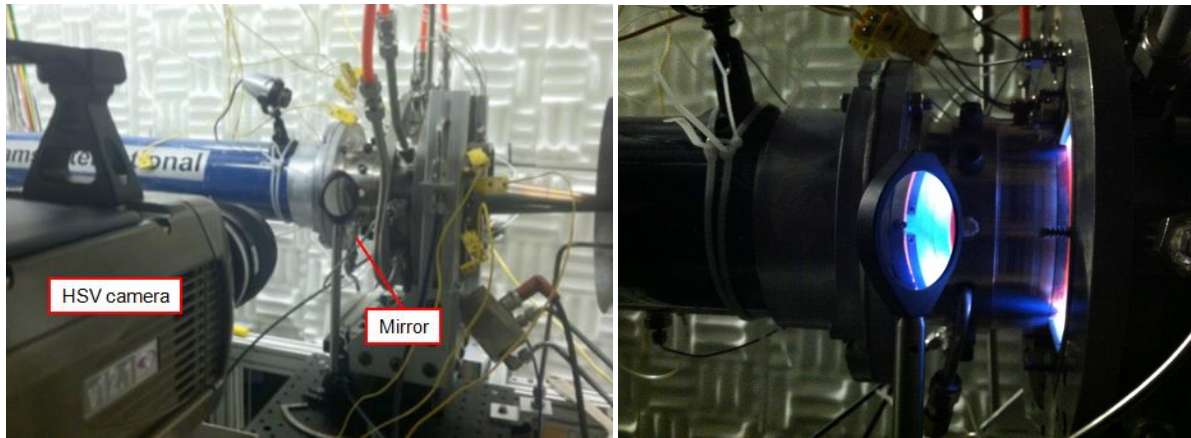
Figure 58. Camera setup with mirror system to allow direct line of sight into the cavity

The Phantom V12.1 camera was connected to a Lenovo Think Station computer and was run using Vision Research PCC software version 2.14.727.1. A Nikon 85 mm lens was used to focus the image on the mirror, which reflected the image back to the camera. The camera resolution was set to 608x800 pixels, with a sample rate and exposure time of 8000 fps and 124 μs, respectively. These settings were chosen to minimize the amount of time between frames, but still leave enough exposure time to capture the flame.

In addition to a physical calibration image, a current session reference (CSR) was done to remove noise and bias due to thermal gradients in the camera once it had reached its operating temperature. The CSR was done with a lens cover on the camera to produce a completely unsaturated image. Pixels still detecting signal were then corrected for using the CSR before testing was done, resulting in an accurate collection of images/video of the flame intensity.

3.5.2. Determining G-loading

The cavity and core air supplies were set up on the 3.81cm and 7.62 cm air lines, respectively, giving independent control over each. The cavity air supply was increased or

73

decreased in order to change the g-loading, which was determined from two different methods and checked against each other for verification of accuracy. The first of which used two total pressures (one in-line with the fuel injector and the other in-line with the rear air driver jet just upstream of a fuel injection location) and static pressure probes inside the cavity, shown in Figure 59, to determine the Mach number, M, within the cavity using the equation [24]

$$M = \sqrt{\left(\left(\frac{P_T}{P}\right)^{\gamma-1/\gamma} - 1\right)\frac{2}{\gamma - 1}}$$

Equation 11

where P_T is the total pressure, P is the static pressure, γ is the ratio of specific heats, which for reacting flows, the $\gamma = 1.37$ was used, whereas $\gamma = 1.4$ was used for non-reacting flows. Tangential velocity is then calculated using the equation [24]

$$V = M\sqrt{\gamma R T}$$

Equation 12

where R is the gas constant and T is the cavity temperature, found by using a K-type, Omega brand stick thermocouple. The air value of $R=287$ J/kg/K was used for calculations. The g-loading in the cavity is then found by using Equation 2.
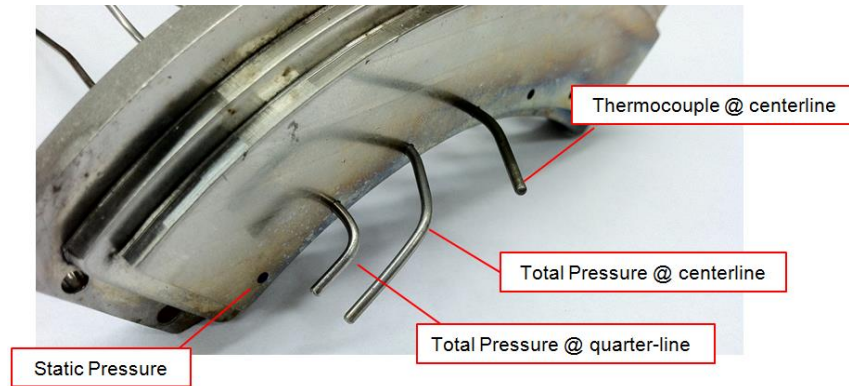
Figure 59. Total and static pressure and temperature probes in the circumferential cavity instrumentation plate

The second way tangential velocity was found was using high speed video images and Innovative Scientific Solutions Inc.'s (ISSI) digital PIV software version 2.1 [41] to track flame structures as they moved from one frame to the next. Single, frame-to-frame pairs of image can be compared to one another, or a batch process can be done on an even number of images in order to find average velocity vector. Images must be 8-bit, monochrome, TIF images in order for the program to work correctly, which was done using the software ImageJ [42] since the camera images were color. The software must also be installed on the main hard drive of the computer system in its own folder, not in "Program Files" or another subdirectory. File names must not contain any special characters or spaces.

Additional analysis of the flow field could be done simply analyzing the video playback of the images and studying the way the flow moved, which could reveal structure patterns and helical motion in the cavity and core sections. Visible flame lengths also gave insight as to reaction zones and times and the completion of reaction at the exit of the system.

3.5.3. Cavity/System Equivalence Ratio

To change the equivalence ratio, the cavity air mass flow was kept constant and the fuel flow was increased or decreased depending on the desired condition. Equivalence ratio, ϕ, is defined by the equation [5]

$$\phi = \frac{\left(\dot{m}_{air}\middle/\dot{m}_{fuel}\right)_S}{\dot{m}_{air}\middle/\dot{m}_{fuel}}$$

Equation 13

where $\dot{m}$ is the mass flow and S refers to the stoichiometric condition. The stoichiometric air-to-fuel ratio for propane is approximately 15.7 [5]. An air-to-fuel ratio less than 15.7 is then considered fuel lean, while an air-to-fuel ratio greater is fuel rich.

3.5.4. Calculating Rayleigh Loss

To determine the Rayleigh loss in the system, the flow was run hot and cold for each test condition, and the pressure and temperature characteristics were collected at the two locations. While the cold case gave insight into aerodynamic losses, the hot case gave total losses, which were made up of both aerodynamic and Rayleigh losses. The Rayleigh loss is then given by the equation [25]

$$\left.\frac{P_{T,3} - P_{T,4}}{P_{T,3}}\right|_{Rayleigh} = \left.\frac{P_{T,3} - P_{T,4}}{P_{T,3}}\right|_{HOT} - \left.\frac{P_{T,3} - P_{T,4}}{P_{T,3}}\right|_{COLD}$$

Equation 14

where P_T is the total pressure, *3* refers upstream measurement location, and *4* refers to the downstream measurement location (before and after heat addition, respectively). Mach number and velocity are then calculated using Equation 11 and Equation 12, respectively.

3.5.5. Uncertainty Analysis

An uncertainty analysis was done to determine the accuracy of the measurements and flow rates during testing. The general form, Constant Odds equation [43]

$$\delta R = \{\left(\frac{\partial R}{\partial x_1}\delta x_1\right)^2 + \left(\frac{\partial R}{\partial x_2}\delta x_2\right)^2 + \ldots + \left(\frac{\partial R}{\partial x_N}\delta x_N\right)^2\}^{0.5}$$

Equation 15

was used, where R is the function/equation, x_N is the measured variable, and δx_N represents the accuracy of the measurement. To calculate g-loading, there are three main measured components: total pressure, static pressure, and temperature. The accuracy in which these are collected depends on the instruments used, and these accuracies are summarized in Table 4, along with a single test point data. This data was taken from the centerline cavity total pressure probe, cavity static pressure and temperature measurements. A measurement of cavity radius was also done using a ruler, which had an accuracy of ±0.1 cm. The quantities are used to determine cavity Mach number, velocity, and finally g-loading, using Equation 11, Equation 12, and Equation 2, respectively.

Table 4. Accuracy of measurements for total and static pressure and temperature

Quantity	Determined via	Accuracy	Result
Total pressure	ESP-64HD pressure scanner	±0.03 %	100732 Pa
Static pressure	ESP-64HD pressure scanner	±0.03 %	100684 Pa
Temperature	K-type thermocouple	±2.2°	1189 K
Cavity radius of probe	Standard ruler	±0.1 cm	6.7 cm

This error is compounded through these calculations as seen in the following equations, where the previous dependent variable becomes an independent variable with its own error within the equation (G signifies g-load);

$$\delta M = \left\{\left(\frac{\partial M}{\partial P_T}\delta P_T\right)^2 + \left(\frac{\partial M}{\partial P}\delta P\right)^2\right\}^{0.5}$$

Equation 16

$$\delta V = \left\{\left(\frac{\partial V}{\partial M}\delta M\right)^2 + \left(\frac{\partial V}{\partial T}\delta T\right)^2\right\}^{0.5}$$

Equation 17

$$\delta G = \left\{\left(\frac{\partial G}{\partial V}\delta V\right)^2 + \left(\frac{\partial G}{\partial r}\delta r\right)^2\right\}^{0.5}$$

Equation 18

The results for the measured quantities and the errors involved are shown Table 5. As seen, there is extremely low error in the Mach number calculation, but error grows with the calculation of velocity, and gets to be notable when calculating g-load, since the velocity error is squared in the g-load calculation. However, this error is still within 1.5% of the resulting g-load for the given test data. Equation 15 was also applied for Mach number reading for Rayleigh loss and pressure drop tests, using the same pressure and temperature system.

Table 5. Error propagation results for Mach number and g-load measurements in the rig

Quantity	Measured	Error result	Accuracy to measured value
Mach #	0.026	δM=2.18e-007	8.26e-004 %
Velocity	18.0	δV=0.17	0.09 %
g-load	493	δG=7.38	1.50 %

While measurement techniques are very accurate due to the high accuracy the equipment offers, the flow itself is very unsteady in the cavity and significant fluctuations can occur due to the accuracy of the flow equipment. Three main systems drive this error: the mass flow controllers for the fuel flow, the air flow controller, and the airflow readout. The fuel mass flow controllers were calibrated using the Bios Definer 1020, which had an accuracy of 0.25% the full scale (FS) value (500 SLPM) but because of the high airflows, the air system had to rely on the accuracy of the Fox Thermal Systems FT2 flow meters on each line, which was 1% of FS (which is 18 kg/min for the cavity air line). The same analysis was then done Equation 15 for the error in reported cavity equivalence ratio. The two variables are used to find the partial derivative of Equation 13 and the Constant Odds method is again used with the result is shown in Table 6.

Table 6. Error propagation results for equivalence ratio

Quantity	Set point	Error result	Accuracy to set point value
Equivalence Ratio	1.76	$\delta\phi = 0.294$	16.67 %

This fluctuation in flow can cause errors in measurements since the correct measurement condition is not being met. Therefore, data averaging was used to find averages for Mach numbers, and therefore for velocity and g-loading as well. An averaging scheme in LabVIEW [18] was used to average pressure and temperature data over 45-60 seconds for each test case, with data rates for pressure and temperature roughly 330 and 100 Hz, respectively. Typical variation in pressure could be as much as 100 Pa, but temperatures tended to be much steadier, only varying few degrees. Using the average values allowed for a more accurate result for the desired flow condition to be captured. The rig was also allowed to reach a steady state temperature, which took anywhere from 60-180 seconds depending on the test case. For some

79

cases, particularly those with high equivalence ratios or a swirl direction in the counter-clockwise direction, severe heating occurred on the rig body, and averaging and warm up time were decreased for rig preservation.

Test samples at the same operating conditions for a 3.24/1.08 kg/min core-to-cavity air split at an equivalence ratio of 1.76 were done over multiple test days to analyze the repeatability for a single g-load case. Table 7 shows the dates and results of each test case. Measurements are within 14% of each other at the worst case scenario. However, it was seen that g-load can vary at the same test point for the same test day all the way up to ±50. This is attributed to the unsteadiness in the fluid and the general wearing effect on probes, which must be replaced frequently as heating can cause the probes to deform out of their original position. As reported for stability results, varying ambient conditions in the lab may have a significant effect on the rig for characteristics for the same operating conditions as well, since it is an atmospheric rig. Temperature and pressure rise or fall may contribute to this error; however, trends would be expected to stay the same.

Table 7. Repeatability study

Date	g-load
18 JUN 2013	547
27 JUN 2013	493
28 JUN 2013	472

3.6. Testing

The research objectives previously outlined were addressed after the test rig was built and installed and the lab was properly configured. The following section outlines how each objective was met in detail. These objectives included the analysis of stability, g-loading, air injection diameter change, swirl direction, and Rayleigh loss. These tests will provide an initial

characterization to some of the most important parts of the UCC and act as a gateway for more in-depth research into each field.

Lower air flow rates than the design point of 0.45 kg/s (split 70/30 core-to-cavity) were used in these test cases due to a limit on fuel delivery to the rig. The maximum fuel deliverable is 0.25 kg/min using the current setup. At these rates, cavity equivalence ratios would be able to reach a maximum equivalence just shy of 0.5 in the cavity (for the design point). In order to reach equivalence ratios of 2.0 in the cavity, a fuel mass flow of 1.0 kg/min would be needed.

3.6.1. Swirl Direction Impact on Cavity Flow

Debate over the swirl direction of the cavity flow with respect to the hybrid vane developed by Bohan and Polanka [4] necessitated an experiment in which exit pressure loss and cavity flow characteristics were characterized for CW and CCW swirl directions. Anderson et al. [12] studied swirl direction with respect to an axial vane using emissions, but the number of fuel injectors in that particular test rig did not equal the number of vanes. Therefore it was likely that each vane passage (four passages all together) could have a different flow results because of their position with respect to the six fuel injectors. Using the AFIT UCC test rig would give accurate results as is a balance between fuel injection locations and vane passages. Results could determine the optimum swirl direction to either maximize efficiency or reduce the pressure loss of the system, or perhaps both, for this type of vane geometry.

The baseline cavity ring (0.45 cm air hole diameter) was flipped to change swirl direction from CW to CCW with respect to the vane, shown in Figure 4. Tests were performed at the two flow conditions, shown in Table 8, with the same core-to-cavity ratio of 75/25 and equivalence ratio of 1.76. Total pressure was collected for each case using four, 0.16 cm stagnation probes

81

aligned with the exit flow angle of 70° at the mid-span of the vane passages and averaged, shown in Figure 60. Static pressure and temperature were also collected using four probes each at the exit of a vane passage. The flow was also imaged using the HSV system inside the cavity using the mirror seen in Figure 58.

Table 8. Swirl test matrix for flow splits of 75/25 and equivalence ratios of 1.76

Core Flow kg/min	Cavity Flow kg/min	Swirl Direction
3.24	1.08	CW
3.24	1.08	CCW
4.86	1.62	CW
4.86	1.62	CCW
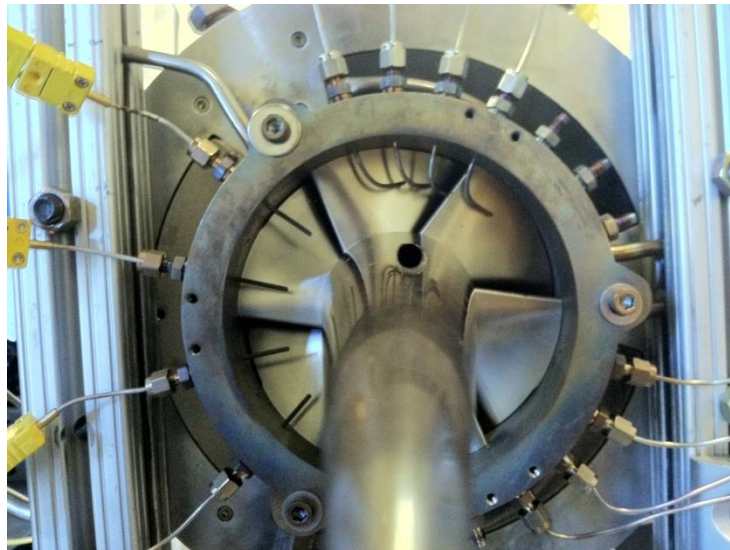
Figure 60. Total pressure, static pressure, temperature, at the rear of the UCC rig

3.6.2. Stability and Blowout Tests

Operability limits for the new test rig needed to be established so that future test cases could be done in a stable combustion environment. G-loading and equivalence ratio were varied at a constant core flow to determine the stable operating range over these two parameters. The point at which the fuel fails to ignite and cause a flame without the use of an igniter is considered

the blowout point and defined the stability region. While it is expected that the operability limits for these parameters will be similar to those seen by Zelina et al. [11] using the smaller AFRL rig, it is likely that rigs with different geometries will have different sets of limits. Factors such as cavity size, fuel, radius, and blowing ratio may all affect the ability to maintain a flame in the circumferential cavity, and these factors must be understood to establish the design space for proper engine integration.

The 0.45 cm air injector diameter was used with propane, and was tested without distribution baffles inserted. Initially, fuel baffles were used to break up the fuel stream at each fuel injection port. However, it was seen that significant amounts of fuel pushed around the outside of the cavity and caused significant wall/window heating (depending on the location of the fuel port). For this reason the following tests were all done without fuel baffles installed. The ring was installed for a CW flow field, and cavity mass flow was varied from 0.72 to 2.16 in the cavity at a constant core flow rate of 3.24 kg/min, changing the core-to-cavity split from 82/18 to 60/40. An equivalence ratio between 1.1 and 1.75 was chosen to serve as the start point, as these conditions were generally known to be stable within the cavity during initial testing, and the fuel flow was reduced until blowout occurred. The starting point equivalence ratio for each mass flow split is shown in Table 9. G-load was collected using total and static pressure and temperature probes in the circumferential cavity.

Table 9. Lean blowout test matrix for constant core flow of 3.24 kg/min

Cavity Flow kg/min	Core-to-Cavity Air Split %	Starting Point Equivalence Ratio	Fuel Flow kg/min
0.72	82/18	1.75	0.026
1.08	75/25	1.75	0.040
1.44	69/31	1.75	0.053
1.8	64/36	1.50	0.077
2.16	60/40	1.10	0.126

3.6.3. Rayleigh Loss Study

Johnson [26] showed that Rayleigh loss is an important part of the UCC and need to be studied and mitigated to ensure significant losses are not present. Therefore a determination of Rayleigh loss for the baseline configuration was done to study exactly what percentage of pressure drop was due to Rayleigh loss. The TCB and cavity ring with CW air jet injection diameter of 0.65 cm were used as the baseline case to study Rayleigh loss in the UCC rig. Tests were performed in a stable condition, under various g-loading, equivalence ratios, and air flow split configurations, shown in Table 10. These tests were performed for both reacting, and non-reacting flows. The same conditions were then run for the LLCB. Total and static pressure and temperature were collected at one point in the inlet tube and at four points at the exit of the rig at the mid-span location, which were used to find the average total pressure over one vane passage. In addition to the measured locations, the characteristics directly upstream of the vane were calculated based on area, mass flow, and measurements taken at the inlet location, using Equation 9. These were used to help better characterize the Mach number in the rig for given mass flows. Note that the density calculated using the pressure and temperature measurements at the inlet was used for this calculation because Mach number is less than 0.3.
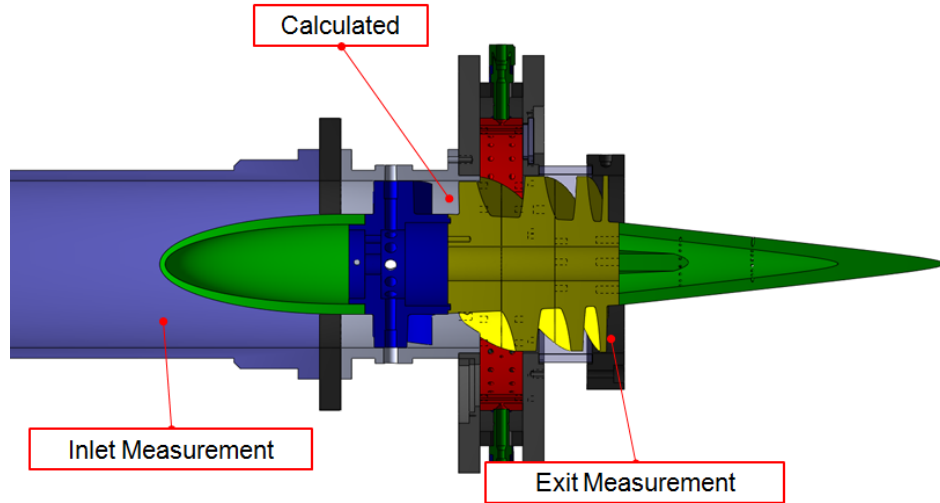
Figure 61. Total and static pressure and temperature probe locations for Rayleigh loss study

Table 10. Rayleigh loss study test matrix

Center body	Reacting/Non-reacting	Core Flow kg/min	Cavity Flow kg/min	Core-to-Cavity %	Equivalence Ratio
TCB	Reacting	6.02	1.08	85/15	1.75
TCB	Reacting	4.86	1.62	81/19	1.47
TCB	Reacting	4.86	1.62	81/19	1.76
TCB	Reacting	4.86	1.62	81/19	2.02
TCB	Reacting	7.92	1.8	81/19	1.82
LLCB	Reacting	6.02	1.08	85/15	1.75
LLCB	Reacting	4.86	1.62	81/19	1.47
LLCB	Reacting	4.86	1.62	81/19	1.76
LLCB	Reacting	4.86	1.62	81/19	2.02
LLCB	Reacting	7.92	1.8	81/19	1.82
TCB	Non-reacting	6.02	1.08	85/15	1.75
TCB	Non-reacting	4.86	1.62	81/19	1.47
TCB	Non-reacting	4.86	1.62	81/19	1.76
TCB	Non-reacting	4.86	1.62	81/19	2.02
TCB	Non-reacting	7.92	1.8	81/19	1.82
LLCB	Non-reacting	6.02	1.08	85/15	1.75
LLCB	Non-reacting	4.86	1.62	81/19	1.47
LLCB	Non-reacting	4.86	1.62	81/19	1.76
LLCB	Non-reacting	4.86	1.62	81/19	2.02
LLCB	Non-reacting	7.92	1.8	81/19	1.82

3.6.4. Cavity Air Jet Diameter Influence on g-Loading

Work done by Bohan and Polanka [4] showed the g-loading could be directly correlated to the hole size of the air injection jets using CFD, previously shown in Figure 15. This would allow a target g-load to be achieved for any given mass flow, ensuring stable combustion in the cavity for any application. This is an important study in determining if the stability region and g-loading is in fact impacted by the cavity jet diameter.

Three separate cavity rings with different air injection sizes were built, shown Figure 62. The baseline ring has an air jet diameter of 0.45 cm. The second and third rings are identical to the first ring, but have jet diameters of 0.35 cm (roughly halving the jet area of the baseline) and 0.65 cm (roughly doubling the jet area of the baseline), respectively. These were chosen to provide a large range of test conditions in attempt to match trends seen by Bohan and Polanka [4]. These rings were tested at a constant core mass flow and cavity equivalence ratio of 3.24 kg/min and 1.76, respectively, for a CW flow direction. The full test matrix is shown in Table 11.

Figure 62. 0.35 cm, 0.45 cm, and 0.65 cm (from top to bottom) diameter air driver rings

Table 11. Cavity air jet diameter study test matrix at 3.24 kg/min core flow and cavity φ=1.76

Air Injection Diameter cm	Cavity Flow kg/min
0.35	0.72
0.35	0.90
0.35	1.08
0.35	1.26
0.35	1.44
0.45	0.72
0.45	0.90
0.45	1.08
0.45	1.26
0.45	1.44
0.65	0.72
0.65	0.90
0.65	1.08
0.65	1.26
0.65	1.44

Finally, the DPIV software [41] was used to analyze the flow velocity in the cavity for the 0.45 cm diameter. The rig was run at a core-to-cavity split of 3.24/1.08 kg/min at an equivalence ratio of 1.76. This was then compared back to the pressure/temperature method of taking velocity/g-load data.

3.6.5. Cooling Effectiveness

In order to gain a better idea of what heat loads are applied to the rig, an infrared camera was used to capture material surface temperatures at different locations during burning. Then, the cooling air was applied at the same rig conditions to study the effectiveness it had on the material. The UCC was set up on the test stand with the rear quartz windows replaced with windows made from Hastelloy-X, shown in Figure 63, to ensure no quartz windows were destroyed while the cooling flow was turned off.

Figure 63. Exit of the UCC with metal inserts in place of the quartz windows on the rear cavity wall.

To study the surface temperature, a FLIR ThermaCAM SC640 with a temperature range of 233 to 1773 K, was used. The camera was set up in two locations to study each cooling scheme, as shown in Figure 64. Measurements were taken on the center body tail and rear cavity plate. To eliminate reflectivity, each test section was painted with high temperature, matte black paint.
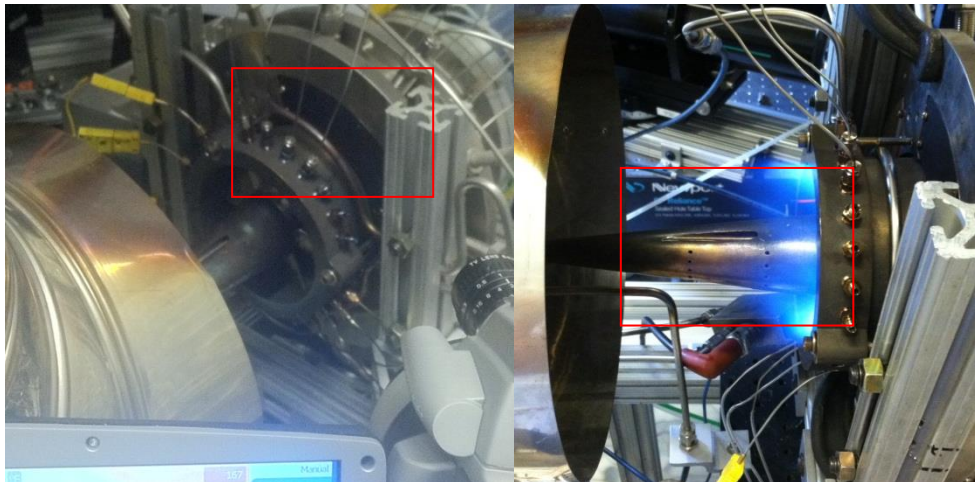
Figure 64. Camera imaging locations (boxed in red) for studying rear cavity (left) and tail cooling (right)

The test rig was run for 120 seconds with and without cooling at an equivalence ratio of 1.17, using 4.32 kg/min air in the core and 1.62 kg/min in the cavity, giving a core-to-cavity ratio of 73/27. 1.67 kg/min of cooling was split between the internal center body cooling passages, impingement jets on the rear cavity face, and the exhaust cooling ring. After 120 seconds, an image was taken and the rig was then shut off and cooled for the next test.

IV.   Results and Discussion

There were five primary objectives for this research. The results of each topic are

discussed and explained sequentially starting with the cavity swirl direction findings. This

investigation established the preferred direction for the remainder of the tests and most likely

future work. A stability map was subsequently generated identifying the lean blow out

conditions congruently with measurements of the cavity g-load. This established a baseline case

for the remainder of the g-load investigations and the Rayleigh loss measurements that followed.

Finally, measurements of the cooling effectiveness were obtained.

4.1.   Cavity Swirl Direction Results

The difference between the flow impacting the suction side (CW) and pressure side

(CCW) of the hybrid airfoil (shown in Figure 4) as products migrated from the cavity into the

core stream was substantial. Tests were conducted using the 0.45 cm jet diameter ring at core-to-

cavity splits of 3.24/1.08 kg/min and 4.86/1.62 kg/min air flow with equivalence ratios of 1.76

for each. The CW flow showed a consistent flame profile in the cavity flow, shown in Figure 65

and Figure 66 for the lower and higher mass flow cases, respectively. Products migrated radially-

inward and exited into the core along the suction side with minimal turning, as depicted. This

allowed the cavity flow to stay uniform and consistent over the entire time frame, with no large

flame intensity variations appearing from one moment to the next. This type of flame structure is

desired for consistent exit flow characteristics from vane passage to vane passage around the

annulus. Note that in both Figure 65 and Figure 66, the CW flow seems to be moving counter

clockwise, and vice versa. This is because the cavity image is reflecting off a mirror before being

90

detected by the camera. The CW and CCW are moving in the correct direction as they are labeled when looking at the front of the circumferential cavity.

The presumed benefits of swirling in the CCW direction were that the pressure side would be easier to cool than the suction side and that better pitch-wise temperature profiles could be achieved at the exit of the hybrid vane due to the natural migration of flow from the pressure surface across the airfoil passage to the suction surface. The CCW flow, however, revealed significant flow unsteadiness due to the exiting cavity flow needing to turn nearly 135° in order to exit the circumferential cavity into the core. This caused severe disruptions in the cavity flow field and increased g-load variation within the cavity itself, which is shown in comparison with the CW case in Figure 65. The CW flow is consistent and mostly uniform in time, while the flow field for the CCW varies substantially over 5 milliseconds. Lighting the rig became an issue while the flow was traveling in the CCW direction because of the disruptions and variations, and fuel injection had to be staggered flowing higher and lower fuel flows for every other injector in order to get the flow to ignite (with the ignition port fuel injector being on the low end, roughly one-tenth of the higher value), and then brought back to equal flows on all injectors at the desired condition. Also, a stagnation region was formed just downstream of the injector, where the next vane in the core is located, causing significant heating on the cavity and the OD of the vane and the exit tube. At a higher total mass flow of 4.86/1.62 kg/min, the flow structures in the circumferential cavity still show large intensity fluctuations for the CCW case. The heating on the vane and cavity walls is even more noticeable through the rise of pixel intensity on the inner radius of the cavity for the higher mass flows.
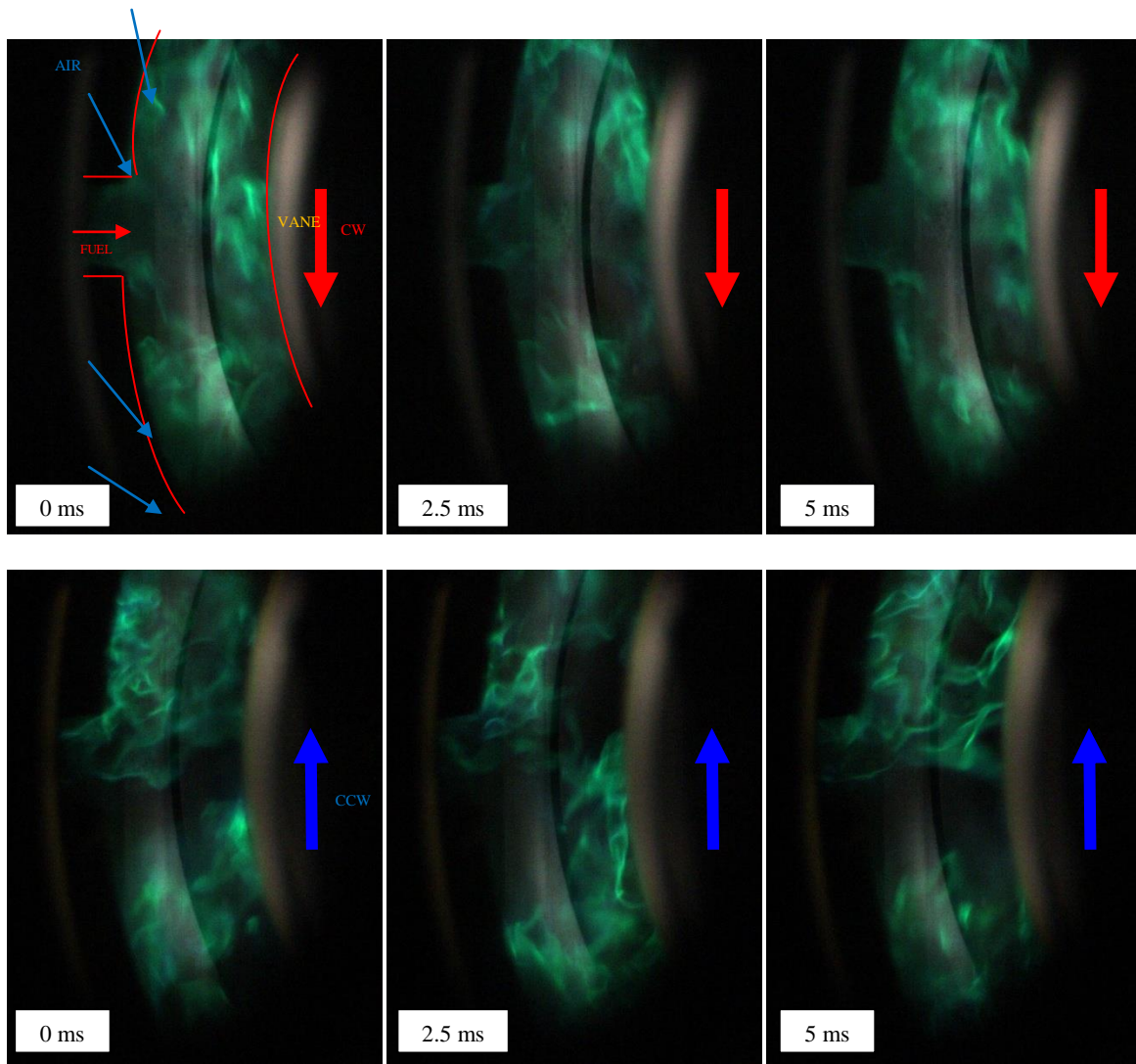
Figure 65. CW (top) and CCW (bottom) flows for 0.45 cm air injection at 3.24/1.08 kg/min core-to-cavity air flow
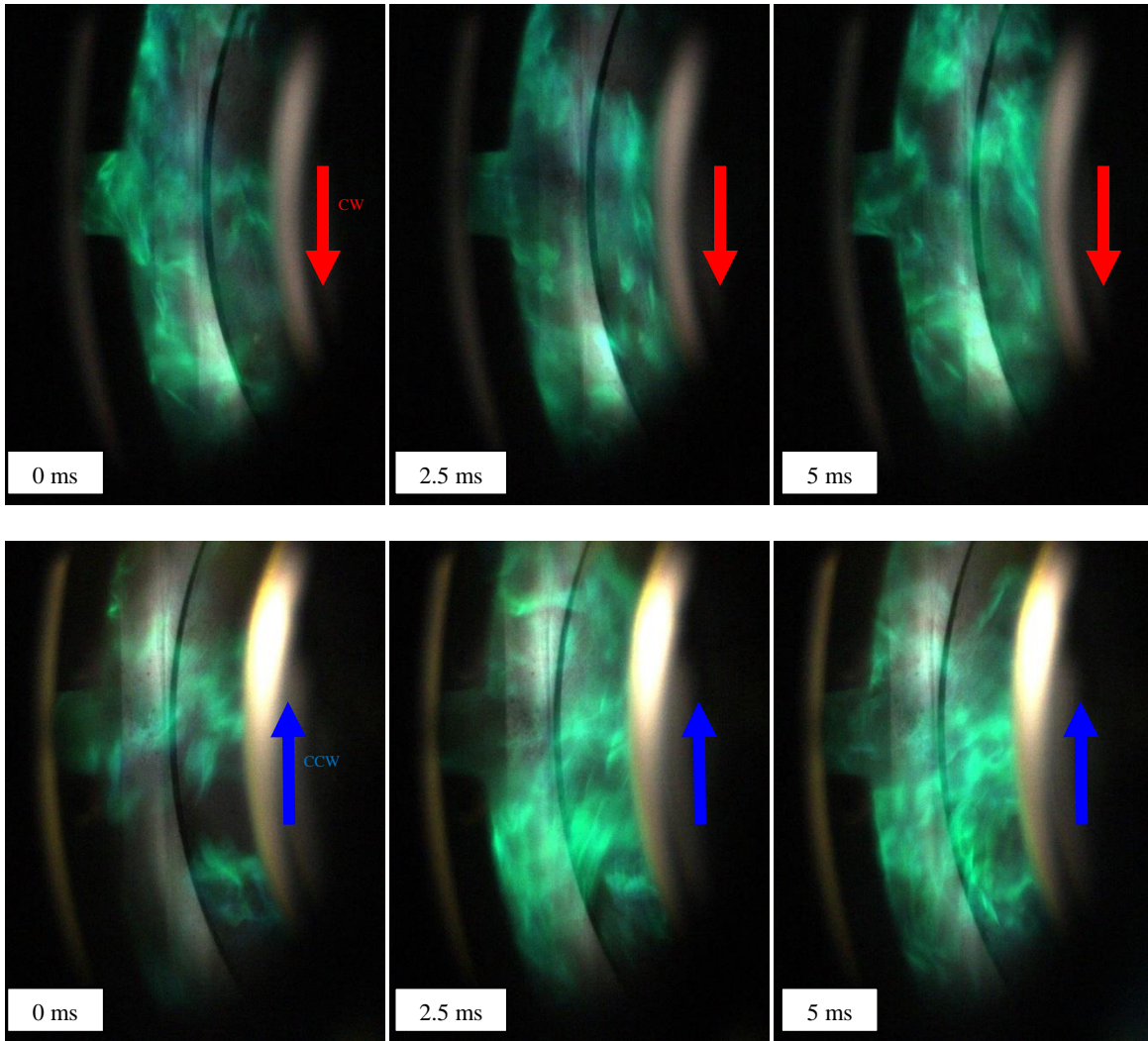
Figure 66. CW (top) and CCW (bottom) flows for 0.45 cm air injection at 4.86/1.62 kg/min core-to-cavity air flow

To better quantify the differences in the flame structure, MATLAB [40] was used to show average and instantaneous flame intensities for CW and CCW flows for the 3.24/1.08 kg/min condition. The gray-scale red channel was subtracted from the green and blue channels to remove the background and any light given off by heating of rig material (shown in Figure 67),

and that image was processed to determine flame intensities. The MATLAB codes are given in Appendix E.
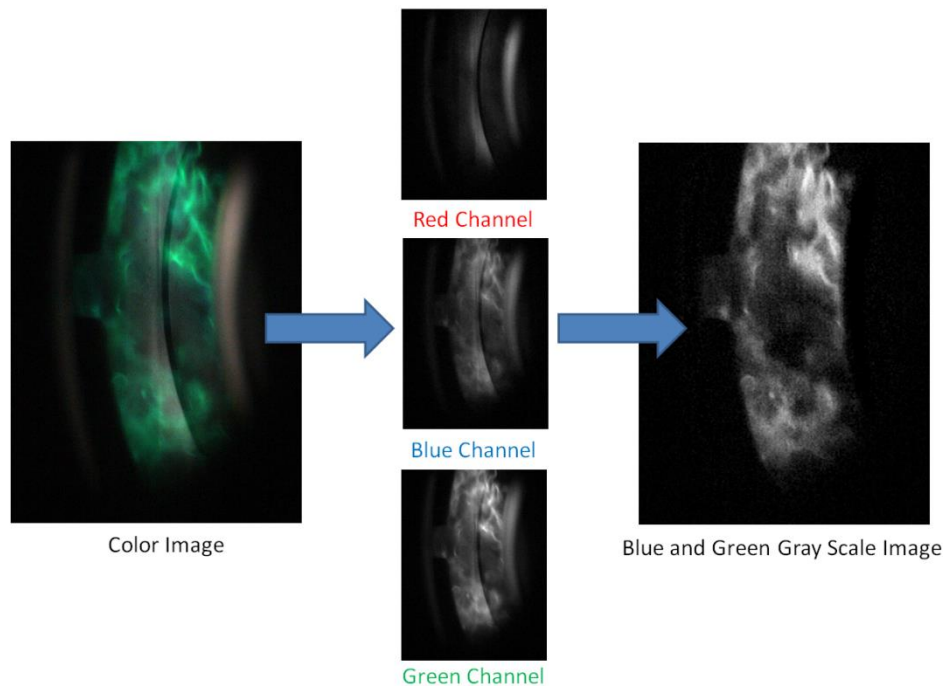
Figure 67. Conversion from color image to gray-scale blue and green channel image

The results showed more flame intensity at an instantaneous point in time in the CW case opposed to the CCW case, as shown in Figure 68, in which a clear discontinuity can be seen upstream of the fuel injector where little flame is present. Using an average of 45 images, the CW case shows more cavity flame coverage with a noticeable increase in intensity near the ID of upstream of the injector, shown in Figure 69. The path of the fuel can also be distinguished as a region of less flame as the jet of fuel is too rich to burn well and must mix with the air before burning can occur. The discontinuity seen in the instantaneous data is still present in the average data for the CCW case and further testifies to the CCW case having non-uniform cavity properties.

94
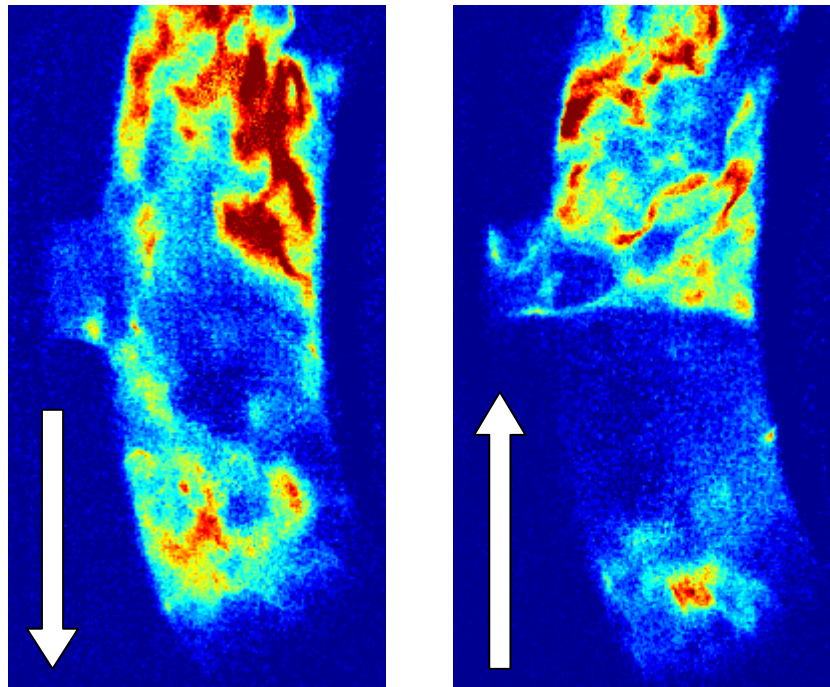
Figure 68. Instantaneous flame intensities for CW (left) and CCW (right) flow directions
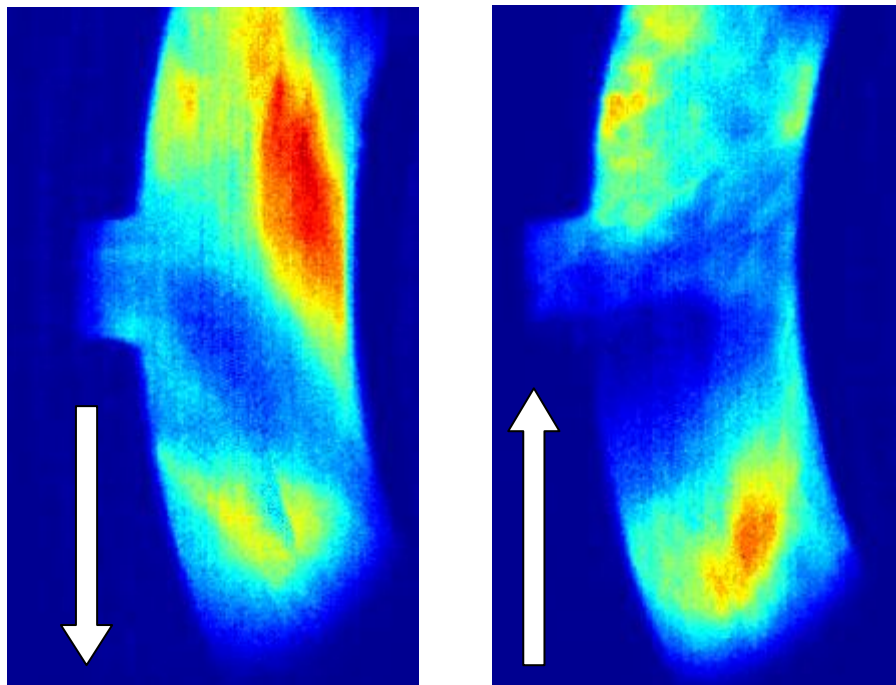
Figure 69. Average (45 images) flame intensities for CW (left) and CCW (right) flow directions

95

In addition to non-uniformities, the CCW configuration also resulted in a higher pressure loss at the exit of the rig for each of the flow cases. Table 12 highlights the increase in loss for the CCW cases as compared to the same flow condition in the CW direction for the 3.24/1.08 kg/min and 4.86/1.62 kg/min air flow splits and equivalence ratios of 1.76 for the 0.45 cm diameter air driver ring.

Table 12. Total pressure drop for CW and CCW flows for ϕ = 1.76 for 0.45 cm diameter air injection ring

Mass Flows (core/cavity) kg/min	Direction	Total Pressure Loss %
3.24/1.08	CW	1.05
3.24/1.08	CCW	1.20
4.86/1.62	CW	1.96
4.86/1.62	CCW	2.44

4.2.   Stability and Lean Blowout Results

Lean blowout testing was done on the 0.45 cm diameter air injection ring. Results of lean blowout testing revealed similar trends to those shown previously by Zelina et al. [11]: as mass flow, and therefore g-load, increased, a higher cavity equivalence ratio was needed to sustain the flame within the UCC cavity. Core flow was held constant at 3.24 kg/min and cavity mass flow was increased to increase g-load. Equivalence ratio was then decreased from a stable point down until blowout occurred, using high speed video data to quantify the flame structure in the cavity. Three different cavity phenomena were observed: stable flame, discontinuous flame, and no flame. The stable flame filled the entire cavity and was continuous, represented in Figure 70 by the 'Stable operating condition' points, with flow fields represented by Figure 71 at ϕ=1.55 and ϕ=0.99 (g-loads of 250 and 300, respectively). These high speed videos were focused at the cavity centerline and intense flames were visible around the full circumference and at all

instances of time. Fuel flow was reduced at constant air flow, which has the auxiliary effect of

increasing the cavity g-load, indicating increased fuel flows reduce g-loading (for gaseous fuels).
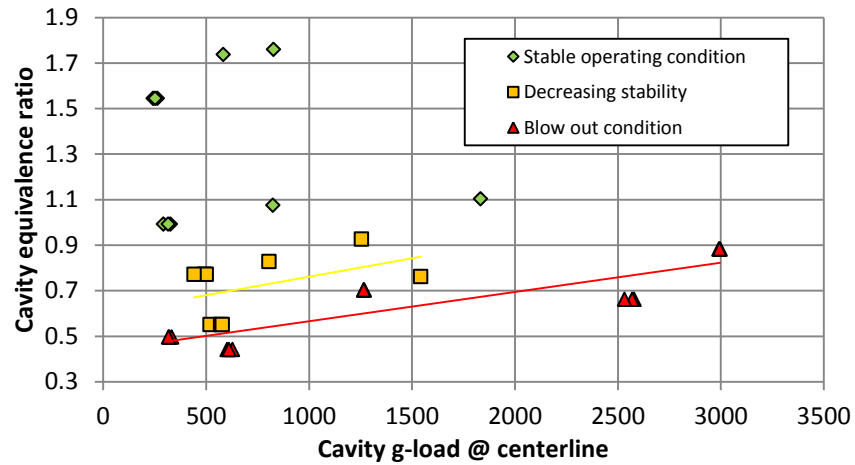
Figure 70. Stability and lean blowout points for 0.45 cm air injection diameter at a constant core flow of

3.24 kg/min
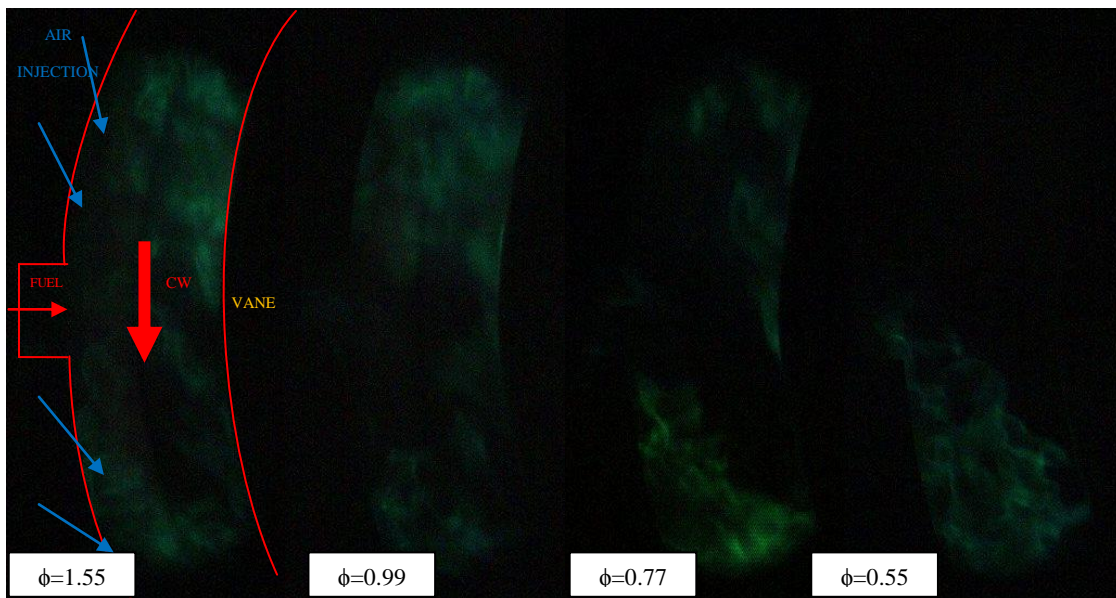
Figure 71. HSV progression at constant core-to-cavity air flow split of 3.24/1.08 kg/min

To better show the progression of flame degradation with decreased equivalence ratio, the MATLAB [40] outlined in Appendix E was again used to determine average flame intensities over 45 images for each case. Figure 72 more clearly shows the progression from a full cavity flame to a reduced flame only occurring at and directly downstream of the fuel injector. However, it also reveals a large pocket where no flame is present, even for the most fuel rich condition, and communicates a general idea of the location of the fuel and its path in the cavity.
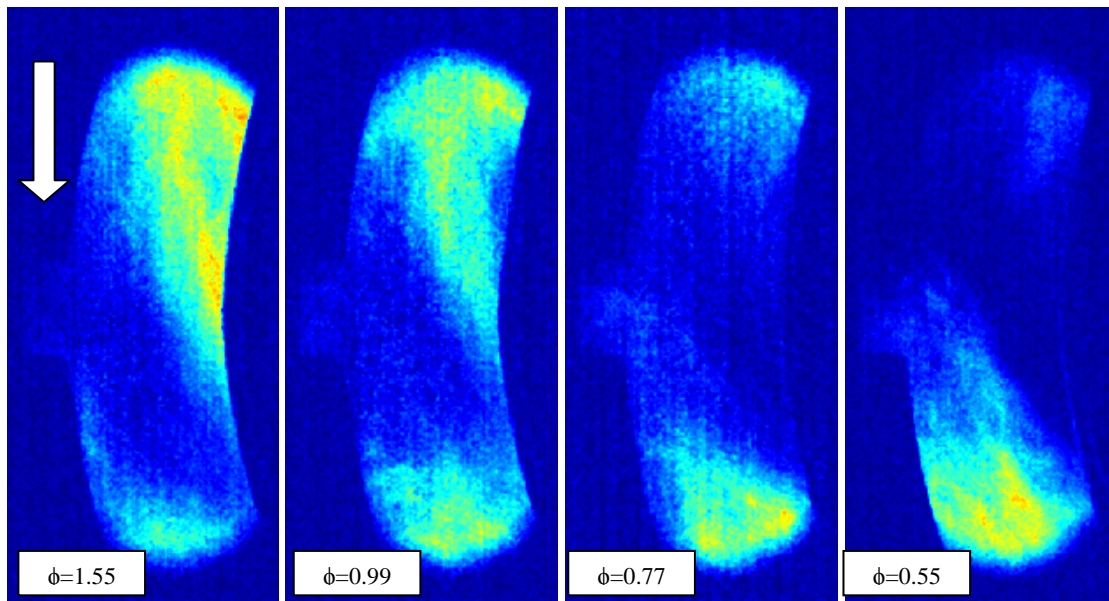
Figure 72. Time averaged flame intensities for 3.24/1.08 kg/min condition.

As fuel was decreased, an equivalence ratio was reached where burning fluid from one fuel injector no longer reached the next injector downstream, and the flow became discontinuous. This is represented in Figure 70 as the 'Decreasing stability' points on the chart and are represented by the images at ϕ=0.77 and ϕ=0.55 (g-loads of 500 and 530, respectively, in Figure 70) in Figure 71. Therefore, it was observed that although one can operate a UCC above

lean blowout, the process was not intrinsically stable. This decreased stability condition was further identified by the drop in the flame temperature within the cavity. At $\phi=0.77$, the temperature measured at the centerline averaged near 1150 K, and dropped to nearly 800 K when equivalence ratio was reduced to $\phi=0.55$. Further decrease of equivalence ratio enhanced these discontinuities until blowout occurred, which are designated as 'Blow out condition,' points in Figure 70. For this progression, blow out occurred at an equivalence ratio below 0.5 at an approximate g-load of 630. The trend line connecting all the measured blowout points represents an average, absolute limit to the equivalence ratio needed to sustain a flame at a given g-load.

Blowout and instability depended on several different aspects of the rig environment. It was noted that at a lower atmospheric pressure in the lab, cavity stability was decreased, as less back pressure existed at the rear of the rig, meaning lean blowout would occur at higher equivalence ratios. Data in Figure 70 was collected at an atmospheric pressure of 97.9 kPa (14.2 PSI). Also, as the temperature of the rig body was increased before testing for blowout (via longer run times), the blowout line actual moved to slightly lower equivalence ratios, as the cavity mixture could pull energy from the cavity walls to stay lit longer. The above results were done over one day and each time the rig was run for 60 seconds before taking data. This was to ensure all the conditions were the same for all data in Figure 70. Running longer before reducing fuel flow and testing for blowout would be expected to result in lower blowout equivalence ratios.

4.3. Cavity G-Load Results

The 0.35 cm, 0.45cm, and 0.65 cm air injection diameters were tested in order to provide experimental data to compare trends with Bohan and Polanka [4] for increasing air injection area

effects on g-load. The air injection ring with the desired diameter was inserted into the rig and tested at a constant core flow of 3.24 kg/min, while maintaining an equivalence ratio of ϕ=1.76 for cavity flows of 0.72 to 1.44 kg/min. Total and static pressure and temperature were taken to determine the tangential velocity at the mid-radius of the cavity, at both the centerline and quarter-line locations, using the setup shown in Figure 59. The centerline and quarter-line measurements were taken to determine if there was a significant velocity gradient in the cavity. Bulk velocity measurements were also studied for the 3.24/1.08 kg/min core-to-cavity air split at ϕ=1.76 using the DPIV [41] software, in order to verify these measurements were giving accurate results.

Trends showed that tangential velocity increased as air injection diameter was decreased for both quarter-line and centerline measurements. However, for each diameter size, the centerline g-load was higher than the quarter-line g-load until mass flows between 0.9 and 1.1 kg/min (dependent on the diameter) were reached, as shown in Figure 73. Past these mass flows, the quarter-line g-loading began to grow as a function of tangential velocity squared, where the center-line g-loads seemed to start leveling off for the 0.35 and 0.45 cm air injection diameters. This possibly indicates that the jets had reached a velocity at which they are unable to impart the majority of their momentum to the bulk flow, creating a velocity gradient within the cavity. Increased fuel flow could be acting as a jet in cross flow and blocking the centerline flow, as fuel flow was shown to decrease tangential velocity/g-loading in the stability/blowout analysis. The centerline tangential velocity for the 0.65 cm indicates it is still rising at the last mass flow point, indicating the larger holes had both slower speeds and continued to drive the bulk fluid at higher flow rates. The last mass flow point for the 0.35 cm diameter was not taken because the flame

100

experienced blowout believed to be due to the high variation of g-load within the cavity, before

necessary conditions could be met.
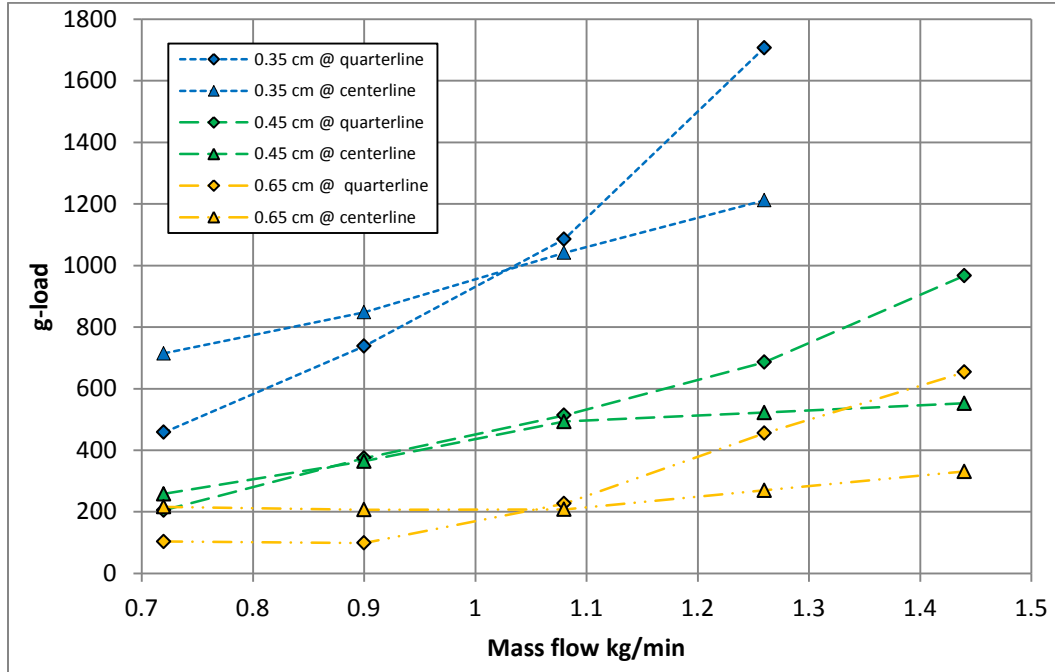
Figure 73. Effects of changing cavity mass flow at 3.24 kg/min core flow and ϕ=1.76 for three jet rings

The variation between the quarter-line and centerline may explain why blowout occurred

for the 0.35 cm diameter jets and not the 0.45 and 0.65 cm at higher mass flows. At the 1.26

kg/min cavity flow condition, the difference between the 0.35 cm quarter-line and centerline g-

load is nearly 500 and seems to be diverting more quickly with increased mass flow. At this

same location, the 0.45 and 0.65 cm g-load differences between centerline and quarter-line are

163 and 185, respectively. The tangential velocity gradients in the 0.35 cm may be enough to

cause blowout at this condition. Instabilities were also observed for the 0.65 cm diameter air

injection jets at lower mass flows than the 0.45 cm. With a cavity only 2.54 cm wide, two, 0.65

cm jets take up more than half of the width, possibly trapping fuel between two circumferential

sets of jets, which decreased residence time and mixing. This behavior was reported in experimentation done on a smaller rig by Anthenien et al. [9], where angled air driver slots (instead of to paired holes) were used to drive the circumferential cavity flow. It was reported that the slots trapped the fuel and reduced efficiency greatly, which led to the design of paired holes as the main flow driver design in the first place.

To verify the pressure/temperature method of determining the tangential velocity and g-loading in the cavity, the DPIV [41] software was used to determine an average velocity in the tangential direction near the mid-radius of the cavity, which was then used with Equation 2 to find g-loading. The image length correlation was 12.86 pixels/mm, which was determined using the 10.16 mm fuel cavity width clearly shown in each cavity image. Time between images is 0.125 ms at 8000 frames per second. The correlation of the two images for the 3.24/1.08 kg/min core-to-cavity split at $\phi=1.76$ is shown in Figure 74. Once a correlation is made, an average vector can be extracted for a given area in the image, shown in Figure 75.
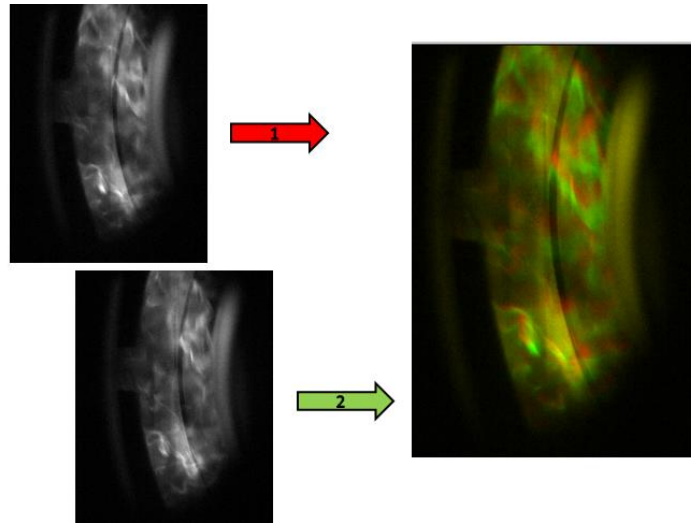
Figure 74. Correlation using DPIV software [41] of two images at a 3.24/1.08 kg/min core-to-cavity split at $\phi=1.76$
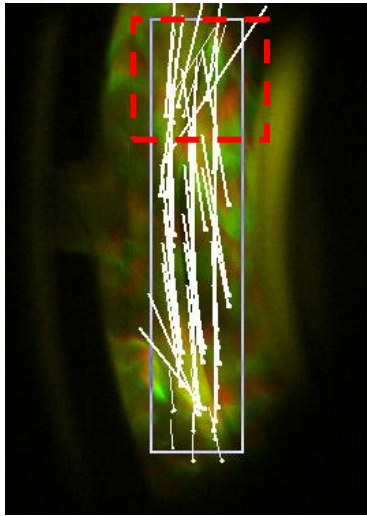
Figure 75. Velocity vectors for center-radius correlation at a 3.24/1.08 kg/min core-to-cavity split at

$\phi=1.76$

The measured pressure/temperature velocity and g-load was 18.22 m/s and 503.4 (average between quarter-line and centerline probe data), respectively. Averaging the vectors (listed in Table 13) nearest to the probe location in Figure 75 (near the top in the smaller boxed section) resulted in a velocity in the tangential of 17.55 m/s, corresponding to a g-load of 466. Tangential direction was determined by only taking vectors that were in-line with the cavity walls in this box. The resulting velocity is within 7.5% accuracy to what the pressure/temperature probe was reading, giving confidence that these are accurate methods of measuring the tangential velocity and g-load. These were the only vectors used as it is expected that a velocity gradient in the circumferential direction exists due to the radial fuel flow slowing the bulk air flow at injection locations.

Table 13. Vectors used for average calculations in dashed, red box of Figure 75

Velocity Vector Magnitude m/s
9.63
16.45
23.41
17.59
19.87
20.73
18.58
21.79
9.90

While this is extremely useful for showing velocity vectors within a flow field, the software requires extensive post processing time to convert files to black and white and import them into the program. Also, quartz windows are also more vulnerable to damage from heat and can even leak if extensive pressure builds up in the cavity, impacting measurements and flow within the cavity. The pressure/temperature method has the potential to provide instantaneous g-loading data and operate in harsher/hotter environments within the cavity, although it was noticed that after 10-15 test cases, the probes themselves began to wear, and would even begin to sag during longer runs or near 25 test cases, due to the heat load and gravity. This necessitated adding new total pressure probes every 10-15 runs, making both methods time consuming.

4.4.   Rayleigh Loss

The Rayleigh loss was characterized by taking total and static pressure measurements at the inlet of the core and the exit of the rig. Initial measurements were taken at a core-to-cavity split of 6.02/1.08 kg/min and equivalence ratio of 1.75 and are shown in Figure 76. For the TCB, these flow rates led to exit Mach numbers of 0.19 and roughly a 200 K temperature increase for the reacting case and led to a total pressure drop at the exit of 2%. Aerodynamic losses during non-reacting cases were near 0.7%, resulting in a Rayleigh loss just over 1.3%.

104
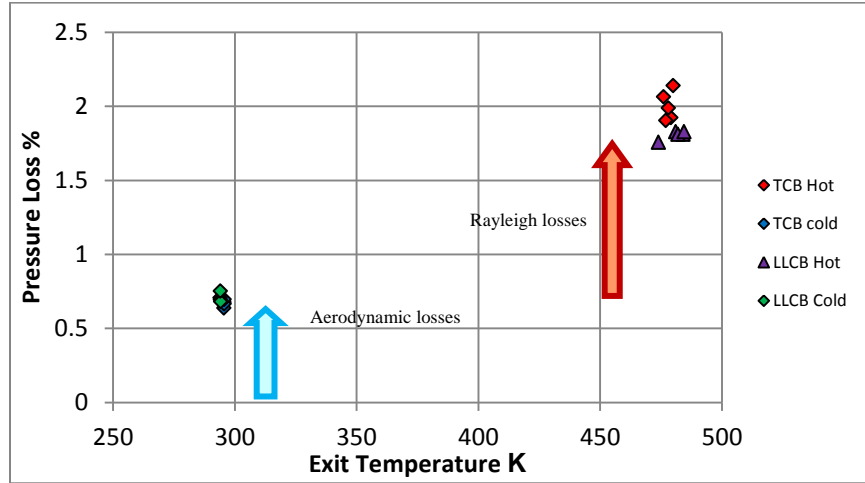
Figure 76. TCB Rayleigh loss measurements at 6.02/1.08 kg/min core-to-cavity split and equivalence

ratio of 1.75

The LLCB was under the same conditions as the TCB for the initial 6.02/1.08 core-to-cavity air flow split and equivalence ratio of 1.76 ($\phi = 0.3$ overall). These results are shown with the TCB results for comparison between the two in Figure 76. The LLCB had near the same aerodynamic losses as the TCB, however, there was a noticeable difference in Rayleigh loss of 0.23% between averages of the TCB and LLCB reacting cases. While this is low, the Mach number at the exit is not reflective of the higher Mach numbers that would be expected and these initial tests only serve as a baseline for higher mass flow cases and show an increased pressure loss with heat addition.

The second set of tests aimed at characterizing the effect of increasing equivalence ratio on the flow. Tests were conducted at a 6.84/1.62 kg/min core-to-cavity split at equivalence ratios from 1.47 to 2.02. Reacting Mach numbers were roughly 0.05 (just upstream of the hybrid vane) and the inlet and 0.25 at the exit, the latter of which was measured using pressure methods and

Equation 11 described in a previous chapter, and results for reacting and non-reacting cases for the TCB and LLCB are shown in Figure 77. Rayleigh loss tended to increase with equivalence ratio as shown in Figure 78, which is expected.
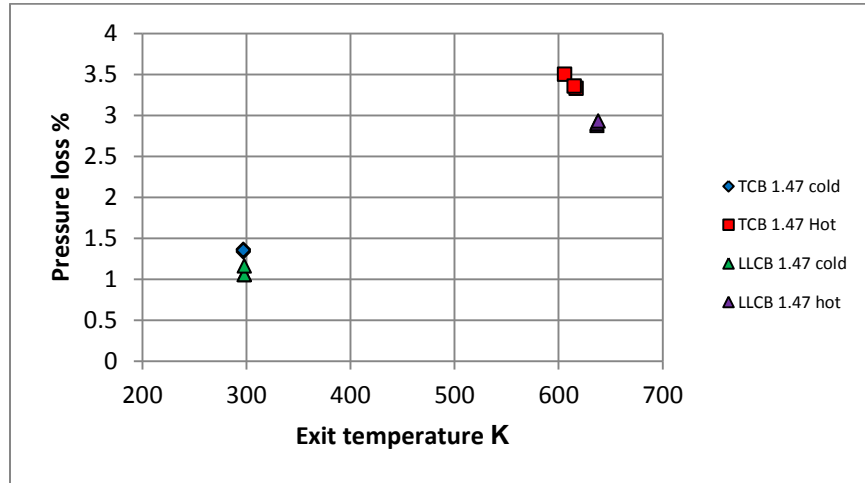
(a)
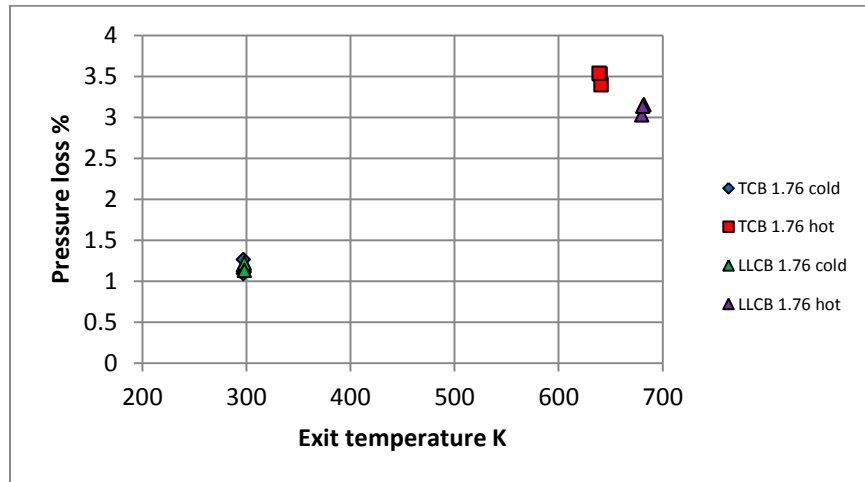
(b)
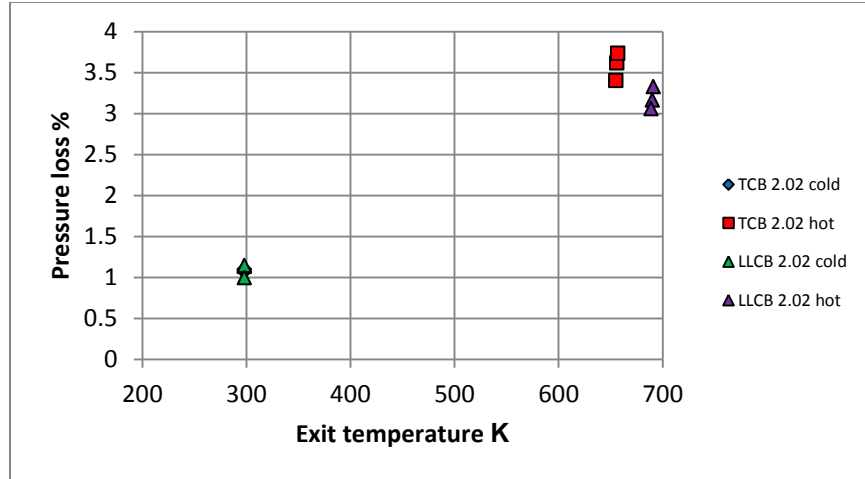
(c)

Figure 77. Losses for the TCB and LLCB at 6.84/1.62 kg/min core-to-cavity split for a) ϕ=1.47, b)

ϕ=1.76, and c) ϕ=2.02
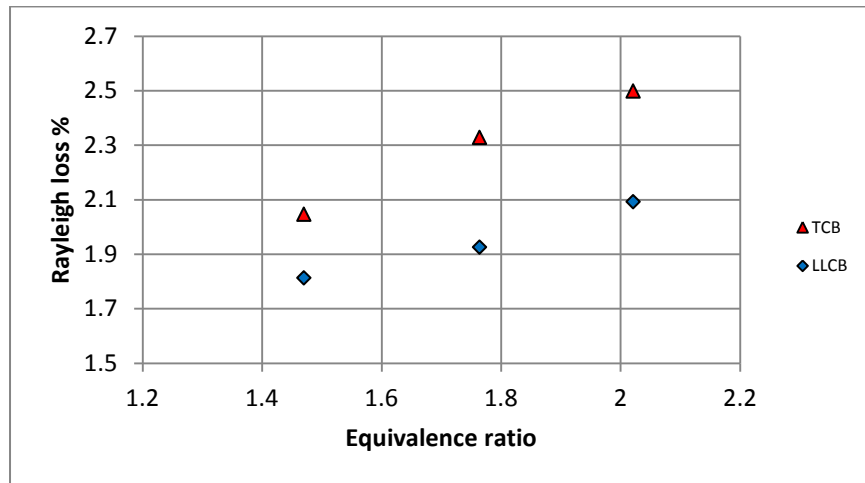
Figure 78. Equivalence ratio effect on Rayleigh loss at 6.84/1.62 kg/min core-to-cavity split

The temperature gain for these cases is notably small for the equivalence ratios that are

being tested. This is due to the cold core air that dominates the flow split. Only 19% of the air is

going to the cavity to burn before rejoining the core, causing overall equivalence ratios to be

107

extremely low (0.28, 0.34, and 0.39, for the cavity equivalence ratios of 1.47, 1.76, and 2.02, respectively). The 70/30 flow split fuel requirements to reach cavity equivalence ratios of 1.5-2.0 at the desired exit Mach numbers are not supported by the available fuel mass flow controllers. While rated for 70 SLPM of propane, the MFCs did not provide a fuel input past 55 SLPM (two MFCs provided 55 SLPM each to obtain ϕ=2.02 case for the 6.84/1.62 kg/min air split) with the desired stability, and fluctuations up to ±1-3 SLPM were seen up to an input of 60 SLPM, where the controllers could no longer hold a steady value. The final test case was conducted at a core-to-cavity flow split of 7.92/1.8 kg/min and equivalence ratio of 1.82, which resulted in a reacting Mach number of 0.061 at the inlet and 0.31 at the exit. Because of the higher Mach number, higher losses are seen, even though the temperature rise is not substantial. This condition for the TCB and LLCB is shown in Figure 79. Rayleigh losses were 2.84 and 2.91 % for the LLCB and TCB, respectively, only giving a 0.07% pressure recovery over the baseline. With increased fuel flow, the desired exit Mach number could be reached for the correct flow split, and would be expected to generate even higher losses.
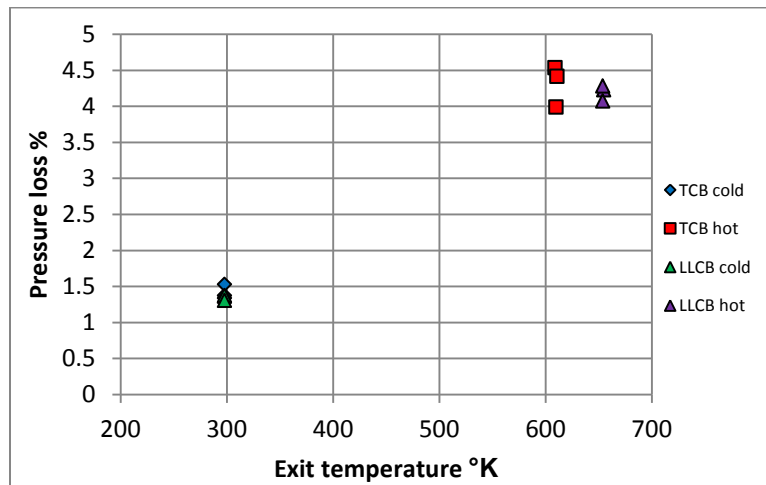
Figure 79. Losses for 7.92/1.8 kg/min air flow split and equivalence ratio of 1.82

108

It is worth pointing out all the reacting, LLCB cases have a higher temperature gain for each set of test cases. Since these cases were taken on the same day, under the same lab conditions, and run for the same amount of time before taking a sample, it is indicative that more burning is happening in the LLCB case. Because the LLCB was designed to slow the flow at the point of cavity-to-core migration, the remaining reactants from the fuel rich cavity have more time to burn in the cavity before exiting the rig, allowing for a more complete burn, and increased exit temperature versus the TCB.

Calculated and measured Mach number data is shown in Table 14 for each case at the three locations shown in Figure 61. In each case, the reacting flow seems to create greater downstream pressure, which has the effect of lowering the Mach number, if only slightly, upstream. As expected, increased heat addition and mass flow raise the Mach number at the exit of the rig. Also, for the most part, Mach numbers for the LLCB cases are lower than the TCB cases. This was expected as the LLCB has more area within the vanes to do burning the exit.

Table 14. Measured and calculated Mach numbers for each flow split (hot and cold) for TCB and LLCB

Core-to-Cavity Split kg/min	Reacting/Non-reacting	Equivalence Ratio	Center Body	Average Measured Inlet Mach	Average Calculated Mach Upstream of Hybrid Vane	Average Measured Exit Mach	Pressure Loss %
6.02/1.08	Non-reacting	1.75	TCB	0.040	0.062	0.164	0.67
6.02/1.08	Reacting	1.75	TCB	0.036	0.058	0.210	2.00
6.02/1.08	Non-reacting	1.75	LLCB	0.035	0.054	0.153	0.71
6.02/1.08	Reacting	1.75	LLCB	0.033	0.050	0.203	1.81
4.86/1.62	Non-reacting	1.47	TCB	0.037	0.058	0.172	1.42
4.86/1.62	Reacting	1.47	TCB	0.034	0.052	0.262	3.28
4.86/1.62	Non-reacting	1.76	TCB	0.042	0.066	0.187	1.16
4.86/1.62	Reacting	1.76	TCB	0.032	0.049	0.267	3.49
4.86/1.62	Non-reacting	2.02	TCB	0.039	0.061	0.181	1.09
4.86/1.62	Reacting	2.02	TCB	0.036	0.056	0.268	3.59
4.86/1.62	Non-reacting	1.47	LLCB	0.042	0.065	0.178	1.09
4.86/1.62	Reacting	1.47	LLCB	0.031	0.048	0.243	2.95
4.86/1.62	Non-reacting	1.76	LLCB	0.040	0.063	0.186	1.18
4.86/1.62	Reacting	1.76	LLCB	0.033	0.051	0.247	3.10
4.86/1.62	Non-reacting	2.02	LLCB	0.038	0.060	0.180	1.09
4.86/1.62	Reacting	2.02	LLCB	0.032	0.050	0.254	3.18
7.92/1.8	Non-reacting	1.82	TCB	0.045	0.071	0.205	1.41
7.92/1.8	Reacting	1.82	TCB	0.037	0.058	0.310	4.32
7.92/1.8	Non-reacting	1.82	LLCB	0.042	0.066	0.198	1.35
7.92/1.8	Reacting	1.82	LLCB	0.038	0.061	0.298	4.19

4.5. Cooling Effectiveness

Images were taken of the back surface of the UCC test rig using the FLIR IR camera to quantify the effectiveness of both the impingement cooling on the rear cavity wall and the center body cooling that exhausted at the tail. The rig was run at a core-to-cavity split of 3.24/1.08 kg/min and equivalence ratio of 1.76. A flow rate of 1.67 kg/min of cooling air was split between the inner center body cooling flow, rear cavity cooling jets, and the exhaust flow cooling ring. This was a preliminary study and was only meant to provide a reference for future cooling schemes. Results, shown in Figure 80, indicated the cooling on the rear cavity wall reduce the max temperature by 100 K on the rear wall, moving the max wall temperature in the 'box' from 723 °F (657 K) to 543 °F (557 K). Internal center body cooling exiting out of the tail also

110

reduced the max tail temperature in the 'box' from 529 °F (549 K) to 449 °F (505 K), which is a

44 K reduction, shown in Figure 81.
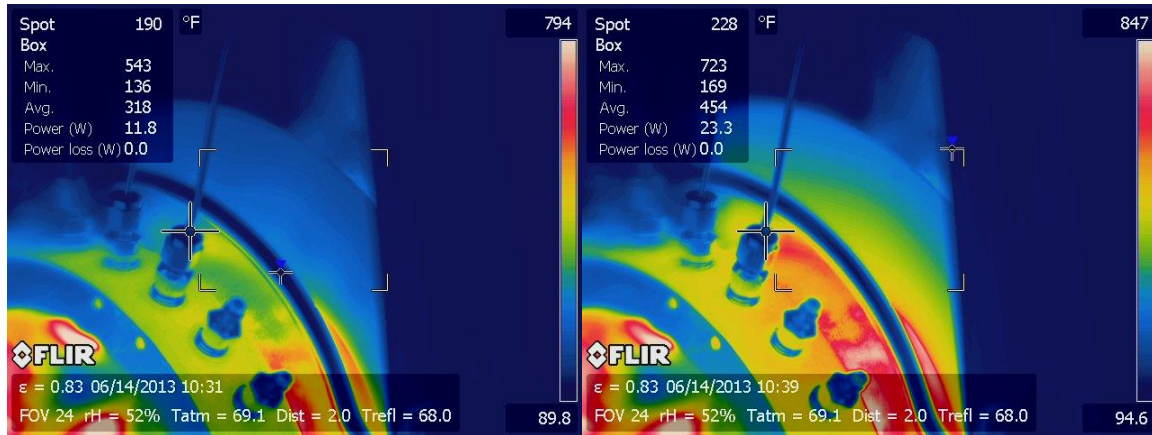
Figure 80. Rear cavity wall IR images with cooling on (left) and off (right)
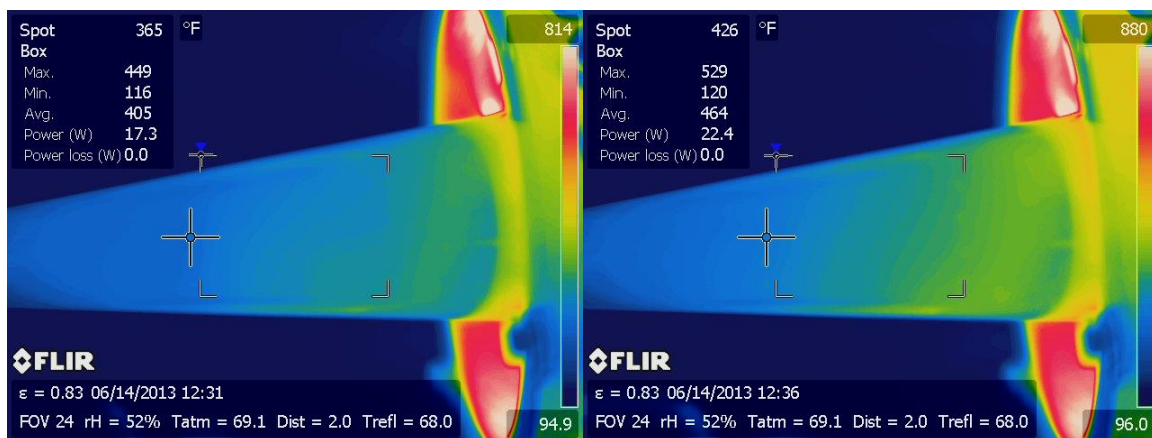
Figure 81. Tail IR images with center body cooling on (left) and off (right)

The center body and rear cavity plate cooling techniques were effective for flow splits of

80/20 because there was significantly more cold, core air than hot cavity flow. At core-to-cavity

splits nearer to 70/30, hotter exit temperatures are expected, and the center body vanes,

especially nearest the OD, and rear exit tube will likely see significant heating, limiting the

duration of each test based on material limits. With cooling in place, tests were run, at most, just over 7 minutes without any damage occurring to the rig. However, instrumentation was damaged after multiple (15-20) runs and needed to be replaced after long tests series, as their material properties were not on par with those of the rig body. Longer testing would require more cooling mass flow applied to the rear cavity wall, exit tube, and center body sections. Active cooling applied to the front of the cavity as well is recommended for future testing. Further cooling schemes applied to the center body section, such as film cooling, will ensure a longer rig lifetime.

V.   Conclusions and Recommendations for Future Work

Upgrades to the COAL Lab were carried out in order to achieve main research objectives of determining proper swirl direction in the UCC cavity, mapping flame stability, studying cavity g-load, and mitigating Rayleigh loss. This chapter outlines the conclusions of both the upgrades and testing discussed in the previous chapters.

5.1.   Facility Conclusions

A new UCC test rig was designed, built, and installed in the COAL Lab for testing multiple aspects of high g-loaded combustors. Power and signal lines were rerun separate from one another to avoid interference, and new gas lines were run to the rig and emissions analyzer. Valves and regulators for the new air line system were set up and an additional propane line installed for additional fuel flow. The control station for the rig was completely gutted and redone to allow control of air flow, gas flow, emissions, pressure, and temperature measurements, and video monitoring all from one location. Once the lab was operating effectively, testing began on the UCC rig.

5.2.   Test Conclusions

The main objectives of the preliminary tests done on this test rig were to determine the correct cavity flow direction with respect to the hybrid vane, define the stability region of the cavity flame, understand and mitigate Rayleigh losses that result from heat addition at high Mach number study effects of air injection diameter on the g-loading in the cavity. These objectives were established to provide a baseline reference for in depth studies into each one of these fields.

5.2.1. Swirl Direction

The circumferential cavity flow showed extreme differences when impacting either the suction side or pressure side of the hybrid vane. The CW flow, or suction side impact, resulted in a more uniform flow field within the cavity, where products could migrate steadily out into the core flow. CCW flow, or pressure side impact, resulted in large intensity gradients in the cavity, with stagnation regions forming downstream of the fuel injectors. This stagnation region translated directly into significant heating on the vanes and rear cavity wall. A pressure drop was also seen between the CW and CCW cases. These results favor swirl direction resulting in a suction side impact, for which the rest of the tests were done. More advanced cooling schemes would be needed to be able to operate with a pressure side vane impact, but may lead to enhance mixing and better efficiency.

5.2.2. Stability Analysis

The stability region was defined for the 0.45 cm case, and lean blowout data showed trends similar to those in previous studies. However, it was discovered that lean blowout does not set the operating limits of the test rig. Cavity flow uniformity can be severely degraded before blowout occurs, where flame from the upstream fuel injector does not reach the next. This can severely detriment performance of downstream components and therefore the UCC should not be run in this area or non-uniform exit properties in the core may result.

5.2.3. Cavity G-Load

Air injection diameter was varied at the same mass flow and equivalence ratios and showed to effect g-loading in the cavity. Larger diameter injectors resulted in slower moving fluid in the cavity, while smaller holes moved fluid more quickly. It was noticed that the quarter-

line g-load began to increase faster than the centerline g-load for higher mass flows, which even led to blowout in the 0.35 cm case. The 0.65 cm case had also experienced blowout in previous testing before the 0.45 cm case, indicating a correlation between stability and air injector diameter. Camera images and computer software confirmed the velocity measurements made in the cavity using pressure and temperature, proving it was effective for determining g-load. This data can help lead to an optimized cavity air driver diameter for a desired g-load.

5.2.4. Rayleigh Loss

Heat addition was shown to increase the pressure loss in the test rig when comparing reacting and non-reacting flows. These Rayleigh losses increased with equivalence ratio and core Mach number (driven by mass flow). A low loss center body profile was developed and showed reduced losses over the baseline, tapered design, because of an increased passage area that led to lower Mach numbers during heat addition to the core. This low loss design also resulted in hotter exit temperatures in the core for the same conditions, indicating a more complete burn over the baseline. This type of geometry can be used in future designs of UCCs to increase pressure recovery and improve emissions.

5.2.5. Rig Cooling

Heat loads on the exit of the rig and throughout the center body region were reduced by the use of cooling air. Impingement air reduced heat loads by 100 K after 120 seconds of testing, indicating the rig could be successfully cooled using these techniques. The tail of the rig was cooled by 44 K, which is still significant and lends to the longevity of the rig's lifetime. However, because cooling flow passes from front to aft in the rig, cooling flow reaching the tail has already been in contact with hot sections in the rig and there is no longer as large of temperature

115

difference between the cooling fluid and hot surfaces, which decreases the fluids ability to extract heat.

5.3. Recommendations for Future Work

Even though much has been learned about the UCC test rig, it is still relatively new and there is much work to be done. There are many modifications that should be made to the rig and instrumentation methods in order to obtain better data. The rig itself experiences significant heat loads, especially on the rear cavity plate and exit tube OD. High heat, anti-seize lubricant must be applied to all bolts if they are expected to come back out of the rig. Also, it would be easy and inexpensive to replace the front and back cavity faces and the exit tube with modified versions that employ active, internal cooling mechanisms. This would allow for longer runs and overall lifetime of the test rig. A more complex cooling scheme would be required to remove heat from the hybrid vanes, but it would be necessary when running higher flow rates. The window sections of the rig are especially vulnerable to heating and getting blown out of place. A slight modification was already made to the holder for the window sections, which increased their seal to the cavity outer wall, but improvements could still be made so that the window could become a permanent part of the rig, not just added when optical access is required for a test point.

The fuel baffles were not used because the led to sidewall fuel spillage that, in some cases, managed to migrate back into the outer plenum. A redesign of these baffles could be implemented to make them more effective, which would allow for better stability in the cavity, as fuel would be broken up into multiple streams at the fuel port locations, decreasing the blowing ratio.

116

Total pressure instrumentation was done using 0.159 cm stainless steel tubing, When used in a hot section of the rig, this tubing was subject to extreme temperature, and would sag or become ineffective after 10-15 runs, depending on the test cases. Cooled, total pressures should be designed for the cavity and core exit such that this no longer is an issue and test cases can be done more accurately, without changing probes out.

Tests reported in this document were also only taken at the mid-span of the core exit (for Rayleigh loss) and quarter-line and centerline ring locations at the mid-radius in the cavity (for g-load measurements). In order to better understand the g-loading in the cavity and the reported g-load variation, measurements should be made at multiple radius locations across the entire span of the cavity. This also applies to the core exit. Multiple span locations should be studied to better understand the differences in exit characteristics between the TCB and LLCB. Emission measurements also need to be done to quantify any improvements the LLCB may offer.

Finally, an optimization study needs to done on the air injection diameter within the circumferential cavity. Finding the optimum size would allow for the best stability qualities and would increase the operating range of the UCC, broadening its potential application base.

Temperature Span Measurements on Small Scale Sector UCC

Because the work of Parks and Polanka [19] and Parks [22] revolved around qualitative data for the rig (HSV and emissions), the same conditions were used to run the tiger claw RVC configuration to obtain pressure and temperature so that span-wise temperature and mass flow entrainment could be quantified. These test cases varied mass flow ratio (MFR) between the cavity and core to study flame structure and migration from the cavity into the core section.

An attempt to better quantify the temperature profile across the exit was done by moving the thermocouples across the span of the core. Quantifying the centerline span temperature was done using conditions from Parks and Polanka [19] and Parks [22] test cases 1, 4, and 5, which are all a 1000g case with MFRs of 0.1, 0.2, and 0.3, respectively. The thermocouples were held in place on either side of the rig, which sits on a single axis translation stage capable of precisely moving the rig side to side, thus changing the span location of the thermocouple. This was done for the baseline, angled RVC, and Tiger Claw RVC vane geometries. The results of this study are shown in Figure 82.

(a)

118
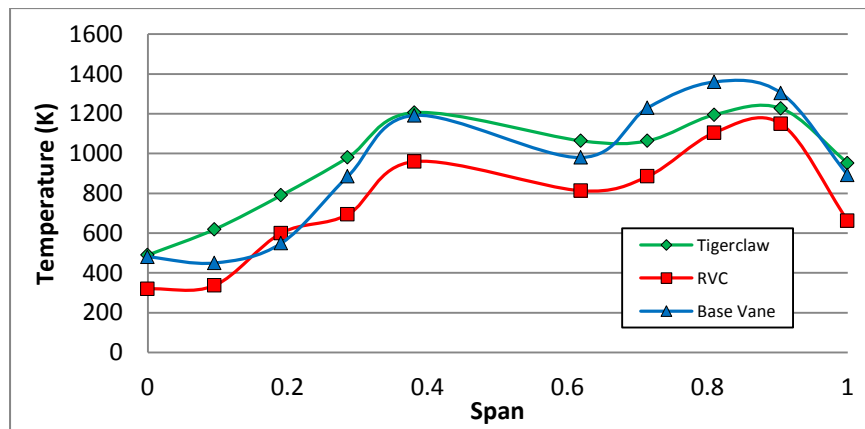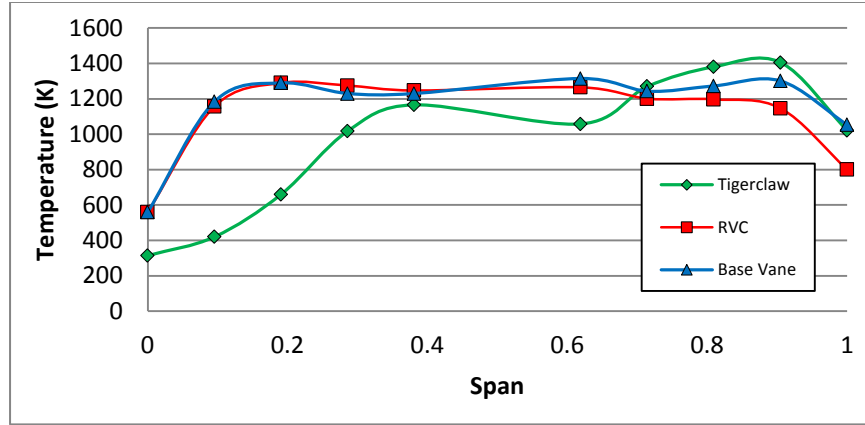
(b)
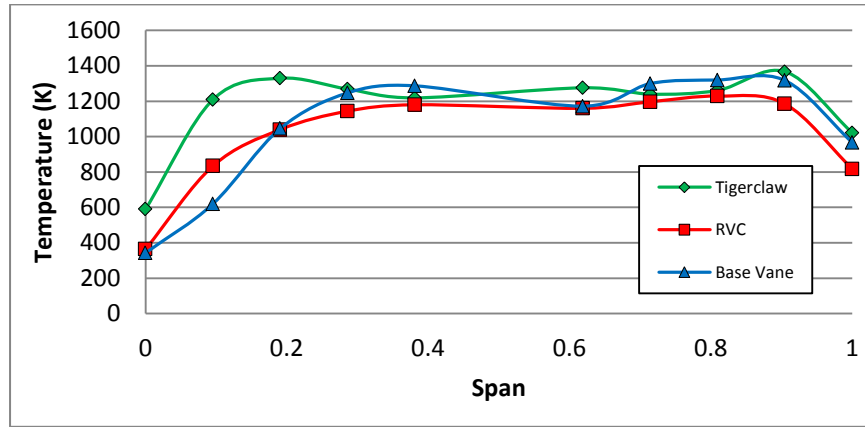
(c)

Figure 82. Span-wise temperature distribution at the exit for MFRs of (a) 0.1, (b) 0.2, and (c) 0.3

The final use for the small rig was to gain insight on the mass migration from the cavity section into the axial core. This is an important quantity as it indicates whether or not the sectional rig accurately represents the mass transfer expected in a full annular combustor. Total and static pressure and temperature were taken at a mid-pitch, mid-span location, just inside of the exit face. Static pressure and temperature provided estimation on the density of the flow using the ideal gas law, and using Bernoulli's principle for incompressible flow, a velocity was

found. Knowing the area of the channel, mass flow could be estimated using continuity, and the difference between the upstream mass flow and exit mass flow yielded the entrained mass from the cavity section into the core. A comparison between the tiger claw RVC, angled RVC, and baseline vane was done at MFRs of 0.1, 0.2, and 0.3 to study the effects of vane geometry on mass transfer. It was seen that the mass transfer out of the test rig was not accurate for what would be expected in a full-annular rig for any of the profiles, as less than 1/6th of the cavity mass flow was transported out into the vane passage, which was what would have been expected at the full annular condition.

Appendix B

Design of Fighter-Sized Ultra Compact Combustor

The small scale, sector model studied by LeBay et al. [20], LeBay [21], Parks and Polanka [19], and Parks [22] provided important and useful information on cavity and core interactions and migration, but was severely limited for several reasons. First, the core passage only simulated one side of a single vane passage, causing inaccuracy in flow migration. Second, the system was not designed with engine integration in mind, and Mach numbers and swirl angles were not replicated. Bohan and Polanka [4] designed a CFD model that more accurately represented a UCC section that could be used for a fighter/transport sized engine system and to verify this model, a large scale, sector UCC test rig was proposed with two vane passages in the core section and a 120° circumferential cavity. The cavity would feed the core with five fuel injection points upstream of the cavity/core interaction at a nominal g-load of 1000, based on the CFD findings of Bohan and Polanka [4].

The 120° circumferential cavity section was broken up into three major components: an upstream "seeder box", a high g-combustion section, and a circumferential optical section, shown in Figure 83. The seeder box was used to bring in the majority of the fuel and air, simulating the remaining 240° of cavity burning, as if it were a full-annular model. The seeder box furthermore served as the ignition source and the source for seed particles for PIV laser diagnostics. The combustion section of the cavity contains five fuel injectors and the corresponding number of air injection jets. Five upstream fuel injectors were selected based on CFD calculations required residence time of injected fuel particles. Fuel particles stay in the circumferential cavity approximately four vane passages downstream before complete

121

combustion and the products become light enough to exit into the core for this design [4]. The cavity combustion section of the rig, therefore, must be sufficiently long enough to allow for fuel from the first injector port to exit into the core flow section of the rig. This resulted in a 66° inlet combustion cavity, with the five fuel injection ports over the latter 48° of the section.

The remainder of the circumferential cavity included the region to interact with the core flow and an optical diagnostic section to understand the flow both entering the core flow and the flow progressing downstream in the circumferential direction. Previous measurements by LeBay et al. [20] and LeBay [21] of this flow in previous AFIT rigs were made aft of the rig exit where the flow lost g-loading and was able to interact with the ambient air. This made it difficult to precisely quantify the velocity within the circumferential passage and measurements of the shear at the core interface were unable to be determined. This optical access section in the current rig enables determination of these quantities.

The core passage section represents the axial flow of the engine. The core section was initially design based on Bohan and Plank's [4] axial cross-section geometry and hybrid vane turning. The initial core flow section was comprised of two passages. As shown in Figure 83, a full hybrid vane was located in the center with end walls comprising a suction surface and a pressure surface of the vane on the two sides. A system for removing a controllable amount of bleed air from the sides of the main core flow was designed, allowing for precise airflow through the passages and enabling the setting of the stagnation points on the airfoils. Boundary layer control on the passage walls was also possible with adjustable sidewall angles.
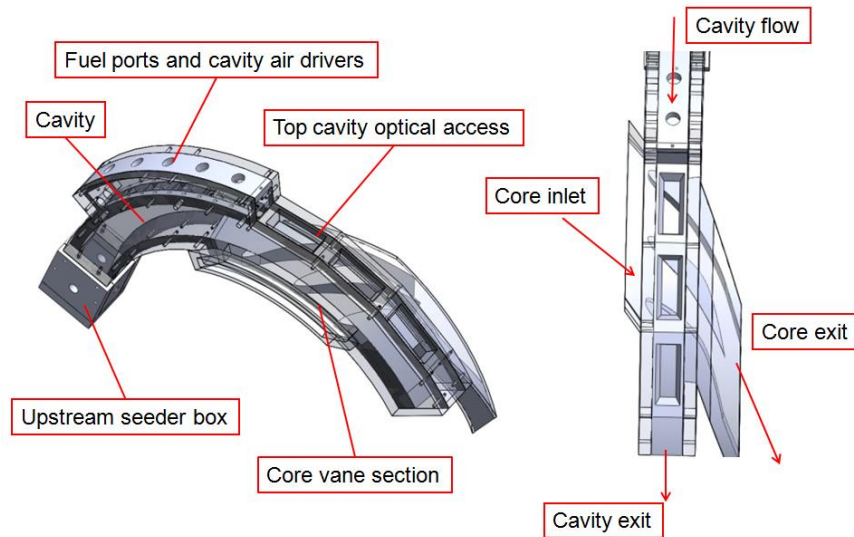
Figure 83. Initial design of UCC sectional rig showing components (left) and flow path (right)

A further modification was needed before a final design could be set, stemming from additional CFD work accomplished at AFIT. CFD analysis showed the Mach number through the initial design of the UCC system done by Bohan and Polanka [4] was close to Mach 0.3, with an exit Mach of approximately 0.35. For a typical, modern turbine engine, the Mach number off the compressor rotor stage was closer to Mach 0.6 and the turbine rotor inlet Mach number was approximately Mach 0.8. By design the UCC burns fuel rich in the circumferential cavity and a quenching and lean burning process occurs in the core flow. This results in a heat addition process at high Mach number if the core flow is not slowed underneath the circumferential cavity. A substantial Rayleigh loss was calculated under these Mach number flow conditions. This loss was proportional to the total heat addition and the inlet and exit Mach number. For higher heat addition and higher Mach numbers, total pressure loss increases. Typical annular combustors avoid this by diffusing the core flow as it enters the combustor below Mach 0.1. This keeps Mach number throughout the combustor relatively low until the exit. For the initial UCC

geometry, Rayleigh loss accounted for up to 12% pressure drop through the system at an average

Mach number of 0.3. The larger Mach number needed at the inlet and exit of the UCC system for

a typical engine would force the average Mach number to be high throughout the system and

further increase the Rayleigh loss.
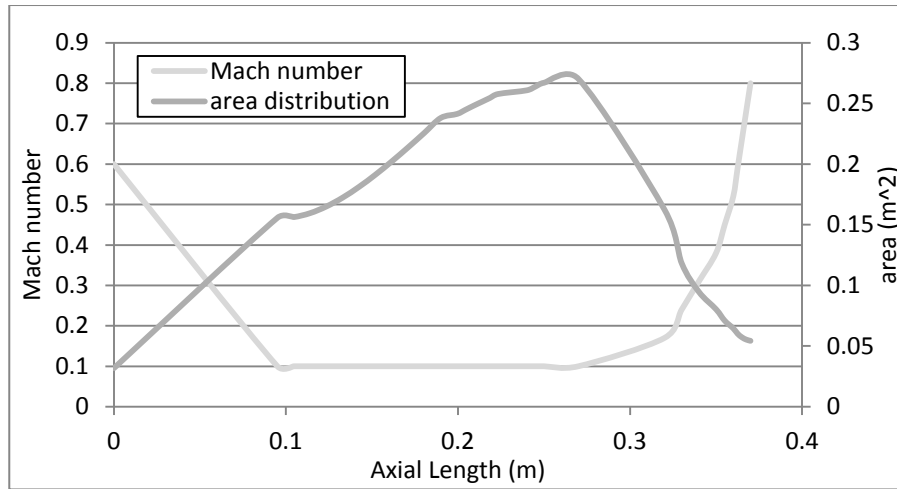
Figure 84. Ideal area distribution based on desired Mach number

The goal of the current geometry then was then to minimize the Rayleigh loss in the UCC

system while keeping fluid dynamics acceptable. The solution to this problem was to use mass

continuity and basic heat addition equations to develop a geometry that diffused incoming Mach

0.6 inlet flow down to Mach 0.1 before the UCC cavity interaction, and kept it at Mach 0.1 while

flow migrated out of the cavity and continued burning in the core. The flow was then accelerated

quickly to Mach 0.8 after the majority of all reactions had occurred. MATLAB [40] was used to

calculate areas through the core section to accommodate the required Mach distribution Figure

84. An ideal area distribution resulted in Rayleigh loss of 3.5%, which is a 70% decrease from

the initial geometry. A representative model with new core geometry was made designed, shown in Figure 85.

Figure 85. Representative full-annular UCC system cut-a-way

Appendix C
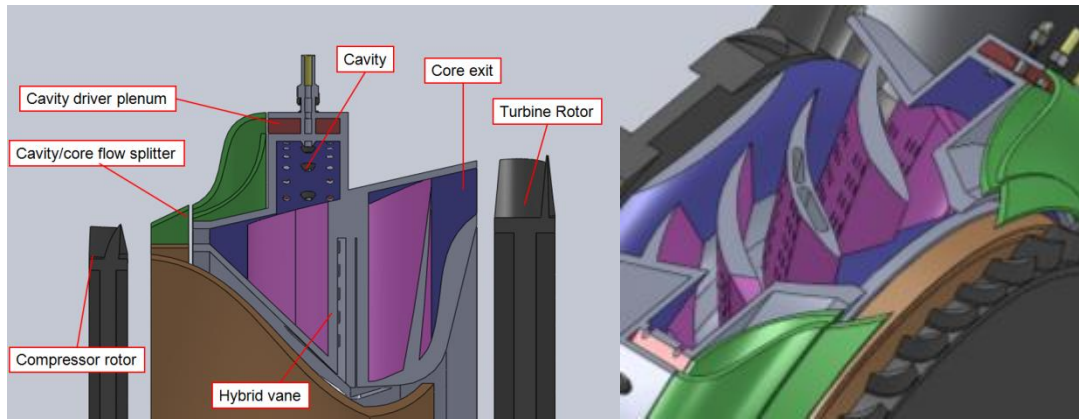
Lab Plumbing, Power, and Control Diagrams

Several modifications that were made to the COAL Lab required several existing systems to be rewired and new systems to be installed. Because the lab was essentially gutted and redone, new layouts were drawn in order to provide those who may need to make changes or install new equipment in the future with an understanding of the current setup. Included are the primary layouts for control, power, and gas lines.

Figure 86 shows the control layout in the COAL Lab. The central point of control using the control and high speed video computers is located at the control cabinet/desk pictured in Figure 56. This is also where the Eurotherm 2404 controllers for controlling airflow, the CAI emissions analyzer, CDAQ chasses and individual CDAQ cards for temperature and control inputs and outputs, relay boards for control and the CAI machine, the MKS 647C controller, and the DTC pressure system are located. FloServe valves and the Fox FT2 metering boxes are both located on the main air wall on the north side of the COAL Lab. MFCs 1-8 are located in the combustion box shown in Figure 52 and the two PLIF computers and three laser table computers are located on the second level of the laser tables immediately behind the control cabinet.

Figure 87 is a diagram of the power layout for major systems in the lab. Main power is supplied via a 120 VAC power line that runs into the control cabinet and is distributed on three blocks inside the cabinet and is turned on and off via the toggle switch at the front of the cabinet directly under the high speed video monitor. The blocks distribute power to the Eurotherm 2404 controllers, the Watlow heater control (which is not currently hooked up to the heaters), and to the main OPTO 22 PB24 relay board for each individual relay. Both the main OPTO 22 relay

126

board and the emissions relay board are powered by a 5 volt signal sourced from one of the two Lambda power supplies. The relays control solenoids for different flow lines both at the wall and in the combustion box, as well as controlling the spark ignition system, which is located on the ground near the UCC test stand.

The gas layout for the lab is shown in Figure 88 . The large propane tanks, LPG vaporizers, calibration gases, and other lab gases (excluding air) are kept in the Tank Farm outside of AFIT room 271 building 640. These are run into the COAL Lab through bundled copper pipe on the North wall beneath the air lines and go either to the CAI emissions analyzer or to the combustion gas box shown in Figure 52. Lab air comes from both the AFIT compressors (AFIT building 644) and the COAL Lab compressor (located outside of the COAL Lab) on the East wall and all control valves and regulators are located on the North wall for each of the three lines.
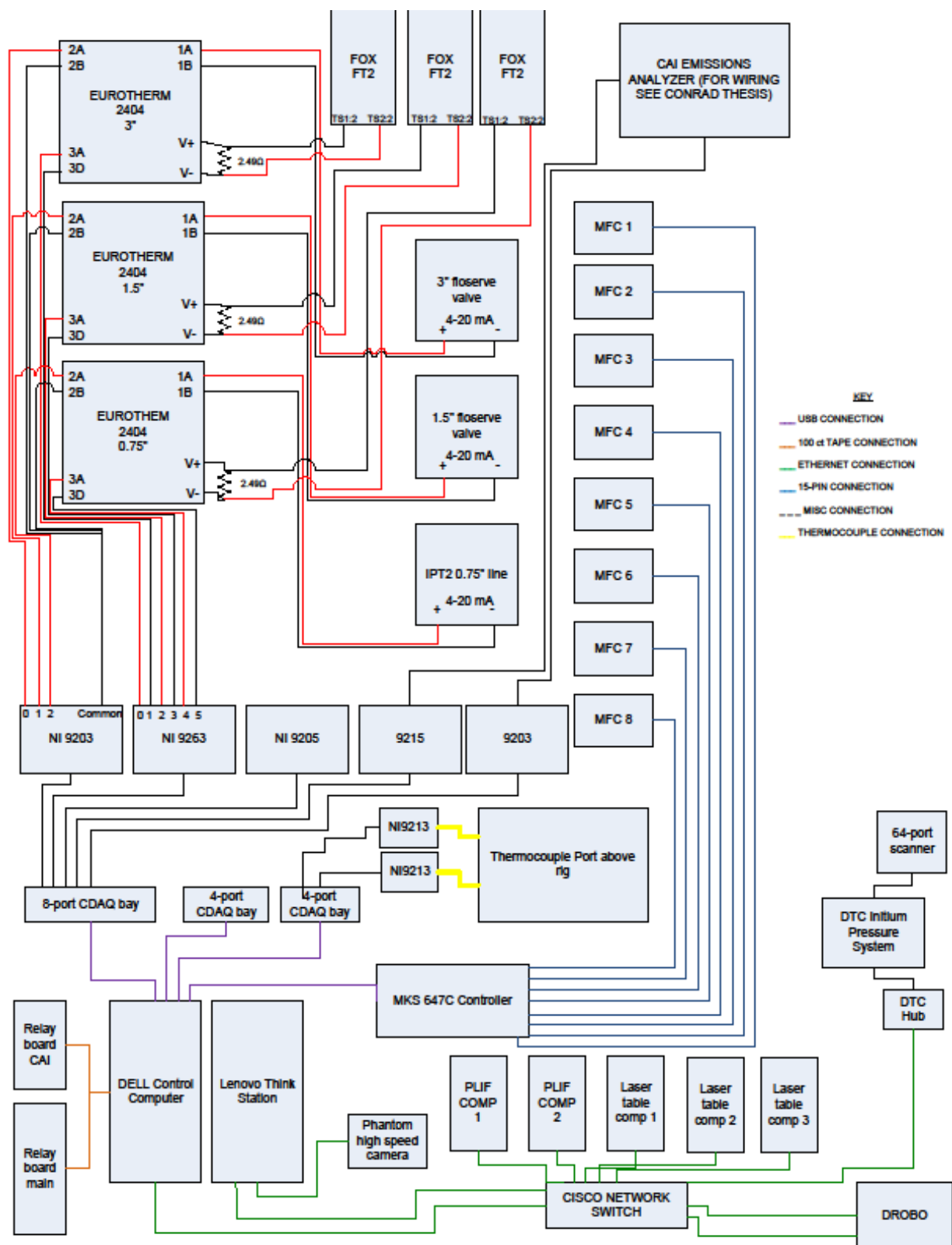
Figure 86. COAL Lab control and instrumentation layout
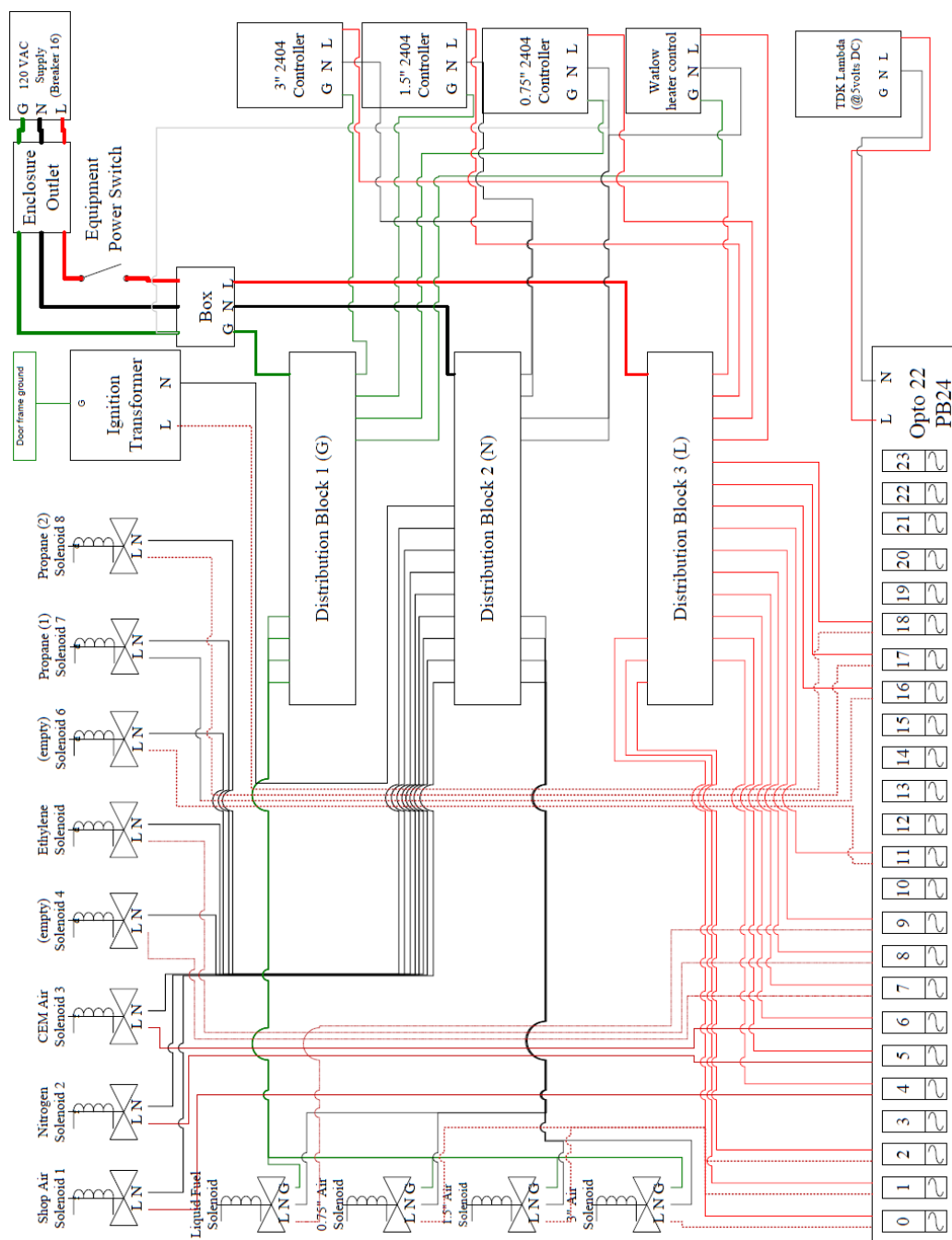
Figure 87. COAL Lab power layout
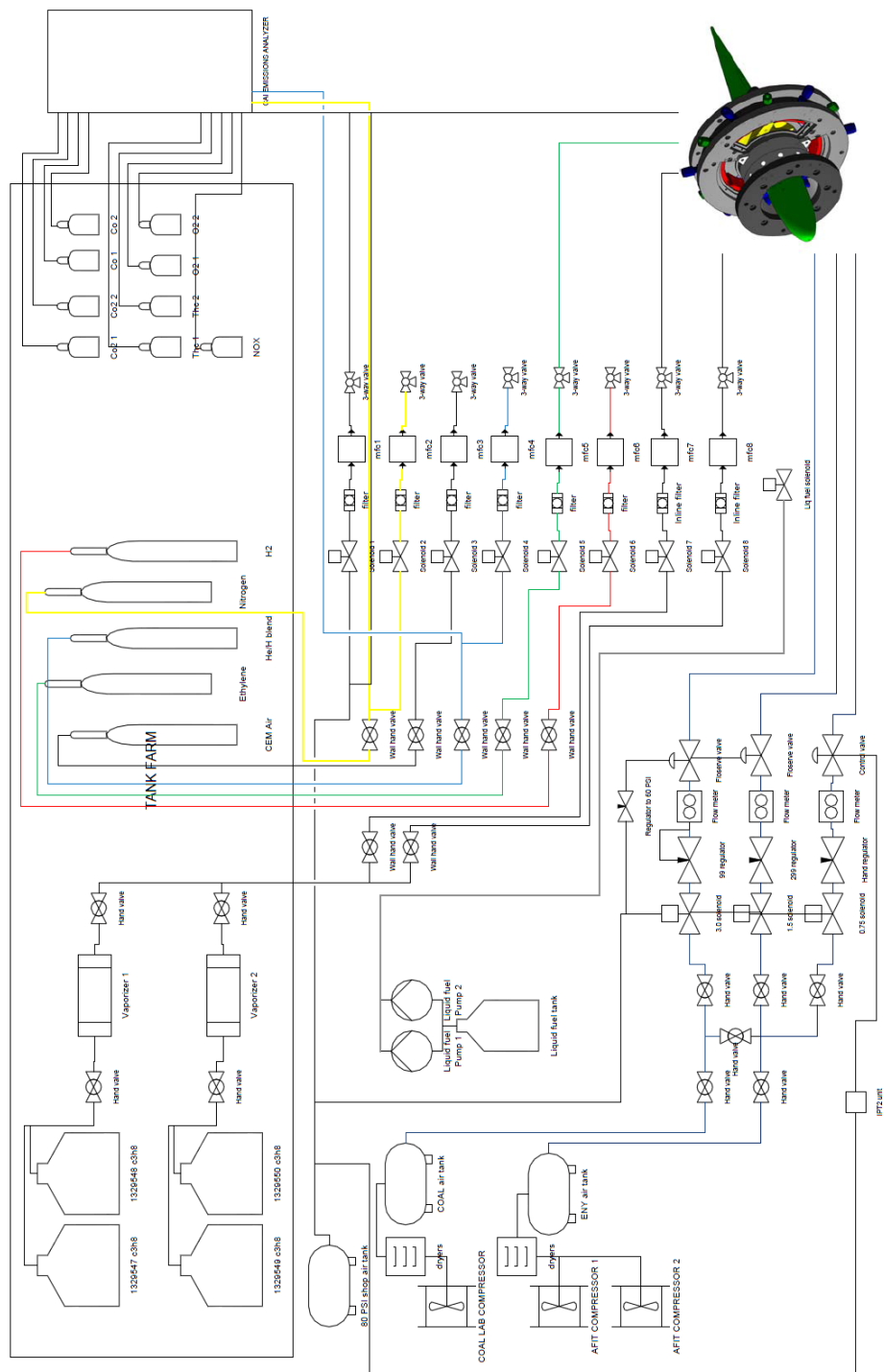
Figure 88. COAL Lab gas layout

Gas MFCs Calibration Data

The following calibrations were done for the MFCs that regulate the gas supply into the rig. These were done using the Definer 220 and 1020 mentioned in a previous chapter. The purpose of these curves is to provide a better accuracy for mass flows (mainly fuel) and therefore more accurately reported results. A linear curve fit was used to represent the calibration equation (shown on each plot) because it best represented the data.
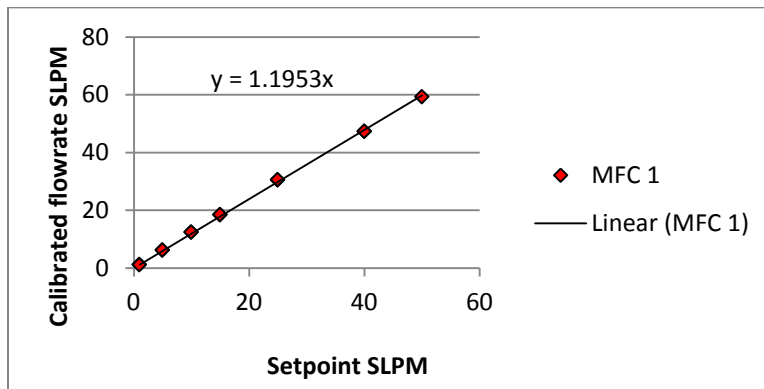
Figure 89. MFC 1 Calibration
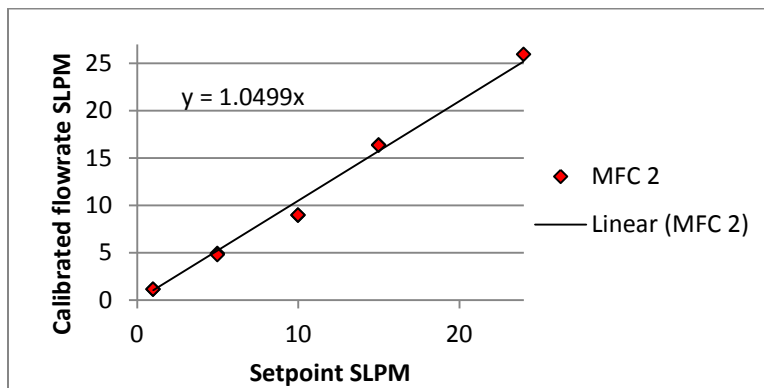
Figure 90. MFC 2 Calibration
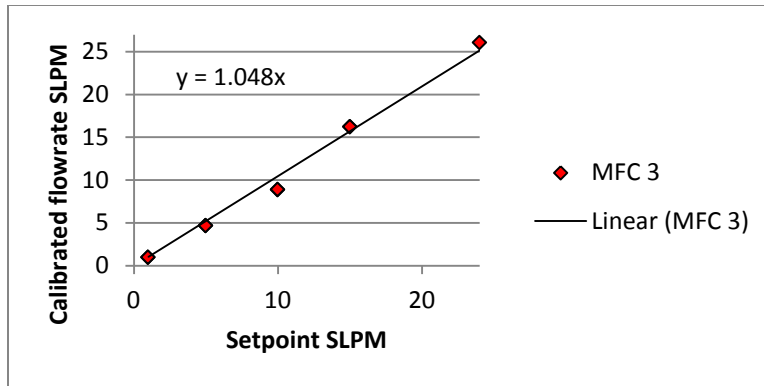
Figure 91. MFC 3 Calibration
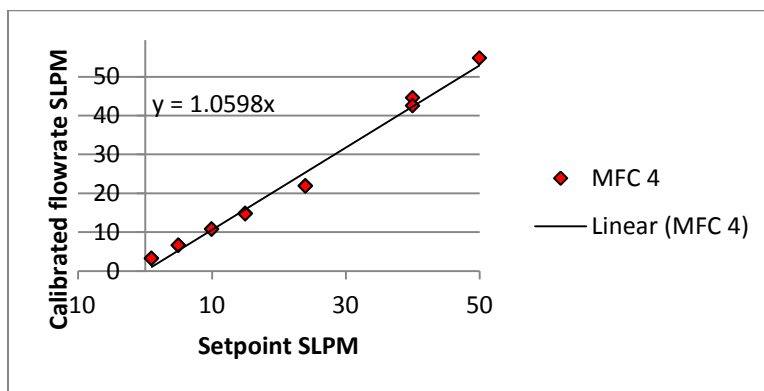
Figure 92. MFC 4 Calibration
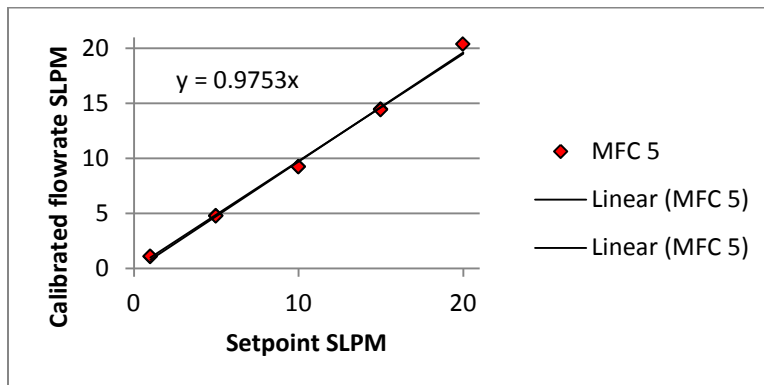
Figure 93. MFC 5 Calibration
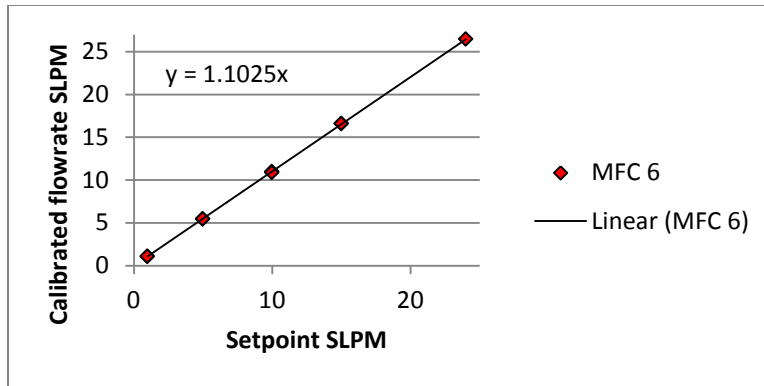
Figure 94. MFC 6 Calibration
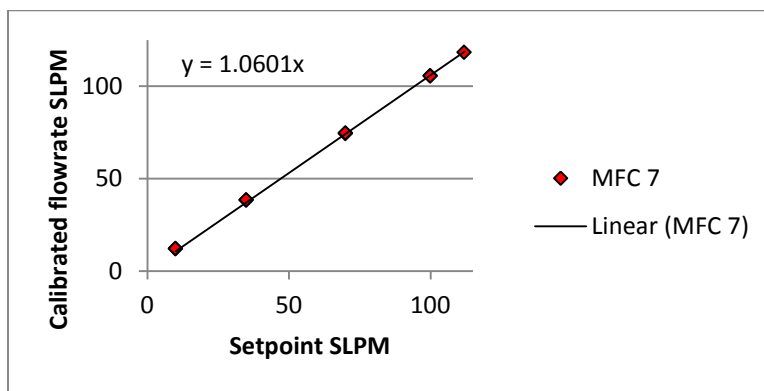
Figure 95. MFC 7 Calibration
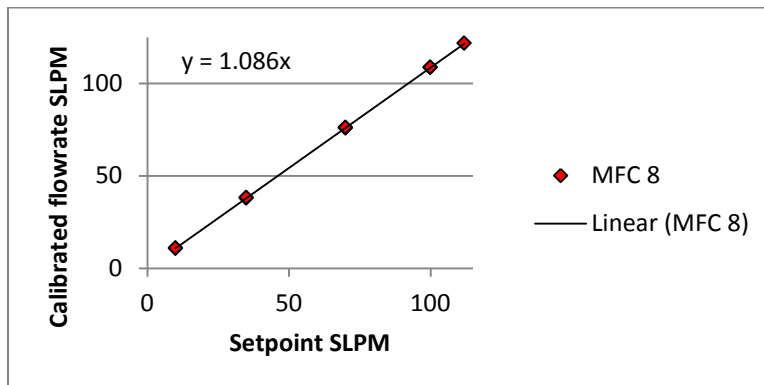
Figure 96. MFC 8 Calibration

133

Appendix E

MATLAB Image Processing for Flame Intensities

To analyze instantaneous and average flame intensities, images in multi-page TIFF format were taken directly from the HSV software and converted into gray scale, red, blue and green channels and saved individually as multi-page TIFF files using ImageJ [42]. Then using the MATLAB [40] code in Figure 97, the figures were broken up into individual TIFF files and the red channel was subtracted from the green and blue channels and saved. These images were then processed using the code in Figure 98 to determine either instantaneous or time-averaged flame intensity.

```
%% image processing
clc
clear

%load total number of images and image data for each color TIFF and break
%multipage TIFF files into individual TIFFs

fname = 'case70blue.tif';
info = imfinfo(fname);
num_images = numel(info);
for k = 1:num_images
    A = imread(fname, k, 'Info', info);
    filename=sprintf('blue%d.tif',k);
    imwrite(A,filename);
end

fname = 'case70green.tif';
info = imfinfo(fname);
num_images = numel(info);
for k = 1:num_images
    A = imread(fname, k, 'Info', info);
    filename=sprintf('green%d.tif',k);
    imwrite(A,filename);
end

fname = 'case70red.tif';
info = imfinfo(fname);
num_images = numel(info);
for k = 1:num_images
    A = imread(fname, k, 'Info', info);
    filename=sprintf('red%d.tif',k);
    imwrite(A,filename);
end

% read individual files for each channel and subtract the red channel from
% the sum of the green and blue channels.

for k = 1:num_images
    filename=sprintf('blue%d.tif',k);
    B=imread(filename);
    filename=sprintf('green%d.tif',k);
    G=imread(filename);
    filename=sprintf('red%d.tif',k);
    R=imread(filename);

    X=G+B-2*R;

    filename=sprintf('X%d.tif',k);
    imwrite(X,filename);

end
```

Figure 97. Initial image processing to subtract red channel

135

```
%clear previous data
clc
clear
clear all
%read first image
Y=imread('X1.tif');
%convert first image to 32 bit
Z=uint32(Y);
%specify number of images to average
num_images=45;

%read, convert form uint8 to uint32, and add images
for i=2:num_images
    R=imread(sprintf('X%d.tif',i));
    R=uint32(R);
    Z=Z+R;
end
%find average
Z=Z/num_images;
%print images to intensity color map and crop
figure
Z=imagesc(Z);
colormap(jet)
axis equal
axis off
caxis([0 90])
axis([200 450 50 600])
```

Figure 98. Image processing to find flame intensities at instantaneous or average time

Appendix F

Redesign of Previous Sectional Rig Core Section

Previous to the design of the new full annular rig, the Anderson [17] sectional rig needed to be modified in order to switch the location of the core vane suction side to the opposite location with respect to the cavity flow direction to study what effect this change would cause on the flow migration from the cavity to the core. The flow in the circumferential cavity ideally moves such that it migrates into the axial core and follows the suction surface of the vane. The low pressure region created by the suction side helps pull flow out of the cavity and reduces needed cooling schemes to a single side of the vane. The rig did not originally follow the UCC design scheme. The suction side of the vane faced away from migrating cavity flow and effects of the low pressure region assisting in migration were lost. The upper surface was flat and was not representative of the vane at all.

Moving the suction side to the correct position for the current rig required two completely new pieces to be designed and fabricated. For comparison purposes to LeBay [21], Parks and Polanka [19], and this author agreed that only the position of the suction side should be changed, and a representative pressure side should not be added and the overall cross sectional area of the core should remain the same. The original SolidWorks [44] models were used to simply change the existing pieces to meet the new criteria, but a slight design change was made so that a single base piece was created in which different vane inserts could be installed and removed without disassembling the entire rig, seen in Figure 99. This both increased the efficiency of the model and reduced fabrication time and needed material. The original location of the suction surface was replaced with a quartz window for optical access.

137
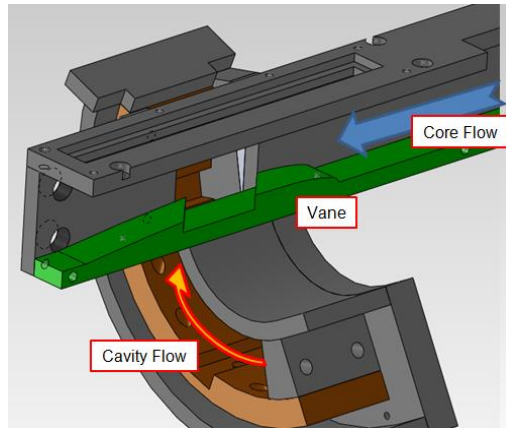
(a)
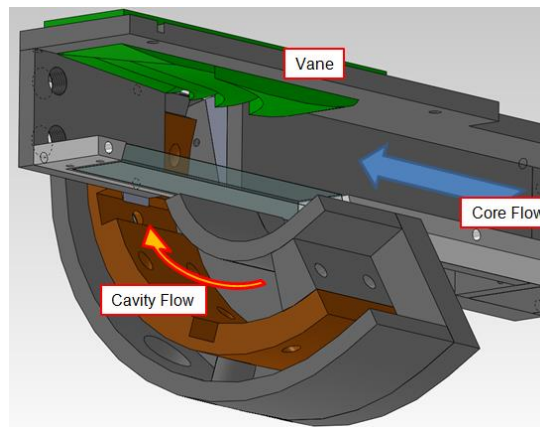
(b)

Figure 99. (a) Sector rig with vane on the bottom and (b) vane repositioned to the top.

Three vane inserts were created to fit inside the base piece, seen in Figure 17. The first two, vane with an angled RVC and vane without an RVC, mirrored previous vane studies with the vane in its original, incorrect position. The third vane insert was a hybrid RVC design that was conceived to create a more evenly distributed temperature distribution at the exit of the core. With the vane with an angled RVC cavity, migrating flow would move radially through the core and impact the ID. The "tiger claw" RVC design was envisioned to desensitize the flow to

different operating conditions such that a uniform temperature field was always present at the

exit of the core.

Appendix G

PIV Seeder Design

Both Thomas [45] and LeBay et al. [20] used laser diagnostics, specifically PIV measurements to study flow velocity in the AFIT small-scale, sector UCC rig. Using this technique requires the flow field of the experiment (in this case, the core section of the Ultra Compact Combustor) to be seeded with small particles, on the order of magnitude of 0.5 to 2.0 microns depending on the resolution, velocity, and other factors: light enough to follow the flow field. A laser "sheet" passes through the flow perpendicular to the imaging plane desired and excites these particles, allowing a high speed camera system to track them as they move through the experiment. Consecutive images are then analyzed to determine the particles initial position and final location between two images, from which a velocity vector is determined [21, 22, 45].

The seeder used by Thomas [45] was of the rotating drum type, and lack of seed density or seed density variation was reported [45]. The seeder type used by Schmidt et al. [46] involved a vertical cylinder in which high pressure air was brought in and mixed with seeding powder/particles while pneumatic agitators helped the seed become airborne and better distributed. This system served as the basis for the design of a new seeder system for experiments in the COAL Lab.
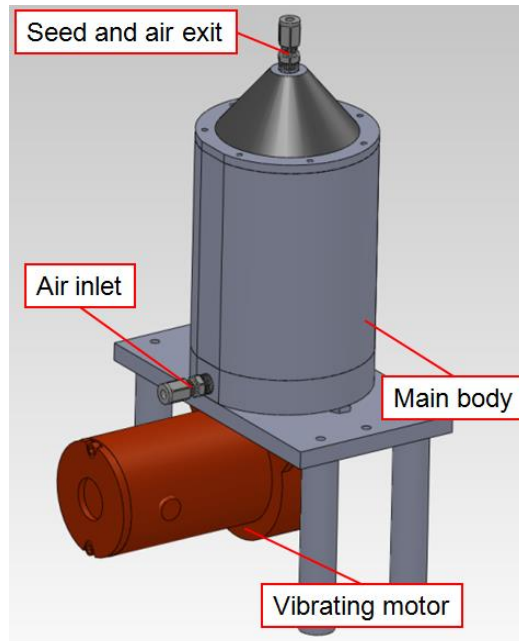
(a)

(b)

Figure 100. SolidWorks CAD model of (a) new seeder system and (b) hardware in a dual configuration

[22]

The new seeder system was envisioned and designed in SolidWorks [44]. The body was a hollow cylinder that mounted to a base with swirling air-injectors with the goal to create a cyclone within the cylinder to help pull seed into the air and into the hose leading to the experiment. A metal screen was used to keep the seed powder from falling into the air injector jets while the system was not running. The top of the seeder was removable to allow the addition of the powder and was conical shape to help direct flow into the exit port. Mating surfaces between the base, body, and top were sealed with rubber gaskets on the inside diameter to keep pressure within the main assembly. The system used by Thomas was configured with nitrogen since air would cause the stoichiometry inside the experiment to be changed, however properties could still be affected with excess nitrogen. The new system was configured with air on a mass flow controller, requiring only minor bookkeeping when seeding the flow to keep track of air mass in the experiment.

The main assembly was mounted onto a platform onto which a Vibe Co. variable speed/force electric agitator motor, model SCR-100, was installed underneath. Using an electric agitator allowed for more control of the seed density in the system with simpler setup. This was mounted on four metal columns with vibration reducing washers between the columns and the platform.
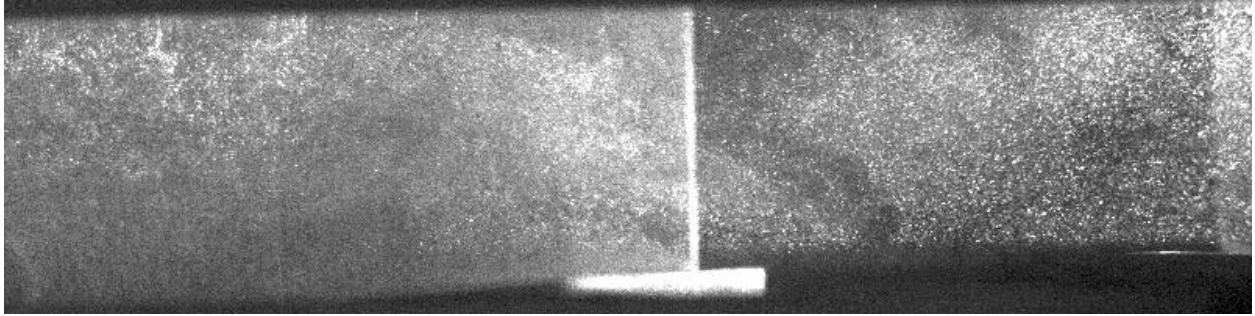
Figure 101. Seed density in AFIT sector UCC core [22]

As seen in Figure 101, the seed content and distribution in the core flow of the sectional, small-scale rig while using the new seeder system was much improved of the old drum systems. It could also be easily varied by changing the amount of air through the seeders and/or varying the speed of the vibrating motors. This allowed precise control over the seed density and the ability to better use PIV diagnostic techniques.

VI. References

1. Mattingly, J. D., Heiser, W. H., Pratt, D. T., *Aircraft Engine Design*, 2nd edition, AIAA, Reston, Virginia, 2002.

2. LeBay, K., Polanka, M., Branam, R., "Characterizing the Effect of Radial Vane Height on Flame Migration in an Ultra Compact Combustor," Proceedings of ASME Turbo Expo, GT2011-45919, 2011.

3. Zelina, J., Sturgess, G. J., and Shouse, D. T., "The Behavior of an Ultra-Compact Combustor (UCC) Based on Centrifugally Enhanced Turbulent Burning Rates," 40th AIAA/ASME/SAE/ASEE Joint Propulsion Conference, AIAA-2004-3541, 2004.

4. Bohan, B.T. and Polanka, M.D. "Analysis of Flow Migration in an Ultra-Compact Combustor," Journal of Engineering for Gas Turbines and Power, vol. 135, 051502 1-11, 2013.

5. Turns, S. R., *An Introduction to Combustion*, 3rd edition, McGraw-Hill, Inc., New York, 1996.

6. Lewis, G. D., "Swirling Flow Combustors – Fundamentals and Applications," Presented at AIAA/SAE 9th Propulsion Conference, Las Vegas, Nevada, AIAA-1973-1250, 1973.

7. Sirignano, W. A., Delplanque, J. P., Liu, F., "Selected Challenges in Jet and Rocket Engine Combustion Research," 33rd AIAA/ASME/SAE/ASEE Joint Propulsion Conference, Seattle, Washington, AIAA-1997-2701, 1997.

8. Yonezawa, Y., Toh, H., Goto, S., Obata, M., "Development of the Jet-Swirl, High Loading Combustor," 26th AIAA/ASME/SAE/ASEE Joint Propulsion Conference, Orlando, FL, AIAA-1990-2451, 1990.

9. Anthenien, R. A., Mantz, R. A., Roquemore, W. M., and Sturgess, G. J., "Experimental Results for a Novel, High Swirl, Ultra Compact Combustor for Gas Turbine Engines," 2nd Joint Meeting of the U.S. Sections of the Combustion Institute, Oakland, CA. 2001.

10. Zelina, J., Sturgess, G., Hancock, R., "Ultra-Compact Combustors for Advanced Gas Turbine Engines," 49th ASME International Gas Turbine and Aeroengine Congress and Exposition, Vienna, Austria, GT2004-53155, 2004.

11. Zelina, J., Greenwood, R. T., Shouse, D. T., "Operability and Efficiency Performance of Ultra-Compact, High Gravity (g) Combstor Concepts," Proceedings of ASME Turbo Expo 2006, Barcelona, Spain, GT2006-90119, 2006.

12. Anderson, W., Radtke, J., King, P., Thornburg, H., Zelina, J., Sekar, B., "Effects of Main Swirl Direction on High-g Combustion," 44th AIAA/ASME/SAE/ASEE Joint Propulsion Conference and Exhibit, Hartford, Connecticut, AIAA-2008-4954, 2008.

13. Greenwood, R. T., "Numerical Analysis and Optimization of the Ultra-Compact Combustor," Graduate School of Engineering and Management, Air Force Institute of Technology (AU), WPAFB, Ohio, Master's thesis, 2005.

14. ANSYS FLUENT CFD software. ANSYS 2013

15. Anisko, J., "Numerical Investigation of Cavity-Vane Interactions Within the Ultra-Compact Combustor," Graduate School of Engineering and Management, Air Force Institute of Technology (AU), WPAFB, Ohio, Master's thesis, 2006.

16. Moenter, D. S., "Design and Numerical Simulation of Two Dimensional Ultracompact Combustor Model Sections for Experimental Observation of Cavity- Vane Flow Interactions," Graduate School of Engineering and Management, Air Force Institute of Technology (AU), WPAFB, Ohio, Master's thesis, 2006.

17. Anderson, W. S., "Design, Construction, and Validation of the AFIT Small Scale Combustion Facility and Sectional Model of the Ultra-compact Combustor," Graduate School of Engineering and Management, Air Force Institute of Technology (AU), WPAFB, Ohio, Master's thesis, 2007.

18. National Instruments LabVIEW graphical programming code. National Instruments 2012

19. Parks, A. K., Polanka, M. D., "Quantifying Exhaust Emissions and Temperature of the Ultra-Compact Combustor," 50th AIAA Aerospace Sciences Meeting, Nashville, Tennessee, AIAA-2012-0935, 2012.

20. LeBay, K.D., Polanka, M.D., and Branam, R.D. "Characterizing the Effect of Radial Vane Height on Flame Migration in an Ultra Compact Combustor," Proceedings of ASME Turbo Expo 2011. Vancouver, British Columbia, GT2011-45919, 2011.

21. LeBay, K. D., "Characterization of Centrifugally-Loaded Flame Migration for Ultra-Compact Combustors," Graduate School of Engineering and Management, Air Force Institute of Technology (AU), WPAFB, Ohio, Doctoral dissertation, 2011.

22. Parks, A. K., "Desensitizing Flame Structure and Exhaust Emissions to Flow Parameters in an Ultra-Compact Combustor," Graduate School of Engineering and Management, Air Force Institute of Technology (AU), WPAFB, Ohio, Master's thesis, 2012.

23. Spytek, C. J., "Application of an Inter-Turbine Burner Using Core Driven Vitiated Air in a Gas Turbine Engine," Proceeding of ASME Turbo Expo 2012, Copenhagen, Denmark, GT2012-69333, 2012.

24. Anderson, J. D., *Modern Compressible Flow*, 3rd edition, McGraw-Hill, Inc., New York, New York, 2004.

25. Radtke, T. J., "Efficiency and Pressure Loss Characteristics of an Ultra-Compact Combustor with Bulk Swirl," Graduate School of Engineering and Management, Air Force Institute of Technology (AU), WPAFB, Ohio, Master's thesis, 2007.

26. Johnson, D. D., "Cooling Requirements for the Ultra-Compact Combustor," Graduate School of Engineering and Management, Air Force Institute of Technology (AU), WPAFB, Ohio, Master's thesis, 2012.

27. Personal communications with Ryan Batelle, 2012.

28. Bergman, T. L., Lavine, A. S., Incropera, F. P., Dewitt, D. P., *Fundamentals of Heat and Mass Transfer*, 7th edition, John Wiley & Sons, Inc., Hoboken, New Jersey, 2011.

29. Glynn, C., O'Donovan, T., Murray, D. B., "Jet Impingement Cooling," Department of Mechanical and Manufacturing Engineering, Trinity College, Dublin.

30. San, J., Lai, M., "Optimum Jet-to-jet Spacing of Heat Transfer for Staggered Arrays of Impinging Air Jets," International Journal of Heat and Mass Transfer, vol. 44, 3997-4007, 2001.

31. Stojkovic, B.D., Fansler, T.D, Drake, M.C., Sick, V., "High-speed Imaging of OH* and Soot Temperature and Concentration in a Stratified-Charge Direct-Injection Gasoline Engine," Proceedings of the Combustion Institute, vol. 30, 2005.

32. Cross, C., Fricker, A., Shcherbik, D., Lubarsky, E., Zinn, B., "Dynamics of Non-Premixed Bluff Body-Stabilized Flames in Heated Air Flow," Proceedings of ASME Turbo Expo 2010, GT2010-23059, 2010.

33. Cross, C., Lubarsky, E., Shcherbik, D., Bonner, K., Klusmeyer, A., Zinn, B., "Determination of Equivalence Ratio and Oscillatory Heat Release Distributions in Non-Premixed Bluff Body-Stabilized Flames Using Chemiluminescence Imaging," Proceedings of ASME Turbo Expo 2011, GT2011-45579, 2011.

34. Conrad, M. M., Wilson., J. D., Polanka M. D., "Integration Issues of an Ultra-Compact Combustor to a Turbine Engine," 49th AIAA/ASME/SAE/ASEE Joint Propulsion Conference and Exhibit, San Jose, CA. 2013.

35. Conrad, M. M., "Integration of an Inter-Turbine Burner to a Jet Turbine Engine," Graduate School of Engineering and Management, Air Force Institute of Technology (AU), WPAFB, Ohio, Master's thesis, 2013.

36. Wilson, J. D., Polanka, M. D., "Reduction of Rayleigh Losses in a High g-Loaded Ultra Compact Combustor," Proceedings of the ASME Turbo Expo 2013, San Antonio, Texas, GT2013-94795, 2013.

37. Wilson., J. D., Polanka M. D., Conrad, M. M., "Flame Structure Effects at High g-Loading," 49th AIAA/ASME/SAE/ASEE Joint Propulsion Conference and Exhibit, San Jose, CA. 2013.

38. "Hastelloy X Alloy," Haynes International, High-Temperature Alloys 1997

39. Souder, W. H., Hidnert, P., "Thermal Expansion of Nickel, Monel, Metal, Stellite, Stainless Steel, and Aluminum," Scientific Papers of the Bureau of Standards, vol. 17.

40. MATLAB version 2011b, The MathWorks, Inc., 2013

41. Digital Particle Image Velocimetry (DPIV) software, Larry Goss, Innovative Scientific Solutions, Inc., Dayton, Ohio.

42. ImageJ, image-processing program, National Institutes of Health, 2013.

43. Moffat, R. J., "Contributions to the Theory of Single-Sample Uncertainty Analysis," Journal of Fluids Engineering, vol. 104, 1982.

44. Dassault Systems SolidWorks CAD software. Dassault Systems 2013

45. Thomas, L. M., "Flow Measurements Using Particle Image Velocimetry in the Ultra Compact Combustor," Graduate School of Engineering and Management, Air Force Institute of Technology (AU), WPAFB, Ohio, Master thesis, 2009.

46. Schmidt, J., Kostka, S., Lynch, A., and Ganguly, B., "Simultaneous Particle Image Velocimetry and Chemiluminescence Visualization of Millisecond-Pulsed Current–Voltage-Induced Perturbations of a Premixed Propane/Air Flame," Experiments in Fluids, Vol. 51, 2011.

<table>
<tr><td colspan="2" align="center">REPORT DOCUMENTATION PAGE</td><td><i>Form Approved</i>
<i>OMB No. 074-0188</i></td></tr>
</table>

REPORT DOCUMENTATION PAGE		*Form Approved* *OMB No. 074-0188*

The public reporting burden for this collection of information is estimated to average 1 hour per response, including the time for reviewing instructions, searching existing data sources, gathering and maintaining the data needed, and completing and reviewing the collection of information. Send comments regarding this burden estimate or any other aspect of the collection of information, including suggestions for reducing this burden to Department of Defense, Washington Headquarters Services, Directorate for Information Operations and Reports (0704-0188), 1215 Jefferson Davis Highway, Suite 1204, Arlington, VA 22202-4302. Respondents should be aware that notwithstanding any other provision of law, no person shall be subject to an penalty for failing to comply with a collection of information if it does not display a currently valid OMB control number.
PLEASE DO NOT RETURN YOUR FORM TO THE ABOVE ADDRESS.

1. REPORT DATE *(DD-MM-YYYY)* 12-09-2013	2. REPORT TYPE Master's Thesis	3. DATES COVERED *(From – To)* June 2011 – August 2013

TITLE AND SUBTITLE Characterizing G-Loading, Swirl Direction, and Rayleigh Losses in an Ultra Compact Combustor	5a. CONTRACT NUMBER
	5b. GRANT NUMBER
	5c. PROGRAM ELEMENT NUMBER

6. AUTHOR(S) Wilson, Jacob D.	5d. PROJECT NUMBER
	5e. TASK NUMBER
	5f. WORK UNIT NUMBER

7. PERFORMING ORGANIZATION NAMES(S) AND ADDRESS(S) Air Force Institute of Technology Graduate School of Engineering and Management (AFIT/ENY) 2950 Hobson Way, Building 640 WPAFB OH 45433-8865	8. PERFORMING ORGANIZATION REPORT NUMBER AFIT-ENY-13-S-02

9. SPONSORING/MONITORING AGENCY NAME(S) AND ADDRESS(ES) Air Force Research Lab Air Force Office of Scientific Research Dale Shouse Chipping Li 1790 Loop Road 875 N Randoplh St. Wright-Patterson AFB, OH 45433 Arlington, VA 22203	10. SPONSOR/MONITOR'S ACRONYM(S) AFOSR AFRL
	11. SPONSOR/MONITOR'S REPORT NUMBER(S)

12. DISTRIBUTION/AVAILABILITY STATEMENT
   DISTRUBTION STATEMENT A. APPROVED FOR PUBLIC RELEASE; DISTRIBUTION UNLIMITED.

13. SUPPLEMENTARY NOTES
This material is declared a work of the U.S. Government and is not subject to copyright protection in the United States.

14. ABSTRACT

   Previous research has been conducted showing significant benefits on combustion efficiency and stability by creating high centripetally accelerated, also known as g-loaded, combustion environments. Ultra Compact Combustor systems decrease size and weight of the overall engine by burning in a circumferential direction around a hybrid vane row where the high equivalence ratio cavity flow is quick quenched to lean by the core flow. The hybrid vane row integrates the compressor, combustor, and turbine for further length reduction and weight savings. Fuel and air are brought into the cavity and combusted in a high g-loaded environment driven by air injection at an angle tangent to the cavity outer diameter. The Air Force Research Lab and Air Force Institute of Technology have worked previously on compact combustor designs, and a new, high g-loaded, Ultra Compact Combustor has been designed to study flow characteristics in the cavity and core to help understand integration issues with engine systems.

15. SUBJECT TERMS
   combustion, high g-load, ultra compact combustor, inter-turbine burner, Rayleigh loss, flame stability, hybrid vane, experimental combustor, high speed video

16. SECURITY CLASSIFICATION OF:			17. LIMITATION OF ABSTRACT	18. NUMBER OF PAGES	19a. NAME OF RESPONSIBLE PERSON Dr. Marc D. Polanka, AFIT/ENY
a. REPORT U	b. ABSTRACT U	c. THIS PAGE U	UU	166	19b. TELEPHONE NUMBER *(Include area code)* (937) 255-3636 ext. 4714 Marc.Polanka@afit.edu

<div align="right">

Standard Form 298 (Rev. 8-98)
Prescribed by ANSI Std. Z39-18
</div>